Ventilation processes of the Mediterranean Sea based on CFC-12 and SF$_6$ measurements

Diplomarbeit

am

Leibniz-Institut für Meereswissenschaften

der

Mathematisch-Naturwissenschaftlichen Fakultät

an der

Christian-Albrechts-Universität zu Kiel

vorgelegt von

Tim Stöven

geb. am 29.05.1987

Matrikelnummer: 861537

Erstprüfer: Prof. Dr. Arne Körtzinger

Zweitprüfer: Dr. Toste Tanhua

Kiel, den 30. November 2011

Contents

Abbrevations

CO_2	Carbon dioxide
ADW	Adriatic Deep Water
AGAGE	Advanced Global Atmospheric Gases Experiment
ASOW	Adriatic Sea Outflow Water
AW	Atlantic Water
BiOS	Bimodal Oscillating System
CBM	Communication Bus Module
CFC	Chlorofluorocarbon
CFC-12	Chlorofluorocarbon-12
CIW	Cretan Sea Intermediate Water
cmp	Custom Made Product
CSOW	Cretan Sea Overflow Water
CTD	Conductivity Temperature Depth
DIC	Dissolved Inorganic Carbon
ECD	Electron Capture Detector
EMDW	Eastern Mediterranean Deep Water
EMed	Eastern Mediterranean
EMT	Eastern Mediterranean Transient
GC-MS	Gas Chromatograph - Mass Spectrometer
GWP	Global Warming Potential
LIW	Levantine Intermediate Water
MAW	Modified Atlantic Water
Med	Mediterranean Sea
POEM	Physical Oceanography of the Eastern Mediterranean
PT3	Purge and Trap System 3

PTFE	Polytetrafluoroethylene
PVC	Polyvinylchloride
SF_6	Sulfurhexafluoride
SST	Stainless Steel Tubing
TDW	Tyrrhenian Dense Water
TMZ	Tracer Minimum Zone
TTD	Transit Time Distribution
VS1	Vacuum Sparge System 1
WMDW	Western Mediterranean Deep Water
WMed	Western Mediterranean

List of Figures

List of Tables

Danksagung

An aller erster Stelle möchte ich mich bei meinen Eltern für die sehr gute Unterstützung während meines gesamten Studiums bedanken. Ohne den moralischen Beistand in schwierigeren Zeiten wäre mein Studium sicherlich nicht so einfach zu schaffen gewesen.

Besonderen Dank gilt Dr. Toste Tanhua, der diese Diplomarbeit erst ermöglicht hat, und dessen exzellente Fahrtleitung der Forschungsfahrt M84-3 zu einem umfangreichen Datensatz geführt hat. Durch die sehr gute Betreuung auf der Forschungsreise und am IFM-Geomar hat mir die Arbeit viel Freude bereitet. Des Weiteren haben die Freiheiten und auch die direkte Art von konstruktiver Kritik zu einer sehr angenehmen Arbeitsatmosphäre geführt. An dieser Stelle seien auch Tina Schütt und Boie Bogner gedankt, die durch ihr technisches Fachwissen die sehr eigenwilligen Messgeräte nach diversen Ausfällen wieder reparieren konnten und mich an den vielen schlechten Tagen im Labor immer wieder aufgebaut haben. Karen Stange, Sebastian Fessler und Nils Clasen danke ich für die äußerst amüsante Zeit auf den Forschungsfahrten, im Hafen und im Büro. Meinem Bruder und Dirk Hopmann danke ich für das kurzfristige Korrekturlesen und den stressabbauenden Freizeitgestaltungen neben der Arbeit.

Zu guter Letzt möchte ich meiner Freundin vom ganzen Herzen dafür danken, dass sie trotz meiner ständigen Abwesenheit und den seltenen Zweisamkeiten zu mir steht und mich in allen Lebenslagen unterstützt.

Zusammenfassung

Für einen Großteil des Mittelmeeres erlauben die gesammelten Tracerdaten eine Bestimmung der TTD Mischungsverhältnisse. Das Ionische und Levantinische Meer können durch ein $^\Delta/_\Gamma$-Verhältnis zwischen $0.6 - 0.8$ beschrieben werden. Das Adriatische Meer hat für Tiefen oberhalb von $600\,m$ ein recht hohes Mischungsverhältnis von $^\Delta/_\Gamma = 1.2$ und für die darunter liegenden Wasserschichten ein niedriges Mischungsverhältnis von $^\Delta/_\Gamma = 0.6$. Die Tracerdaten aus dem westlichen Mittelmeer sowie der Ägäis und des Kretischen Meeres sind nicht auf das 1D-TTD-Modell anwendbar. Für das Westbecken begründet sich dies entweder darauf, dass das Tracerpaar nicht die Vorgaben des 1D-Modells erfüllt, oder ein anderes Modell gewählt werden muss. Das $^\Delta/_\Gamma$-Verhältnis der Ägäis und des Kretischen Meeres kann nicht bestimmt werden, da die Aussagekraft des CFC-12 Tracers für junge Wassermassen sehr gering ist. Für alle diese Seegebiete wird ein mittleres Mischungsverhältnis von $^\Delta/_\Gamma = 1.0$ angenommen. Basierend auf den Tracerdaten wurden jüngste Veränderungen in der Wassersäule des Mittelmeeres analysiert. Das östliche Mittelmeer kehrt zu einem Prä-EMT-Zustand (Eastern Mediterranean Transient) zurück, mit dem Adriatischem Meer als Haupttiefenwasserquelle für das Tiefenwasser des östlichen Mittelmeeres. Der letzte Tiefenwassereintrag vom Adriatischen Meer kann durch die erhöhten CFC-12 Konzentrationen $> 230\,ppt$ im Bodenwasser des westlichen Ionischen Meeres nachgewiesen werden. Die Tracerminimumzone hat sich weiter vertikal und westwärts ausgedehnt, ohne das jüngeres und dichteres Wasser aus der Ägäis beziehungsweise des Kretischen Meeres eingedrungen ist. Die jüngste massive Tiefenwasserbildung im westlichen Mittelmeer (Western Mediterranean Transit)

kann anhand von CFC-12 Konzentrationen $> 220\,ppt$ aufgezeigt werden. Die genaue Ausdehnung des Tiefenwassers im westlichen Mittelmeer konnte bisher nicht exakt bestimmt werden. Wassermassen mit Charakteristiken von diesem Tiefenwasser fließen über die Schwelle zwischen Sizilien und Sardinien in das Tyrrhenische Meer und sind bis in $2500\,m$ Tiefe in der Nähe vom sizilianischem Hang aufzufinden. Des Weiteren konnte aufgrund der ausreichend bestimmten $^\Delta/_\Gamma$-Mischungsverhältnisse im Ostbecken eine genauere Abschätzung des Wassersäulengehalts an anthropogenem Kohlenstoff durchgeführt werden. Erste Berechnungen zeigen, dass der Wassersäulengehalt im Mittel um ca $4.4\,\%$ unterschätzt wurde im Vergleich zu Schneider et al. [2010].

Summary

The tracer data of CFC-12 and SF_6 allow to determine a TTD ratio for most of the Eastern Mediterranean. The Ionian and Levantine Sea can be described by Δ/Γ ratios between $0.6 - 0.8$. The Adriatic Sea has a high ratio of $\Delta/\Gamma = 1.2$ for depths above $600\,m$ and a low ratio of $\Delta/\Gamma = 0.6$ for the layers below. The tracer data of the Western Mediterranean as well as the Aegean and Cretan Sea does not fit into the 1D-TTD model. The reasons for the WMed are, that either the tracer couple does not fit into the 1D model or another TTD model must be chosen. The Δ/Γ ratio of the Aegean and Cretan Sea could not be determined due to the less significance of CFC-12 for young water masses. For all these sea areas a Δ/Γ ratio of 1.0 was set as mean ratio. Based on the tracer data, recent changes in the water column of the Mediterranean Sea were analyzed. The Eastern Mediterranean returns to a pre EMT (Eastern Mediterranean Transient) state with the Adriatic Sea as the major dense water source for the deep water of the Eastern Basin. The last dense water input from the Adriatic Sea can be verified in the bottom layer of the western Ionian Sea with CFC-12 concentrations $> 230\,ppt$. The tracer minimum zone spreads out vertically and westwards with no intrusion of younger and denser water from the Aegean and Cretan Sea. The recent massive deep water formation of the Western Mediterranean (Western Mediterranean Transit) is shown by CFC-12 concentrations $> 220\,ppt$. The exact spreading of the newly formed deep water could not be determined yet. Watermasses with characteristics of the Western Mediterranean deep water are entering the Tyrrhenian Sea via the channel between Sicily and Sardinia and are present at depths down to $2500\,m$ near the slope of Sicily. Based on the Δ/Γ

ratios of the Eastern Mediterranean Sea, a new estimation of column inventories of anthropogenic carbon could be carried out. First calculations show that the column inventories have been underestimated by about $4.4\,\%$ in comparison to Schneider et al. [2010].

1. Introduction

At first sight, the Mediterranean Sea seems to be just a relatively small marginal sea, where many Europeans spend their holdiays at the coast. In contrast, a view under the water surface shows a very complex system of water mass movements (e.g. currents, gyres, deep water formations) between several main and subbasins. A powerful tool to analyse changes and characteristics of water masses are transient tracers like chlorofluorocarbons (CFC's) or sulfurhexafluoride (SF_6).

The main focus of this work is to analyse the recent changes in the Mediterranean Sea, such as deep water or intermediate layer formation. Furthermore, the current characteristics of the water column were determined. A comprehensive tracer survey was carried out in spring 2011 during Meteor cruise M84-3 and provided the basis for the analysis.

1.1. Transient tracers and atmospheric history

Transient tracers are chemical tracers with a time varying source or sink. Freon 12 (CFC-12) was mainly produced for aerosol spray propellants and refrigerants and had only anthropogenic sources. It was produced first in 1928 with an exponential increase of the atmospheric concentration until the late 1970s (Figure 1.1). Due to the chemical property of CFC's to deplete the ozone layer in the stratosphere, a world wide agreement was created in 1987, called *Montreal Protocol*. This protocol includes to reduce and subsequently to stop the production of ozone layer depleting components. It was ratified by 196 countries until 1992. The atmospheric concentra-

Table 1.1. – Measurement stations of the AGAGE network.

Station	Country
Mace Head	Ireland
Trinidad Head	Oregon, California
Ragged Point	Barbados
Cape Matatula	Samoa
Cape Grim	Tasmania

tion curve of CFC-12 ed out until it reached a maximum of $546.7\,ppt$ in the year 2002 with a following concentration decrease to $532.49\,ppt$ in the year 2011 which shows the success of this world wide agreement (Figure 1.1).

SF_6 has been produced since the 1950s and is used as insulating gas in high voltage engineering and applications. The source of SF_6 is also only anthropogenic and the atmospheric concentration first increased exponentially until the late 1980s where it changed to a linear increase (Figure 1.1). However, SF_6 is no ozone layer depleting component, but it is a very active greenhouse gas with a global warming potential (GWP) of 22.800 [Forster, 2007]. Due to the low atmospheric concentration of $7.48\,ppt$ in the year 2011 the production is not restricted yet.

The atmospheric concentration history of both gases are different for northern hemisphere with higher concentrations and southern hemisphere with lower concentrations (Figure 1.3 and 1.2). This is caused by the main production shares being in the economically stronger industrial nations in the northern hemisphere. There are several measurement stations distributed all over the world, which monthly publish the current atmospheric concentrations of several trace gases. For example, the Advanced Global Atmospheric Gases Experiment (AGAGE) network is listed in Table 1.1.
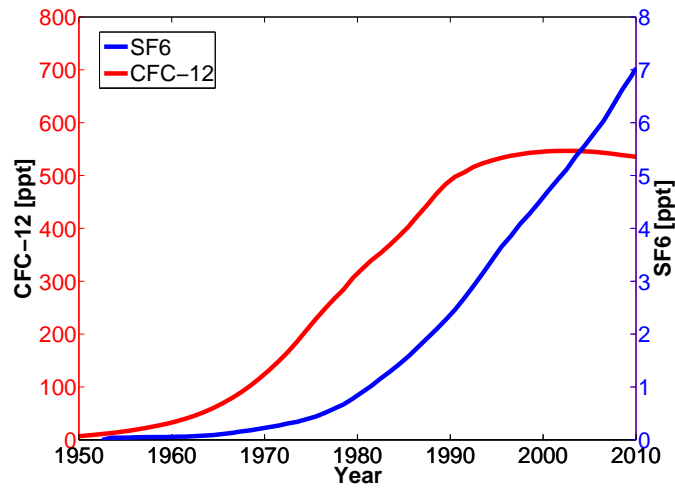
Figure 1.1. – Atmospheric history of CFC-12 (red cruve) and SF$_6$ (blue curve).
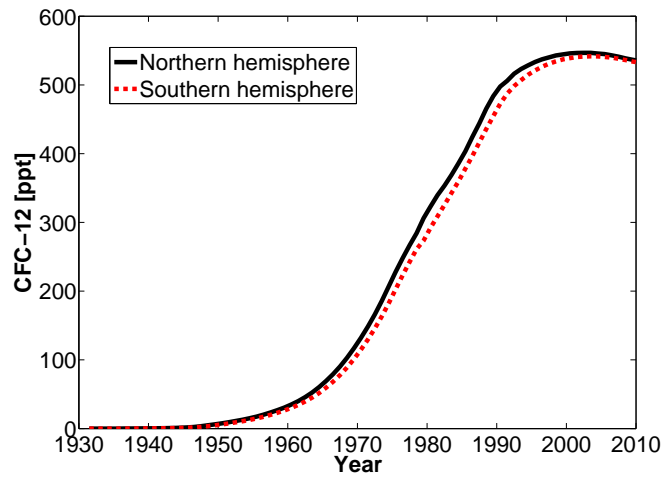
Figure 1.2. – Atmospheric distribution of CFC-12 in the northern hemisphere (black solid curve) and in the southern hemisphere (red dashed curve).
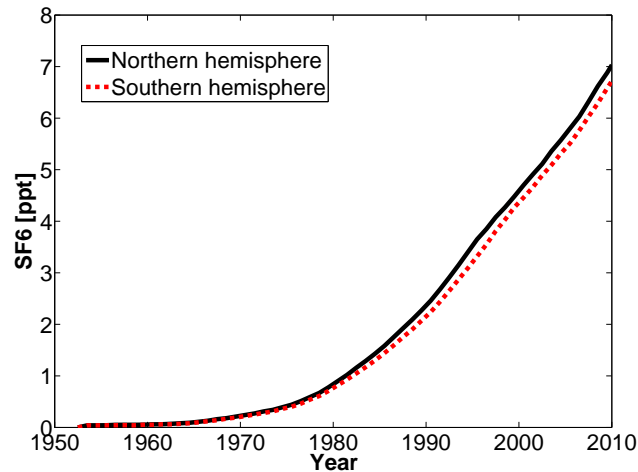
Figure 1.3. – Atmospheric distribution of SF_6 in the northern hemisphere (black solid curve) and southern hemisphere (red dashed curve).

1.2. Transient tracers in the ocean

Gases in the atmosphere are more or less soluble in seawater. The solubility is a function of temperature, salinity and of course the physical nature of the component. A solubility function (Equation 1.1) is described by Warner and Weiss [1985], Bullister et al. [2002]. The constants a and b depend on the tracer and whether the partial pressure of water vapour is taken into account or not.

$$
\begin{aligned}
ln\,F = {} & a_1 + a_2 \left(\frac{100}{T} \right) + a_3 \cdot ln \left(\frac{T}{100} \right) + a_4 \left(\frac{T}{100} \right)^2 \\
& + S \left[b_1 + b_2 \left(\frac{T}{100} \right) + b_3 \left(\frac{T}{100} \right)^2 \right]
\end{aligned}
\tag{1.1}
$$

The partial pressure of a tracer is defined by equation 1.2 [Doney and Bullister, 1992] which is a special form of Henry's law (Equation 1.3).

$$pTracer = \frac{[Tracer]}{F(T,S)_{Tracer}} \tag{1.2}$$

$$[X] = K_H \cdot p(X) \tag{1.3}$$

Where $pTracer$ is the partial pressure of the tracer in equivalent ppt_V, $[Tracer]$ the concentration of the tracer in $\frac{mol}{kg}$ and $F(T,S)_{Tracer}$ the solubility function of the tracer in $\frac{mol}{kg\,atm}$. The saturation of CFC-12 has a time dependency, which means that during the decades with high growth rates in the atmosphere, the saturation was always slightly below 90 % [Tanhua et al., 2008].

CFC-12 and SF_6 are stable in oxygenated water masses. Only CFC-12 is unstable in anoxic regions of the water column [Bullister and Lee, 1995]. The share of anoxic regions in the ocean is very small and as a result of this, both tracers can be described as conserved tracers with no sources or sinks in the ocean and no biogeochemical activity respectively. Together with the well known atmospheric time history, a *tracer age* can be calculated by equation 1.4.

$$c(t_s) = c_0(t') \qquad \text{with} \qquad t' = t_s - t \tag{1.4}$$

In this equation $c(t_s)$ is the concentration of the tracer at sampling year t_s and $c_0(t')$ the surface concentration in the mixed layer at year t' with t as the related transit time also referred as tracer age. This *tracer age* is the real age of a water parcel if there is only an advective flow from the origin into the interior with no sort of mixing or diffusion. Normally mixing is present, so another model is needed, which describes the age of water in a more realistic way.

1.3. Transit Time Distributions

A Transit Time Distribution (TTD) describes a water or air parcel consisting of an age distribution. Mixing and diffusion is taken into consideration. The mathematically background of this theory is based on the Green's function, which was applied to distribution models [Hall and Plumb, 1994]. Equation 1.5 describes a boundary Green's function with χ as the tracer concentration and L as linear transport operator.

$$\frac{\partial \chi}{\partial t} + L\left(\chi\right) = 0 \tag{1.5}$$

This boundary Green's function can be expressed by equation 1.6 with the assumption of a stationary transport. In this equation Ω is the boundary at time ξ, r the interior location at time t and G the transit time distribution.

$$\chi(r,t) = \int_{\infty}^{0} \chi\left(\Omega, t - \xi\right) G\left(r, \Omega, \xi\right) d\xi \tag{1.6}$$

For a one dimensional flow model with constant advective velocity and diffusivity an analytical expression can be determined for a TTD (Equation 1.7)[Waugh et al., 2003].

$$G(t) = \sqrt{\frac{\Gamma^3}{4\pi\Delta^2 t^3}} \cdot exp\left(\frac{-\Gamma(t - \Gamma)^2}{4\Delta^2 t}\right) \tag{1.7}$$

In this equation Γ describes the *mean age* and Δ the *width* of the TTD. The Δ/Γ ratio indiciates the ratio of the advective and diffusivity share in the water parcel.
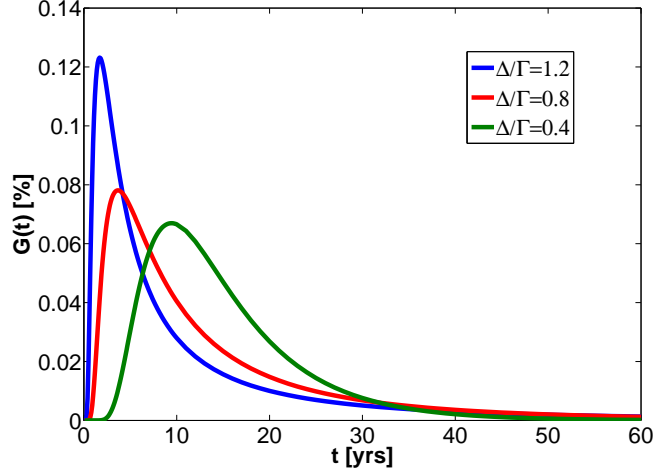
Figure 1.4. – Transit Time Distribution for different $^\Delta/_\Gamma$ ratios

The smaller the $^\Delta/_\Gamma$ ratio the higher the advective share (Figure 1.4). The time t is the transit time (tracer age) the parcel needed from the boundary into the interior. The age spectrum t of the tracer is defined by equation 1.4 with $c_0(t') = 0 - today$.

Equation 1.6 can also be rewritten in a more analytical use (Equation 1.8). The TTD model (G) can be the one dimensional inverse gaussian model (1D-TTD model) or further expressions such as a bimodal two inverse gaussian model (2IG-TTD model) [Waugh et al., 2003]. Furthermore, equation 1.8 connects the TTD with the time dependent surface concentration of the specified tracer and one can obtain the interior concentration $c(r, t_s)$ at location r and sampling year t_s. In this case t' is an integration variable from 0 to ∞. With this equation one can create matrices with defined $^\Delta/_\Gamma$ ratios including the mean age and the associated tracer concentrations and tracer ages. These matrices are then used to connect the measured data with the calculated data and the mean age of each water sample can be obtained.

$$c(r, t_s) = \int_\infty^0 c_0(t_s - t) \cdot G(r, t) dt' \tag{1.8}$$

With the combination of two tracers (e.g. CFC-12, SF$_6$) it is possible to determine

exact ratios or ratios with a low uncertainty fitting to the 1D-TTD model. This ratio approach is, roughly explained, done by minimizing the difference of the tracer's mean ages by changing the ratio. Each tracer couple has its own area of validity, depending on the atmospheric history and the concentration grow rate (Figure 1.1). The validity area of the used $^{SF_6}/_{CFC-12}$ couple and the constraining of the TTD is described later on.

1.4. Anthropogenic carbon and the TTD

The TTD model can also be used to estimate the total amount of anthropogenic carbon in the water column. Therefore it is assumed that the anthropogenic carbon (C_{ant}) behaves like an inert passive tracer with a saturation of $100\,\%$ at the air-sea interface. By combining these assumptions with equation 1.8 the interior concentration of anthropogenic carbon is given by equation 1.9.

$$C_{ant}(t_s) = \int_\infty^0 C_{ant,0}(t_s - s) \cdot G(r,t)dt' \tag{1.9}$$

C_{ant} is the interior concentration of anthropogenic carbon at sampling year t_s, $C_{ant,0}$ the surface concentration at year t' (see equation 1.4) and $G(r,t)$ a TTD, defined by two tracers. The location r is negligible because for each discrete water sample a TTD is compiled. The needed atmospheric concentration history of anthropogenic carbon ($C_{ant,0}$) can be determined with the known atmospheric history of CO_2 and the relation between salinity and alkalinity. The alkalinity is assumed to be constant since preindustrial times and the CO_2 is set to be at constant disequilibrium at the air-sea interface over time with allowed changes in space [Schneider et al., 2010].
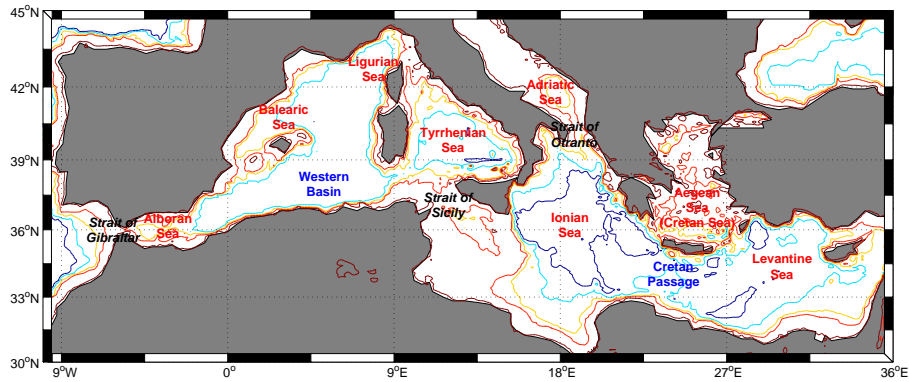
Figure 1.5. – The parts of the Mediterranean Sea. The names of the sea areas are shown in red, the one of the straits in italic black and selected basins and passages in blue. The depth contours are 500 m, 1000 m, 2000 m and 3000 m.

1.5. The Mediterranean Sea - Overview

The Mediterranean Sea (Med) is a marginal sea, which can be devided roughly into two major parts. The Western Mediterranean (WMed) consists of the Alboran Sea, Balearic Sea, Ligurian Sea and the Tyrrhenian Sea (Figure 1.5). It is connected to the Atlantic Ocean via the shallow Strait of Gibraltar and to the Eastern Mediterranean Sea (EMed) via the shallow Strait of Sicily. Both Straits are the limiting factors of water mass exchange between the Atlantic Ocean, western and eastern basin. The major parts of the EMed are the Ionian Sea, Levantine Sea, Adriatic Sea and Aegean Sea and it is connected to the Black Sea via the Dardanelles, the Red Sea via the Suez Canal and of course also with the Western Basin via the Strait of Sicily (Figure 1.5).

1.6. Major circulations and deep water formation

1.6.1. Eastern Mediterranean Sea

Serveral multinational research expeditions have been carried out in the Eastern Mediterranean Sea since the mid 1980s. The POEM (Physical Oceanography of the Eastern Mediterranean) was one of the major scientific programs with the main focus on the understanding of the circulation and mixing processes of the EMed [Malanotte-Rizzoli and Robinson, 1988, Robinson et al., 1992].

Less dense Atlantic surface water (AW) enters the Med through the Strait of Gibraltar going westwards through the Strait of Sicily at shallow depths $(0-200\,m)$ into the EMed. On the way eastwards the salinity increases from 36.5 to > 38 due to evaporation. The AW is then described as Modified Atlantic Water (MAW). Due to high evaporation in summer times and heat loss during winter the surface water gets saltier, colder and respectively dense enough to form an intermediate layer at $200-600\,m$, the so-called Levantine Intermediate Water (LIW). The characteristics of this layer are temperatures of $14.5\,^{\circ}C$ and a salinity of 38.7 [Brasseur et al., 1996]. The mid layer formation takes place presumably simultaneously in several areas of the eastern part of the EMed, but the exact mechanism of this mid layer source is still unknown [Malanotte-Rizzoli and Hecht, 1988]. The LIW mainly flows westwards over the shallow sill of the Strait of Sicily $(\approx 460\,m)$ entering the WMed and finally the Atlantic Ocean through the Strait of Gibraltar [Klein et al., 1999]. The surface water inflow of MAW and the bottom water outflow of LIW are the major currents existing at this shallow sill. The Eastern Mediterranean deep water (EMDW) and Western Mediterranean deep water (WMDW) are completely seperated by the Strait of Sicily.

In the Adriatic and Aegean Sea deep convection of preconditioned surface layers lead to dense bottom water formations. It was expected that the Adriatic Sea was the major source of the renewal of EMDW in the Ionian Basin due to dense Adriatic Sea Outflow Water (ASOW) through the Strait of Otranto [Wuest, 1961]. The resolution

of circulation processes only by potential temperature and salinity was very low. Due to a high homogenity throughout the whole water column of the Ionian and Levantine Sea below $1400\,m$ [Wuest, 1961]. In 1987 the first comprehensive data set of CFC-12 and tritium concentrations were collected during Meteor cruise M5-6 in the EMed as part of the POEM program. The CFC-12 data showed a concentration maximum at the bottom layer of the eastern Ionian Sea with its source from the dense Adriatic Deep Water (ADW) of the southern Adriatic Sea [Schlitzer et al., 1991, Roether and Schlitzer, 1991]. Below the LIW a dense water input from the Cretan Sea was found to form a new intermediate layer between $500 - 1200\,m$ depth, the so-called Cretan Intermediate Water (CIW) [Schlitzer et al., 1991].

A further Meteor cruise in 1995 (M31-1) in the EMed showed an extreme change in the EMDW caused by a massive dense water outflow from the Aegean Sea into the deep water layers of the Ionian and Levantine Basin [Roether et al., 1996]. Following that the major source of deep water formation had changed from the Adriatic Sea to the Aegean Sea. The dense water input from the Aegean Sea between $1989 - 1995$ was three times higher than derived from the Adriatic source in the early 1980s [Lascaratos et al., 1999]. This outflow from Cretan Sea Overflow Water (CSOW) was forced by high salinity values > 39 and thus higher density values in the Cretan Sea than in the Ionian and Leveantine Sea [Klein et al., 1999]. Following this process the homogeneous salinity layer below $1400\,m$ was penetrated by the CSOW and led to an extreme change in salinity and to a higher potential temperature (Θ) at the bottom layer of the eastern Ionian Sea, the Cretan Passage and western Levantine Sea. The newly formed deep water is characterized by higher CFC-12 concentrations than found in 1987 for these layers, coming from the well ventilated CSOW.

Besides the observed CSOW, there were still higher CFC-12 concentrations verifiable, belonging to the last outflow of ASOW. This water mass was located in the western Ionian Basin with its characteristic salinity of 38.668 and a Θ of $13.22\,^{\circ}C$ [Malanotte-Rizzoli et al., 1996].

Furthermore, the CFC-12 minimum zone between $600 - 1400\,m$ depth in the Ionian

Basin and between $600 - 2000\,m$ depth in the Levantine Basin was elevated about $500\,m$ to shallower depth. This was caused by the extrusion of the older deep water layer [Klein et al., 1999]. This uplifting of older, less salty water masses also influenced the water mass inflow into the Adriatic Sea. The LIW with its high salinity was the major water mass entering the Adriatic Sea and was one of the main preconditioning factors for a deep water formation. The uplifted less salty water masses, entering the Adriatic Sea after the Aegean Sea outflow, led to an attenuation of the preconditioning. The Adriatic Sea lost its major role as deep water source for the present [Roether et al., 2007]. This prominent change in deep water sources became known as the Eastern Mediterranean Transient (EMT) .

Based on salinity and density data of the Aegean Sea it was assumed that the dense water outflow startet in the early 1990s. The main output rate was between 1992/93 and started to relax at 1995 [Theocharis et al., 2002]. The major input occured via the Kasos Strait and less through the Antikythera Strait. Salinity and CFC - 12 oberservations carried out 1995, 1997 and 1999 in the Southern Adriatic Sea and Strait of Otranto showed that the input of high salinity water masses has recovered and the capability of the Adriatic Sea to serve as a deep water source increased again [Klein et al., 2000]. Another process influencing the water mass exchange between the Adriatic and Ionian Sea is the Bimodal Oscillating System (BiOS) . The BiOS describes the change of the northern Ionian Gyre from cyclonic to anticyclonic and vice versa on a decadic time scale. It is assumed that this system plays an important role in influencing the Adriatic Sea as deep water source [Civitarese et al., 2010].

Obtained data of CFC-12, salinity and temperature in 2001 (Meteor cruise M51-2) showed, that the changes of salinity and Θ in the bottom layer of the EMed are still present but more uniform. A new dense water input neither from the Adriatic nor the Aegean Sea could be observed [Roether et al., 2007]. Serveral observations of tracers and physical parameters between 2002 and 2007 in the Adriatic and Ionian Sea reinforce the return of the southern Adriatic Sea as a deep water source for EMDW [Hainbucher et al., 2006, Robino and Hainbucher, 2007]. The recently formed EMDW

by ASOW shows a different salinity/temperature character than the pre EMT and pre 2003 formed EMDW with a higher Θ ($> 13.3\,°C$) and salinity (> 38.77).

1.6.2. Western Mediterranean Sea

The MAW is not solely flowing into the EMed. Some parts of the MAW recirculate in the WMed. The circulation path is all along the slope of the european continent through the Tyrrhenian, Ligurian and Balearic Sea [Marullo et al., 1995].

Intermediate water masses coming from the EMed via the Strait of Sicily consist mainly of LIW but there are also water mass characteristics belonging more to ASOW or CSOW [Schlitzer et al., 1991]. The LIW and the lower water layer ($200 - 400\,m$) enter the Tyrrhenian Sea and spread out eastwards along the northern slope of Sicily between $200 - 2000\,m$. The water layer below the LIW is called the Tyrrhenian Dense Water (TDW). A clear seperation between TDW and LIW is not possible because of a smooth transition between both layers [Claude and Millot, 1999]. The further pathway of the LIW and TDW layer is similar to the MAW but with a second main path around Sardinia and Corsica. The deep water layer of the Tyrrhenian Sea ($> 1800\,m$) is supported by dense WMDW from the Western Basin.

The deep water formation in the WMed occurs in the north western part (e.g. Gulf of Lyon). The preconditioning depends on the circulation and respectively recirculation of the MAW and LIW (as surface and subsurface layer). In winter times cold and dry polar air (Mistral) leads to an extreme heat and fresh water loss and thus to a water mass dense enough, to form a new deep water layer (WMDW). The WMDW is characterized by low temperatures between $12.75 - 12.80\,°C$ and a salinity between $38.44 - 38.46$ [Schott et al., 1994]. During the winters of $2004 - 2006$ all required conditions were fulfilled and a massive deep water formation could be observed [Schroeder et al., 2008a, 2010]. Related to the EMT, this deep water formation is called Western Mediterranean Transit (WMT).

2. Material and Method

2.1. Material

The measurements of CFC-12 and SF_6 have been conducted during the M84-3 cruise from Istanbul to Vigo from 5th to 28th april 2011 on the german research vessel *FS Meteor*. There have been 56 stations in total during the cruise which were distinguished in chemistry, isotopes and CTD-only stations (Figure 2.1). At chemistry stations samples were taken for serveral parameters, such as Dissolved Inorganic Carbon (DIC), Alkalinity, Oxygen, etc. Additional to those parameters, isotope samples were taken at the isotope stations (e.g. ^3He, ^{3}H, ^{14}C, etc.). The CTD-only stations were CTD casts with measured parameters of salinity, temperature and depth by sensors without any water sampling.

2.1.1. CFC-12 - Dataset

CFC-12 samples were taken at all chemistry and isotopes stations, so that it was possible to create three main sections from the data set through the whole Mediterranean Sea (Figure 2.2). These three sections are seperated in a WMed section starting at the Tyrrhenian Sea going through the Western Basin into the Alboran Sea and finally ending at the Strait of Gibraltar (Figure 2.2, green line). The second zonal section started from the east part of the EMed in the Levantine Sea going to the western part of the Ionian Sea (Figure 2.2, blue line). The third section is a meriodional section starting in the middle of the Adriatic Basin going through the Strait of Otranto into the middle of the Ionian Sea (Figure 2.2, grey line). There are additional profiles in
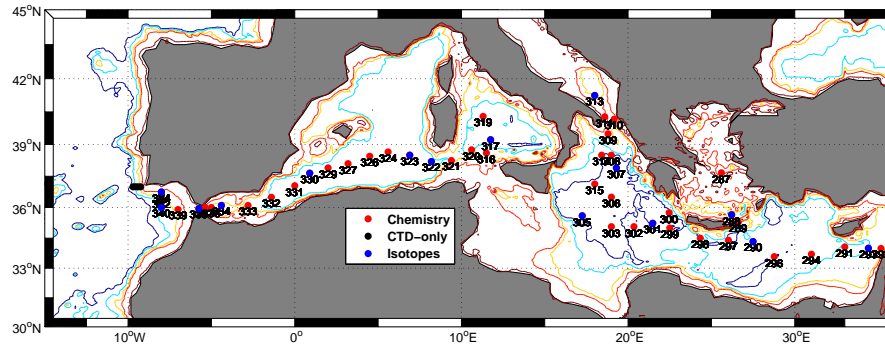
Figure 2.1. – Station numbers of the M84-3 cruise. The stations are seperated in chemistry (red), isotopes (blue) and CTD-only stations (black).

the Aegean and Ionian Sea, which were not used for section calculations but rather for interpretations of local phenomena.

2.1.2. SF$_6$ - Dataset

Due to some technical problems with the measurement system of SF$_6$ it was not possible to obtain such a data set as comprehensive as the one of CFC-12. Because of a leak in the capillary system and a electron capture detector defect samples could not be taken at all stations. However, at eleven key stations (289, 299, 307, 309, 310, 313, 314, 315, 317, 323, 334) samples have been flame sealed in glas ampoules. These key stations have been mainly isotopes stations which allows a comparison of the results based on different tracers and isotopes. The sealed ampoules were measured onshore at the IFM-GEOMAR during september 2011. Nevertheless, there is a sufficient SF$_6$ dataset for two complete sections in the EMed (Figure 2.3), which were equal to the sections of CFC-12 (Figure 2.2, grey and blue line).
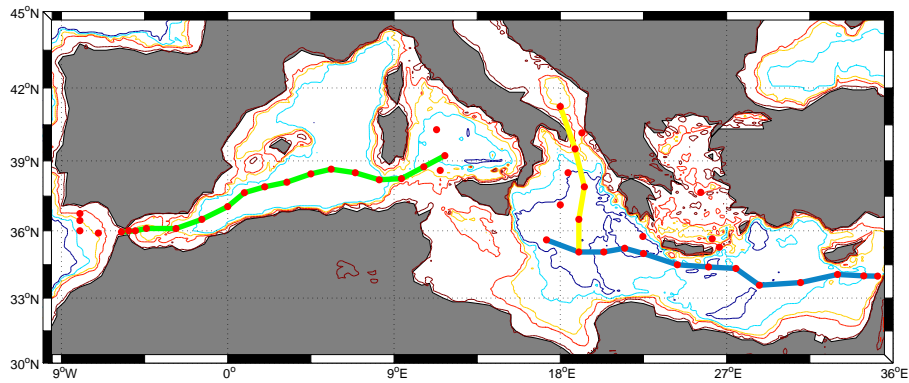
Figure 2.2. – CFC-12 sections and profile data points in the Mediterranean Sea. The three sections consist of the WMed part (green line), the EMed part (blue line) and a Northern Ionian part (yellow line).
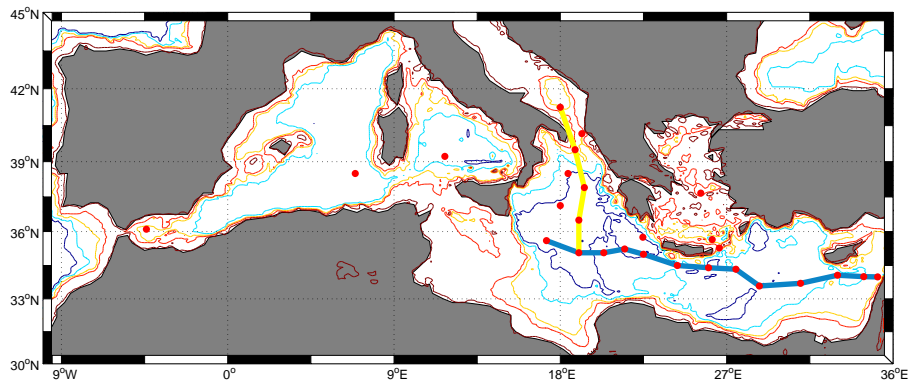
Figure 2.3. – SF$_6$ sections and profile data points in the Mediterranean Sea. The two sections consists of the EMed part (blue line) and the Northern Ionian part (yellow line).

2.2. Sampling

All 10 L niskin bottles were cleaned with isopropanol in advance and all gasket rings were replaced by vented ones to minimize contamination by the sampling system. There were two sampling methods for the two tracers depending on the used measurement system in the lab. The older system named Vaccuum-Sparge-System 2 (VS1), described later on, worked with $300\,ml$ glas ampoules. These ampoules were connected to the niskin bottles via a stainless steel mounting system. The time the water needs to fill up the whole ampoule was ca $1\,min$. The ampoules were connected to the niskin for $4\,min$ each for flushing the whole volume three times. After removing and closing the ampoules with a screw they were stored in a water bath cooled with ice. The measuring rate on board was three samples per hour what implies a maximum store time of $450\,min$ for a complete sample session of 22 niskin bottles.

The other measurement system named Purge and Trap System 3 (PT3) worked with $250\,ml$ glas syringes. This syringes were especially produced for water sampling under exclusion of contact with the atmosphere. Each syringe chamber was rinsed three times with water of the related niskin before the syringe was closed by a valve and also stored in a cooling water bath. During sampling the operator had to make sure that there were no bubbles inside the syringe chamber before closing. The measuring rate for three syringes was close to an hour like the other measurement system with comparable times of storing. The sampling order of all types of samples taken from the niskins was based on the contamination sensitivity by atmosphere contact whereas only the helium and tritium samples were sampled in advanced of CFC-12 and SF_6.

2.3. VS1

2.3.1. Hardware

The older measurement system *VS1* consists of a stainless steel framework with a bottom dimension of standardised pallet size. This framework contains all other equipment parts of the purge and trap gas chromatographic system (Table E.1).

2.3.2. Measurement system during M84

The measurement System *VS1* is based on Monika Rheins purge and trap system[1] in the early 90s (unpublished). The basic functions of this system are roughly the same as tho ones other institutes are using for CFC measurements in seawater [Bullister and Weiss, 1988, Law et al., 1994, Bullister and Wisegarver, 2008].

Generally the measurement program is divided into three main parts. The first part is the filling of the purge chamber, second part is the purge and trap process and the last one is the injection part.

Each sample is prepared by storing them $15\,min$ in a water bath of $35°C$ directly before measuring to enhance the purge efficiency. Afterwards the sample ampoule is connected to the purge tower (Figure 2.4) with a 1/16 PTFE tubing seperated by a magnetic and a second manual valve. Then the first part of the program gets started and the purge tower is evacuated by a vacuum pump to less than $5\,mbar$. The exact value of the low-pressure can not be determined. There are only two uncalibrated manometers connected to Woulffsch's flasks, which show pressure values between $1 - 3\,mbar$. The real pressure is expected to be less than $< 1\,mbar$ related to the power of the vacuum pump.

After $4\,min$ holding the vacuum one has to switch the valve between ampoule and purge tower at the same time when the magnetic valve is switched to open. Without the manual valve the automatically switched magnetic valve would be to weak to

---

[1]All measurement systems are under a continious improvement driven by input of phd-students and technicians

close the purge chamber while evacuating. The sample is sucked into the stripping chamber where the exact and callibrated fill height is controlled by a platinum wire contact bridge. Again $2\,min$ later the magnetic and manual valve get closed and the second part starts. Figure A.1 shows the flow scheme where all valves are in load position and the multi is switched to position 1. To start the purge and trap process of the sample, valve 4 and 6 are switched to inject and the purge flow goes through the water sample stripping the dissolved CFC-12 and SF_6 onto the trap. Valve 5 is built in between valve 4 and the purge tower to reduce the power of the purge flow of the first few seconds to avoid that water enters the system through the purge flow exit. This valve is also controlled manually and the switch time depends on the water sample and the formed bubbles in the head space of the purge chamber. During the purge process the trap is held in a Dewar at which the bottom is filled with liquid nitrogen. To stop the purge and trap process, valve 4 and 6 are switched back to load position. Then part three starts and the trap is heated for $30\,sec$, controlled by a PID, to transfer the traped molecules into the gas phase (desorption process). The heater consists of a PID control unit and a transformer. The heating is based on the lower electrical resistance of the copper wire of the transformer in relation to the stainless steel tubing of the trap which is therefore resistantly heated.

After reaching the end temperature valve 7 is switched to inject and the carrier gas flows through the trap, transporting the analytes over the precolumn into the main column and finally to the electron capture detector (ECD) . The start signal for recording the chromatogram and to define the zero point of retention time is right at the same time as valve 7 is switched to inject. After $30\,sec$ valve 7 is switched back to load position to cut of later eluting components and valve 6 is switched to inject for backflushing the precolumn. After $120\,sec$ valve 6 is set to load position and the heater is turned off to recool the trap to the trapping temperature. At the same time the sample can be replaced by a new one.

The highly purified nitrogen carrier and purge gas (ECD quality), both seperated, flow through a $2\,m$ x 1/4 stainless steel tubing (SST) packed with Molsieve 13X to
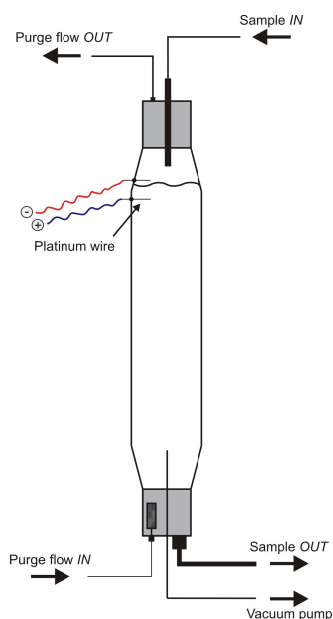
Figure 2.4. – Purge tower for VS1. The sample entry is located at the top, the exit at the bottom. The port for the vacuum pump connection is located sufficiently higher to avoid, that water rests are sucked into the pump. A platinum wire contact bridge controlls the fill hight of the sample water.

remove possible trace contaminations of carbondioxide, nitrogen oxides and oxygen (Figure A.1). The Nafion installed between valve 4 and 6 removes water traces from the purge process which might otherwise causes interferring or ghost peaks in the chromatogram. The signal processing between the ECD and the computer is performed by a CBM-Box . All used settings about temperatures, times, flows and packing materials are listed in table 2.1.

2.3.3. Chromatograms of M84

The retention time of SF_6 in a standard run was $112\,sec$ and $218\,sec$ for CFC-12 (Figure B.2). For a water sample the retention time of SF_6 was shifted to a longer retention time of $116\,sec$ whereas the CFC-12 was identically retained as in a standard run (Figure B.3). All peeks were baseline seperated with a symmetric (gaussian) behaviour which implies no tailing or shifting. The blank runs showed no ghost peaks and no short term baseline shift or other chromatographic artefacts (Figure B.1).

Table 2.1. – Used settings of *VS1* during M84.

Setting	Value
Carrier flow[*]	$10\,\frac{ml}{min}$
Make up flow	$15\,\frac{ml}{min}$
Purge flow[**]	$120\,\frac{ml}{min}$
Nafion	$120\,\frac{ml}{min}$
Trapping temp.	$-60\,to-70°C$
Heating temp.	$130°C$
Purge time	$10\,min$
Heating time	$30\,sec$
Injection time	$30\,sec$
Trap	$70\,cm$ Hayesep D
Precolumn	$30\,cm$ Porasil C
Column	$180\,cm$ Carbograph 1AC
	$20\,cm$ Molsieve 5Å

[*] Measured at ECD exit, valve 7 inject, heater on, (minus Make up flow).

[**] Measured at *VS* exit, valve 4 and 6 inject, trap set to $-60°C$.

2.3.4. Measurement system post cruise

Besides the breakdown of the ECD the *VS1* measurement system has displayed some fundamental flaws during the cruise of M84. In the old set up of the system when the valves are switched to the purge and trap process, the purge flow was going through valve 4 over the trap into the precolumn before it exits at *VS* (Figure A.1). So if there are ECD sensitive components which are not hold in the trap then they will be retained at the precolumn maybe during the whole purge process without exiting the system. This components might enter the main column during the injection process causing a wide ghost peak right at the beginning of the chromatogram (Figure B.3). This ghost peak sometimes interfere with the SF_6 peak and lead to a loss of baseline seperation. The second disadvantage of this setup is the flow resistence of the precolumn. For a sufficient purge efficiency it is indispensable to have a purge flow of at least $110 - 120 \frac{ml}{min}$. This was only attainable with a prepressure of $> 5\,bar$. Due to a accumulation of waste components in the precolumn the pressure once reached $7\,bar$ which causes an explosion of the purge tower. This dangerous occurrence showed clearly the susceptibillity of the old measurement system.

To get rid of these two problems an additional 6 port 2 ways valve (no. 8) was installed between valve 7 and the precolumn (Figure A.2). During the purge and trap process valve 8 is switched to inject so that the purge flow exits at T without going through the precolumn. In addition to this the precolumn is backflushed the whole time of the purge and trap process by an additional flow coming from the flow regulator. In this case the precolumn is not contaminated with waste components but rather cleaned by the backflush. Without the resistence of the precolumn while trapping, the prepressure could be reduced to $1.8\,bar$ within a purge flow of $115\frac{ml}{min}$. The wide ghost peak did not appear again until the last measurements onshore in october and the risk of a purge tower explosion is also minimized.

Even with those two main flaws removed there were still two ghost peaks which disturbed the chromatographic application flow. One appeared right before the SF_6 peak, sometimes baseline seperated. The second one appeared $5\,min$ after the CFC-

12 peak as a huge wide ghost peak with a width of at least $10\,min$. The total size of both peaks seems to depend on the depth the sample was taken from. In some deep water samples neither the first nor the second ghost peak appear. For a precise determination of the components of the ghost peaks it is necessary to use another GC system like a GC-MS or GC-MSMS which were not available in the tracer laboratory.

Nevertheless, another precolumn and column setup was invented to solve the problem (Table 2.2). This setup allows a stable baseline seperation between the first ghost peak and the SF_6 peak. The second huge ghost peak appears now $30\,min$ after the CFC-12 peak. The main factor of retaining this component is the Molsieve 5Å. Due to further length extensions of the molsieve packing of the precolumn it would be possible to have a sufficient seperation in the precolumn to avoid the entry into the main column and thus into the ECD. This have not been done yet because of shortage of time but will be performed during fall 2011. If it is a successful modification the chromatographic procedure will be less than $6\,min$ which leads to a complete measuring time of $15\,min$ per sample.

Another modified part of the post cruise measurement system is valve 7. The 4 port 2 ways valve is replaced by a 6 port 2 ways valve with an additional needle valve regulating or rather influencing the carrier flow when valve 7 is in load position. With this needle valve one can simulate the resistence of the heated trap and precolumn, following that there is always the same carrier flow regardless if the valve is switched to inject or load position. The difference of the flows with the old system was between $6-10\,\frac{ml}{min}$ what implied that after the chromatogram started and valve 7 was switched to inject the carrier flow was abruptly reduced due to the resistence of trap and precolumn and rebuilded when valve 7 was switched back to load position. These pressure fluctuations were shown by dips in the chromatogram and a distinctive tailing of the CFC-12 peak.

Table 2.2. – Used settings of *VS1* post cruise.

Setting	Value
Carrier flow*	$20 \frac{ml}{min}$
Make up flow	$10 \frac{ml}{min}$
Purge flow**	$115 \frac{ml}{min}$
Nafion	$260 \frac{ml}{min}$
Backflush flow***	$30 \frac{ml}{min}$
Trapping temp.	$-60 \, to - 70°C$
Heating temp.	$90°C$
purge time	$10 \, min$
heating time	$30 \, sec$
injection time	$60 \, sec$
trap	$70 \, cm$ Hayesep D
Precolumn	$60 \, cm$ Porasil C
	$10 \, cm$ Molsieve 5Å
Column	$180 \, cm$ Carbograph 1AC
	$30 \, cm$ Molsieve 5Å

* Measured at ECD exit, valve 7 inject, heater on, (minus Make up flow).

** Measured at *VS* exit, valve 4, 6 and 8 inject, trap set to $-60°C$.

*** Measured at *VS* exit, valve 6 and 8 inject.

2.3.5. Measuring procedure with cracker

To measure the sealed ampoules the purge tower was replaced by a cracker unit (Figure 2.5). All samples were stored in a warm water bath of $60°C$ for at least 24 hours to improve the purge efficiency by driving the components into the head space.

In the first step, the sample is fixed in the ampoule housing and the sealed glas neck is hold by a screw-nut with nylon gasket in the cracking chamber. Afterwards valve 4 is switched to inject and the whole chamber is flushed for $5\,min$ with the purge flow to remove all contaminating components. Then valve 4 is switched back to load postion and the top of the ampoule neck gets cracked by the cracking paddle. The purge rod is inserted down into the ampoule and it is very important that the rod touches the glas bottom. The nitrogen then exits between the end of the rod and the glas surface and is finely divided into small bubbles. These bubbles go through the whole ampoule stripping the CFC-12 and SF_6 out of the water and head space. If the rod does not touch the bottom, there will be a few big bubbles going through the middle of the ampoule with a very poor and insufficient purge efficiency. A statistical approach has to be follwed to determine the tracer concentration of the sample [Schneider et al., 2010]. After this has been done the program gets started and the purge and trap process begins. The purge time is the same used with the purge tower because the SF_6 will break through the trap using longer purging times. The valve switching program is also quite the same used during the cruise but with a lower end temperature of the heated trap (reasons will be explained later on) and a longer injection time of valve 7 due to the longer precolumn setup. The nafion flow was set to $260\,\frac{ml}{min}$ because of a higher water vapour fraction in the purge flow. This higher vapour fraction results from the high temperature of the heated samples. All further parameters are shown in table 2.2.

Each sample was purged two times to ensure a sufficient purge efficiency. Due to this double purging and the wide ghost peak after the CFC-12 peak the measurement time for one sample was more than one hour.

The cracked ampoules were weighed right after replacing them from the cracker
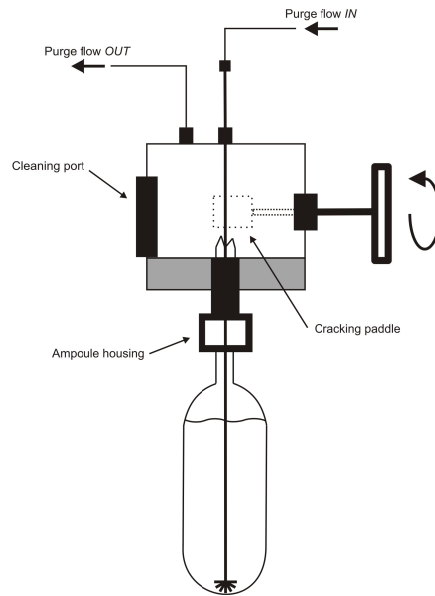
Figure 2.5. – Ampoule cracker. The ampoule is hold in the ampoule housing. After flushing the chamber, the ampoule neck gets cracked by the metal paddle and the purge rod is inserted down to the bottom.

housing. Then the ampoules were emptied through a net to catch the glass splinters from cracking. Afterwards the ampoules were rinsed with destilled water, the glass splinters were sorted back into the ampoules and put into a drying cabinet for 48 hours. As last step, the ampoules were weighed a second time, now in an empty state, in order to quantify the mass of the sample.

2.3.6. Concentration ratio between water and head space

The share of the tracer concentration in the head space and in the water can be estimated with the ideal gas equation (Equation 2.1) and the solubility functions of the tracers (Equation 1.1).

$$n = \frac{p\,V}{R\,T} \tag{2.1}$$

Each flame sealed ampoule consists of the sample water of $\approx 300\,ml$ and a head

space of $\approx 40\,ml$. The head space consists of pure nitrogen direct after the sealing. A sample from the surface layer might have a temperature of $20\,°C$ and a salinity of 38.00. Assuming that the concentration of CFC-12 is $\approx 500\,ppt$ and the SF_6 concentration $\approx 7\,ppt$, it is possible to determine the total amount of substance (Equation 2.2) of the tracers in the sample water by rewriting equation 1.2.

$$n_1 = pTracer_1 \cdot F(T,S)_{Tracer} \cdot V_1 \tag{2.2}$$

The amount of substance for CFC-12 is $n_{1,CFC-12} = 0.356\,pmol$ and for SF6 $n_{1,SF6} = 0.3804\,fmol$. These are the absolut values of moles in the whole glas ampoule ($340\,ml$). Each thermodynamic system strives to equilibrium which means that the dissolved trace gases are outgassing until the partial pressure in the head space is equal to the partial pressure in the water. The ampoules are stored over weeks at room temperature, following that one can assume that the partial pressure reached the equilibrium state. The partial pressure of the tracers in the water ($pTracer_1$) is given by equation 2.2. The partial pressure in the head space can be described by equation 2.3 ($pTracer_2$).

$$pTracer_2 = \frac{n_2\,R\,T}{p\,V_2} \tag{2.3}$$

The volume V_2 is the volume of the head space ($40\,ml$) and p the mean atmospheric pressure of $1\,atm$. At equilibrium both partial pressures must be equal (Equation 2.4). The total amount of substance is described by equation 2.5.

$$pTracer_1 = pTracer_2 \qquad (2.4)$$

$$n = n_1 + n_2 \qquad (2.5)$$

Equation 2.4 yields an expression of the equilibrium state (Equation 2.6). The total amount of moles in the head space and in the sample water can be determined by combining equation 2.5 with 2.6 to 2.7.

$$\frac{R\,T\,F\,V_1}{p\,V_2} = \frac{n_1}{n_2} \qquad (2.6)$$

$$n_1 = \frac{X \cdot n}{1 + X} \qquad with \qquad X = \frac{R\,T\,F\,V_1}{p\,V_2} \qquad (2.7)$$

The results are that more than $99.57\,\%$ of CFC-12 and more than $99.97\,\%$ of SF_6 are in the head space after the ampoules have been sealed and the equlibirum is reached. The heating to $60\,°C$ might have a relatively small additional effect of the concentration ratio, but it is impossible to determine this effect for $60\,°C$. The higher the temperature the higher the pressure and for higher pressure values there are no solubility functions available. Nevertheless, there are two advantages of heating the ampoule before cracking. The higher pressure leads to a blasting of the glass cone while cracking and no glass splinters can block the glass neck. The second adavantage is the fast expansion of the head space into the cracking chamber and thus also onto the trap.

2.3.7. Chromatograms of Cracker

The retention time in a standard run was $75\,sec$ for SF_6 and $183\,sec$ for CFC-12 (Figure B.5). For a cracked water sample the retention time of SF_6 was shifted to a longer retention time of $78\,sec$ and the CFC-12 was shifted to a shorter retention time of $180\,sec$ (Figure B.6). All peeks were baseline seperated but the SF_6 peak had a shifting for higher concentration and area counts respectively as well as the CFC-12 peaks were constant tailing regardless of the concentration. The blank runs showed no ghost peaks and no short term baseline shift but a small negative dip between $34 - 64\,sec$ (Figure B.4).

2.4. PT3

2.4.1. Hardware

The measurement system of *PT3* is also build in a similar stainless steel framework as the *VS1*. A further development compared to the older system is the valve chamber bonded with PVC plates which protect most of the valves from the wet and salty air on a shipboard use. Another advantage of this PVC bonding is a more stable temperature of the standard loops because no winds can go through the chamber. The technical equipment parts of this measurement system are shown in table E.2.

2.4.2. Measurement system during M84

The *PT3* measurement system (Figure A.3) is built up approximately the same as the *VS1* system. The differences to the *VS1* system are a different trap and purge system and also the samples are taken with syringes. The trap is cooled with ethanol to $-70°C$. It is fixed in the cooling chamber and the fill height of the ethanol is pressure regulated. The exact fill height of the ethanol is controlled by a swimmer in the chamber. This swimmer is connected to a metal rod which is inserted into a plastic tubing with magnetic sensors displaying the current fill height.

Purge flow *OUT*

Glass frit

Sample *IN / OUT*
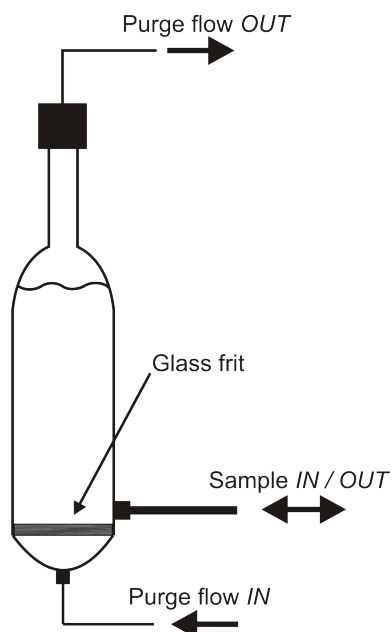
Purge flow *IN*

Figure 2.6. – Purge tower of PT3. The sample is filled in above the glass frit. The purge flow enters below the glass frit, goes through the water sample and exits at the top of the tower.

Before measuring, the sample syringes are also stored for $15\,min$ in a water bath of $35°C$ to improve the purge efficiency. Afterwards the syringe gets installed into a rack equipped with a calliper. The syringe is connceted to the purge ampoule (Figure 2.6) via PTFE capillarys and a three port manual valve. After resetting the zero point of the syringe with the calliper, valve 5 is switched to inject to vent the system, the three port valve is opened and the sample is filled into the purge ampoule. Then the three port valve is closed again and the inserted volume can be determined by the way the syringe core was pressed into the syringe shell. Each syringe has its own number and is volume callibrated. The next step is to switch valve 5 to load position and then start the program of the measurement system. The purge and trap process as well as the injection part is the same as for *VS1* described above. All setting parameters are shown in table 2.3.

Table 2.3. – Used settings of *PT3* during M84.

Setting	Value
Carrier flow[*]	$15\,\frac{ml}{min}$
Make up flow	$15\,\frac{ml}{min}$
Purge flow[**]	$120\,\frac{ml}{min}$
Nafion	$120\,\frac{ml}{min}$
Trapping temp.	$-70°C$
Heating temp.	$125°C$
Purge time	$10\,min$
Heating time	$30\,sec$
Injection time	$30\,sec$
Trap	$70\,cm$ Hayesep D
Precolumn	$30\,cm$ Porasil C
Column	$180\,cm$ Carbograph 1AC
	$20\,cm$ Molsieve 5Å

[*] Measured at ECD exit, valve 7 inject, heater on, (minus Make up flow).

[**] Measured at nafion exit, valve 4 and 6 inject, trap set to $-70°C$.

2.4.3. Chromatograms

The *PT3* system was not ready to measure when we went on the M84-3 cruise. The original plan was to finish the last few problems with the trap system on board and then starting test series with standard loops and water samples to conduct a few final tests. We made various test series with different column and precolumn setups but it was not possible to have a clear signal of the SF_6 peak. Either there was a wide and deep negative peak right at the retention time of SF_6 (Figure B.8) or the SF_6 peak was not baseline seperated with a small ghost peak (Figure B.7). Both chromatographic problems could not be solved on board, because the breakdown of the ECD of our main measurement system *VS1* at the same time provided further problems. The detector was the only part of the main system we had no spare part for due to the strict german regulations for ECDs. This regulation also prohibits to exchange the *VS1* ECD with the one of *PT3*. Due to the missing time for an extensive trouble shooting at the *PT3* system we decided after 48 hours trial and error to take the column setup of the *VS1*. At the end this allowed us to measure the CFC-12 with a clear and symmetric signal but without any signal for SF_6 (Figure B.9).

2.4.4. Measurement system post cruise

The complete setup of the post cruise *VS1* measurement system (Figure A.2) with all new improvements were adopted to the *PT3* system. One additional improvement was done for valve 8. The 6 port 2 ways valve was replaced by a 10 port 2 ways valve and the nafion entry and exit were connected to this valve (Figure A.4). The nafion is now regulated by valve 8 so that there is only a flow through the nafion during the purge and trap process. For all other processes the nafion flow is interrupted at two points so that the sensitive membrane of the nafion is not destroyed by a rising pressure in the outer layer while the system is in load position. Furthermore, there is no expensive ECD nitrogen gas wasted.

2.4.5. Trap - Problems and possible solutions

A systematic trouble shooting of the *PT3* system showed that the heater was too powerful for the Hayesep D packing of the trap. The heater had an effective power output of $300\,W$ which causes a very fast heating sequence. This extreme heating combined with the following dipping in the cold ethanol caused a decompostion of the Hayesep D packing. To solve the problem the effective power of the heater was now reduced to $150\,W$ and the maximum temperature of the PID was set to $90°C$. The trap is now first cooled above the cold ethanol bath before the fill level gets raised again for the next purge and trap process. First test series show, that the Hayesep D gets still damaged with this heating-cooling system. The new Hayesep D trap of the post cruise *VS1* system is very sensitive to temperatures above $90°C$ as well and we guess that the new type series of Hayesep D traps are not a good choice for ECD systems we are using. So the next steps are to try other packing materials, which could be used for this fast but coarse system of *PT3* also with regard to the trap efficiency of CFC-12, SF_6 and other ECD sensitive components. We suspect better temperature range compatibility with anorganic packing materials such as Molsieve 5Å or similar.

2.5. Data processing

2.5.1. Standard series and drift correction

The processed area counts of the measured electrical signals of a tracer need to be set in relation to a standard series. This standard series is created by standard gas, containing all used trace gases with a known concentration. Each measurement system is equipped with two standard loops into which the standard gas is loaded. A big loop *Vg* and a small loop *Vk* connected to V2 and V3 respectively (Figure A.1, A.2, A.3 and A.4,) with a known calibrated volume. With these two loops it is possible to load different volumes of standard gas onto the trap. This is done

by combining the two loops with each other or load them several times onto the trap. Even though the sample injection is different, the desorption and detection procedure is always the same as for a water sample. The maximum volume should be choosen in a way that the resulting amount of the area counts of the standard peaks is larger than the one of the tracers in water samples. With this relation between area counts and volumetric tracer concentration one can create a regression curve with the related equation (Figure 2.7). The standard series should be done at least every week to controll the reproducibility of the system. These standard series are only external standard measurements. For a trace level purge and trap system it is possible to use an internal standard but the needed system has not been installed yet. An ideal internal standard should be in the same medium as the analytes (e.g. water sample) and should have similar properties of interactions with the stationary phase (packing material) but with a different rentention time. Such an ideal tracer is very difficult to create without any contaminations of the water sample. A nearly ideal internal standard could be generated by loading a specfic amount of SF_5CF_3 standard gas (consisting of nitrogen and trifluoromethyl sulfurpentafluoride) onto the trap before the purge process of a water sample starts. In this case the internal standard can give informations about the desorption and detection process. Further descriptions about accurancy and robustness are given below.

The electron capture detectors always have a more or less periodic drift. This drift is determined by a *drift run* consisting of three runs with a standard volume of $Vg + Vk$. The drift run is executed before a new water sample series is started, then after each 10th sample and at the end of the whole run. The three runs of $Vg + Vk$ are indicating the current precision and the drift over the whole measuring time (Figure 2.8). Each measured value gets corrected by the obtained detector drift.

2.5.2. Purge efficiency and detection limit

The purge efficiency of all three types of purge chamber were determined in a similar way. The used samples were measured as many cycles until there was no more CFC-
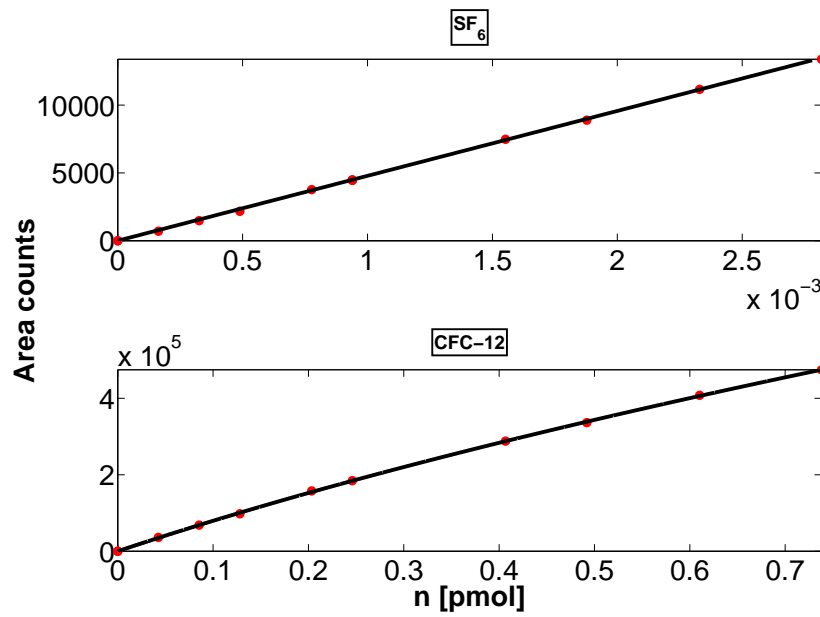
Figure 2.7. – Standard curve of SF_6 and CFC-12. The red dots indicate the measured data and the black solid line the regression curve.
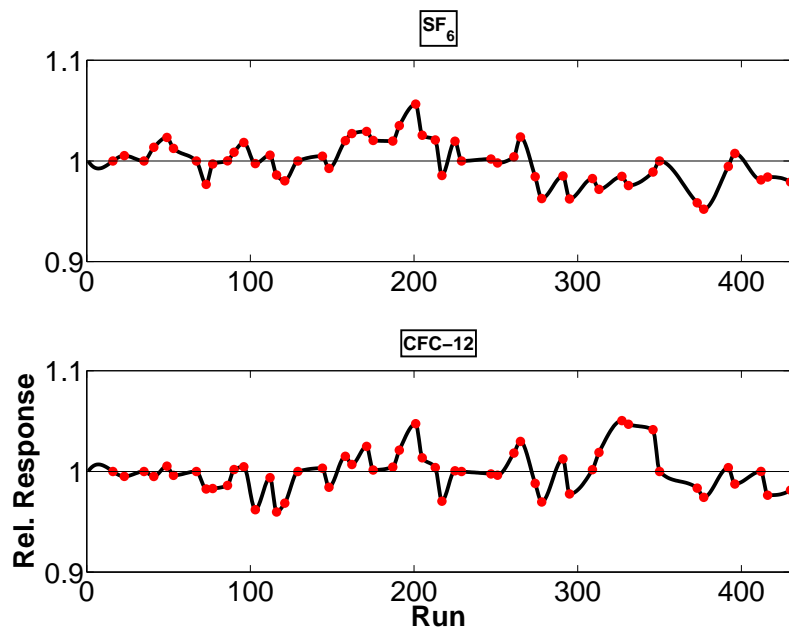
Figure 2.8. – Drift correction for SF_6 and CFC-12. The red dots indicate the measured data and the black solid line the interpolation between the obtained data.

Table 2.4. – Purge efficiency of all purge chambers.

Purge chamber	Purge efficiency		n
	SF_6	CFC-12	
Purge tower of VS1	$100\,\%\,(-0.22)$	$99.8\,\%\,(\pm 0.02)$	3
Purge tower of PT3	$100\,\%\,(-3.6)$	$99.2\,\%\,(-3.6)$	1
Cracker*	$100\,\%\,(-0.48)$	$99.6\,\%\,(\pm 0.08)$	6

* After two purges.

12 and SF_6 left in the water and head space. The number of area counts of the first purge and the first two purges of the cracker system respectively were devided by the total number of area counts from all purges needed. The relatively high uncertainty for the purge tower of PT3 are due to only one measured purge efficiency on the cruise. Comparable tests from past cruises showed a purge efficiency of $96.4\,\%$. A further point to mention is that the ppt values for CFC-12 measured with this system are showing a clear undersaturation (offset) of $3\,\%$ which indicates that the purge efficiency must be lower than determined on board. Due to a very high work load there is less data for these kind of statistics which shows clearly the absolutely indispensability of a sufficient statistic data set. The results are shown in table 2.4. The detection limits are $0.03\,\frac{fmol}{kg}$ for SF_6 and $0.02\,\frac{pmol}{kg}$ for CFC-12. The detection limit of SF_6 is the reason for the higher error range than for CFC-12 values. One would expect that the gases in the head space are well mixed and the CFC-12 concentration shows an exponential decrease after several purges. SF_6, by contrast, is no more detectable after the first purge, but it should have the same exponential decrease in the head space.

2.5.3. Precision, robustness and accuracy

The precision is determined by double water samples from the same niskin bottle. Due to the same fact mentioned above there is not such a comprehensive statistical data set, but these few values are very similar to the precision values of other cruises

Table 2.5. – Precision of all measurement systems.

System	Precision		n
	SF$_6$	CFC-12	
VS1	1.0 %	0.65 %	3
PT3	/	0.34 %	3
Cracker	2.5 %	1.4 %	1

where these measurement systems were used (Table 2.5) The robustness of the purge tower is very good even then when the same type but another tower is used. The purge efficiency is not effected by any change of one of these towers. Regarding the purge tower of PT3 there are no results yet. However, the trap and the other column parts are not robust. Each measurement system has its own character in tubing systems with different lengths and types of valves and not every column or trap working good for system 1 does so for system 2.

The accuracy is not easy to determine. There are many error sources which might effect the measurements. The tightness of the niskin bottles plays an important role. If there is any leaking bottle the obtained values may have an error. To avoid this error source it is very useful to have a leaking list for each station so that bad data can be quality flagged later on. The next source influencing the accuracy is the operator of sampling. Everyone has his/her own sampling technique and some are more accurate watching out for bubbles in the sample than others. The accuracy of the measurement itself is affected by the calibration of the fill high in the purge tower, the volume calibration of each syringe and the accuracy of the calliper. The used standard gas was calibrated against the *Gold-Standard*[2] with an error of $\Delta_{CFC-12}P = \pm 0.98\,ppt$ and $\Delta_{SF_6}P = \pm 0.01\,ppt$. The standard loops were calibrated against a known volume, but, however, the determined error values have not been available yet.

Even if a standard measurement has a low error range it is still an external standard so that possible measuring errors can not be investigated for water samples. Following

---

[2]Marine air from Trinidad Head, California
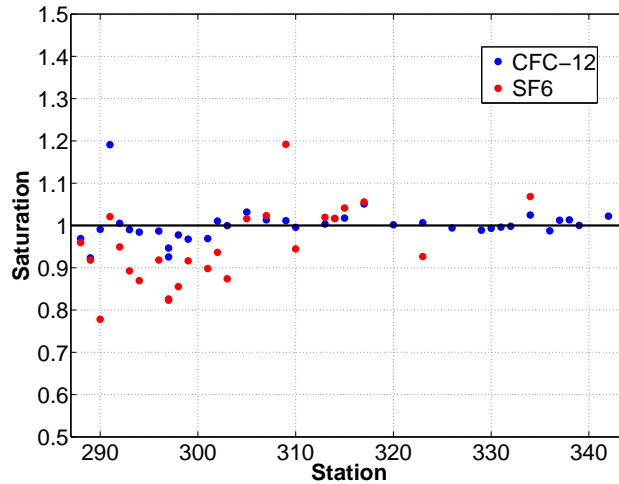
Figure 2.9. – Saturation of SF_6 (red dots) and CFC-12 (blue dots) for $depth < 25\,m$. The black line describes a saturation of $100\,\%$.

that neither a stable offset nor other errors like the influence of other gases to the ECD detection sensibility can be determined. One way to estimate (roughly) the accuracy is to calculate the saturation of SF_6 and CFC-12 in the upper mixed layer (depth<25m) where both tracers should have a saturation of $100\,\%$ (Figure 2.9). The disadvantage of this estimate is that there are several reasons for the deviation of a saturation of $100\,\%$ like the physical properties of water or upwelling areas of older (undersaturated in relation to the atmosphere) water masses. There is may be also a small accuracy offset of the salinity and temperature values which are used to calculate the partial pressure of a tracer. Even if the saturation is $100\,\%$ and the used parameters are well determined there are further uncertainties for deeper layers. For example components with a varying concentration in the water column which can effect the sensibility of the ECD detector mentioned above. Maybe one can obtain a significant error of the accuracy for a large surface data set with $n > 100$ minimizing some zonal effects of under- or oversaturation. An extensive error calculation was not performed yet, because of less statistic data. The error estimation and calculation will be more in focus on following cruises to have a more detailed background of errors and error sources.

2.5.4. Used software

All used software (licensed) can be found in table 2.6.

Table 2.6. – Used software.

Software	Version
Data processing and analysis	MatLab R2011a
Operating system of IBM Laptop (*PT3*)	Windows XP SP3
Operating system of Toshiba Labtop (*VS1*)	Windows 3.11
Shimadzu software of GC2014 (*PT3*)	GC Solution 2.41
Shimadzu software of GC-14A (*VS1*)	Shimadzu CLASS CR10
Valve control (*VS1*)	TurboBasic 1.0
Valve control (*PT3*)	LabView 8.5

2.6. Constraining the TTD

In theory, it is very easy to define the exact TTD ratios for the 1D-model with two tracers. A plot of the mean ages of CFC-12 vs. the mean ages of SF_6 for different ratios shows the relation between the two tracer (e.g. figure C.1). The mean ages lying on the bisecting line describe the best fitting TTD ratio. Such a plot based on the whole data set is not significant due to a high scattering of the values. Furthermore, this approach does not make any differences in space and one recieve only a rough estimation for the whole data set.

A more detailed ratio estimation is done by calculating the difference of each tracer mean age couple for each specific ratio and data point. The ratios can be subdivided into parts of 0.2 from 0.4 to 1.6. Lower ratios than 0.4 are rare due to the high advective share and in the same way, ratios higher than 1.6 are also rare due to the high diffusity share. The best fitting ratio is described by the ratio wich is belonging to the minimum of the absolut mean age differences. However, even this estimation still does not provide correct $^\Delta/_\Gamma$ ratios (Figure 2.10). Only data fitting to case 1 provide exact $^\Delta/_\Gamma$ ratios given by the intersection at $y = 0$. Obtained data belonging
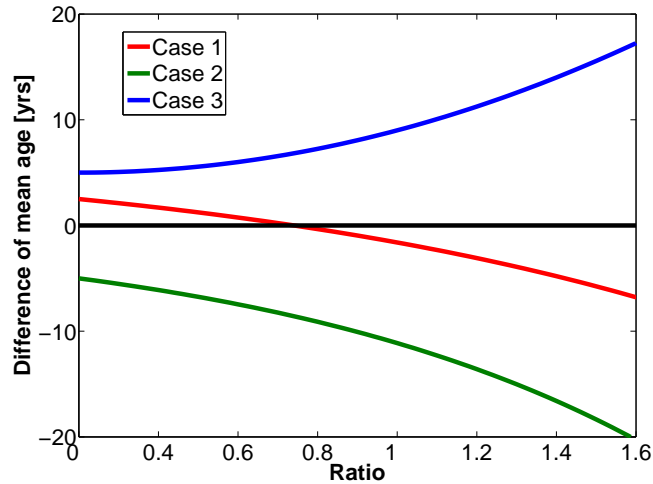
Figure 2.10. – Mean age vs. $^\Delta/_\Gamma$ ratio describing good and bad data for the used tracer couple. Case 1 (red curve) fits into the validity area of the tracer couple. Case 2 (green curve) and 3 (blue curve) show characteristics of non fitting data.

to case 2 or 3 can not be described by the $^{SF_6}/_{CFC-12}$ tracer couple and lead to wrong results. The ratio belonging to the minimum of case 2 and 3 always tends to zero. This would describe a water parcel with no mixing and diffusion.

To eliminate data belonging to case 2 or 3, the exact validity area of the used tracer couple has to be determined. Related to this, it is important to have a detailed look at the atmospheric history of both tracers and the resulting restrictions. Therefore a plot of tracer age vs. mean age for both tracers is a very meaningful concept (Figure 2.11).

The decrease of the CFC-12 concentration in the atmosphere leads to a restriction of the data range since any concentration between $532.49 - 546.7\,ppt$ describes two points in the time history between $1994 - 2011$ and is therefore of limited use. Following this, the lower limit of CFC-12 ages is set to $\geq 18\,yrs$ which as well implies a minimum tracer age for SF_6 of $\geq 15\,yrs$. The upper limit of $\leq 55\,yrs$ is defined by the intersection of both curves where the atmospheric concentration of SF_6 just started to increase but was still near zero.

As described in the introduction, the mean age depends on the $^\Delta/_\Gamma$ ratio, following that one can create several of these age vs. mean age plots such as figure 2.11. Figure
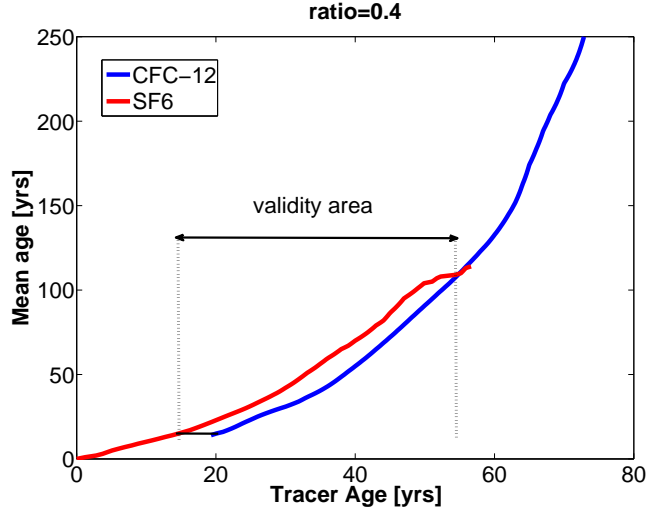
Figure 2.11. – Validity area of SF_6 (red curve) and CFC-12 (blue curve) at ratio=0.4. The validity area is indicated by the two black dashed lines.

2.12 shows the same type of plot for $^\Delta/_\Gamma$ ratios of 0.4, 0.6, 0.8, 1.0, 1.2 and 1.4. The curve couple of CFC-12 and SF_6 belonging to a specific ratio are identically coloured. The upper curve belongs to SF_6 and the lower one to CFC-12.

The slope of both curves increases to a different degree from lower to higher ratios. This includes that the mean difference of $Tracer\,Age_{(CFC-12)} - Tracer\,Age_{(SF_6)}$ also increases from lower to higher ratio. This is visualized in figure 2.12. The tracer age of SF_6 is fixed at $45\,yrs$ showed by the grey solid line, whereas the CFC-12 age is hold variable. The related mean age of the fixed SF_6 age increases with an increasing $^\Delta/_\Gamma$ ratio. Following that the CFC-12 age belonging to this determined mean ages increases, which is shown by the dashed grey line. Related to this, the difference of $Tracer\,Age_{(CFC-12)} - Tracer\,Age_{(SF_6)}$ (Equation 2.8) increases as well, shown by the yellow horizontal lines.

$$Diff_{(tracerage)} = Tracer\,Age_{(CFC-12)} - Tracer\,Age_{(SF_6)} \qquad (2.8)$$

The age difference can be obtained for all $^\Delta/_\Gamma \neq 0$. If such an age difference with
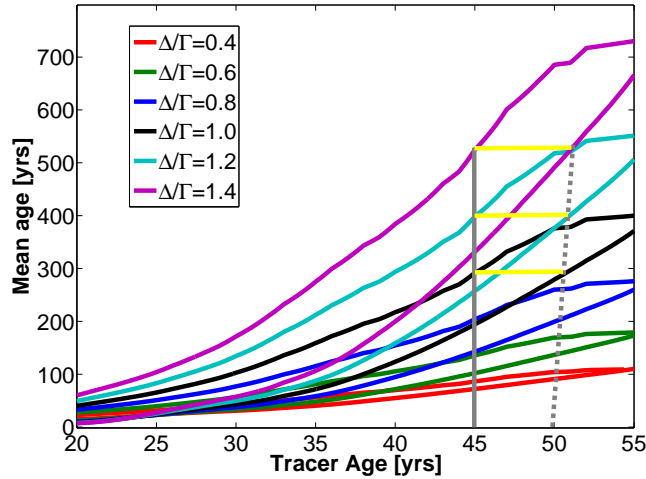
Figure 2.12. – Validity areas for different $^\Delta/_\Gamma$ ratios (colour seperated). The lower and upper limit of the x-axis is related to the validity area of the tracers. The upper curve of a colour couple is the SF_6 curve and the lower one the CFC-12 curve. The yellow lines indicate the difference of the two tracer ages related to the specific mean age value.

the belonging two tracer ages fits into one of the given age vs. mean age relations (Figure 2.12), case 1 in figure 2.13 and 2.10 occurs and the mean age as well as the width are exactly determined for the 1D-TTD model. Case 2 in figure 2.13 and 2.10 occurs when the CFC-12 age is smaller than the SF_6 age, following that the more the ratio increases the more the negative difference increases. Case 3 occurs for a too large age difference with an increasing mean age difference for increasing ratios.

The 1D-TTD-model is basically a framework for tracer couples and the significance of each couple is restricted by its validity area. If there is some data which is not fitting into the validity area of the used tracer couple it does not mean that the 1D-TTD-model is wrong at all. But if other tracer couples do not fit into their validity areas as well, another expression of G should be used (e.g. 2IG-TTD model).
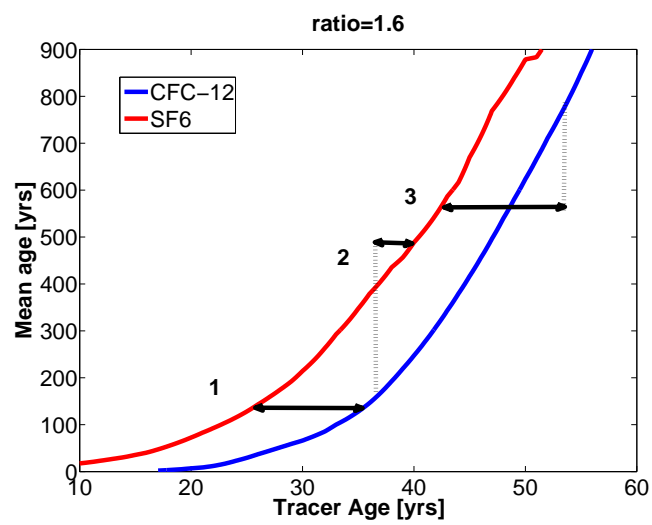
Figure 2.13. – Possible relations between age couples. Case 1 describes data fitting into the validity area, whereas case 2 and 3 show non fitting data.

3. Results

3.1. TTD - Ratio determination

The plots of CFC-12 mean age vs. SF_6 mean age coloured by depth of all the specific sea areas are shown in the appendix C. Except for the Western Mediterranean, all plots show good correlations. Figure 3.1 shows all available data points of station vs. depth coloured by ratio. Figure 3.2, however, shows only the data points which are allowed for this tracer couple and TTD-model. All other data points violating the restriction are excluded. Based on this data set a statistical analysis was carried out. For all stations which ratios are not determinable, the ratio is set to $\Delta/\Gamma = 1.0$.

Table 3.1. – Best ratios for the Mediterranean Sea.

| Area	Depth	Δ/Γ
Ionian Sea	complete	0.8
Levantine Sea	$0 - 1700\,m$	0.8
	$1700\,m - bottom$	0.6
Adriatic Sea	$0 - 600\,m$	1.2
	$600\,m - bottom$	0.6
WMed, Aegean	complete	1.0 (undefined)
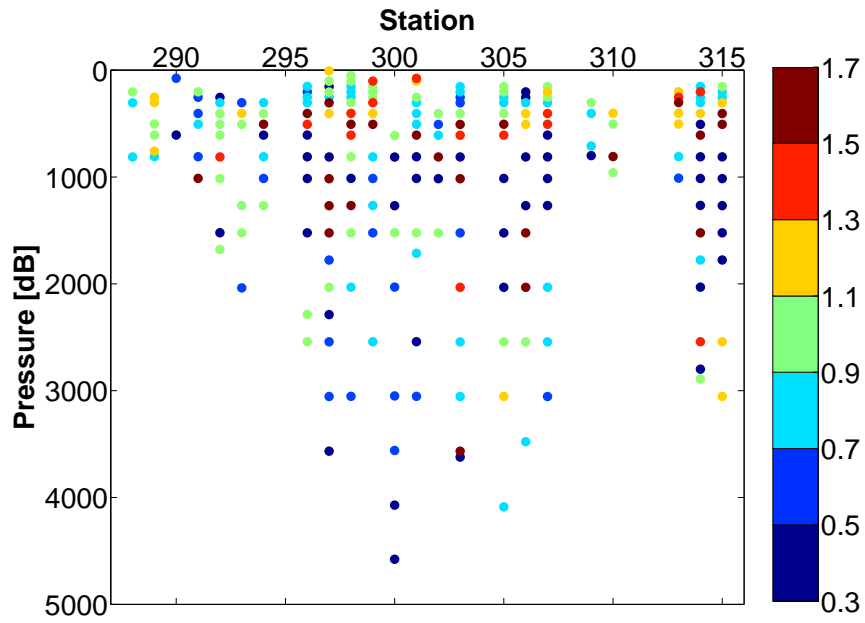
Figure 3.1. – Statistical determined best fitting ratios with no restrictions. Non perfect fitting data allowed.
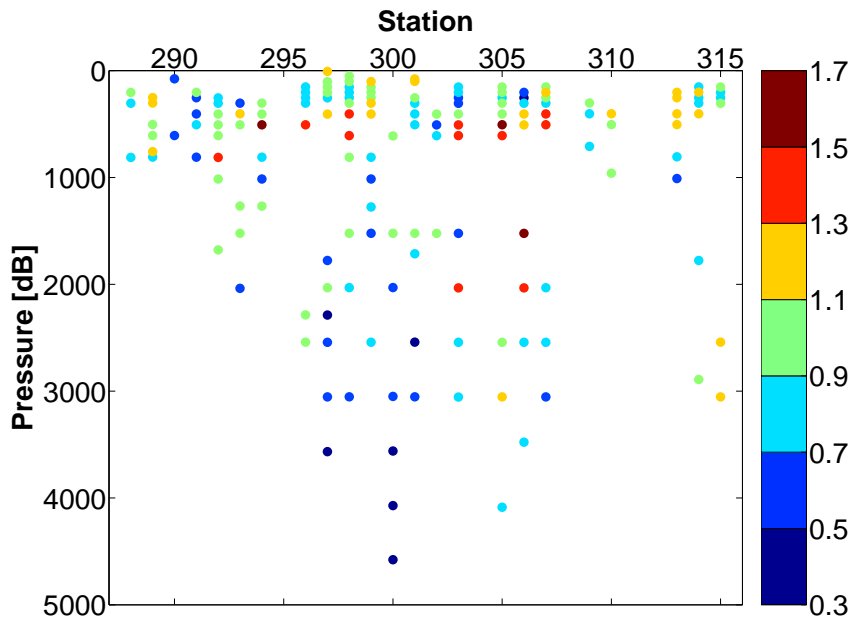
Figure 3.2. – Best fitting ratios based on the exact scope of the tracer couple. Bad data points are eliminated.

3.2. Eastern Mediterranean Sea
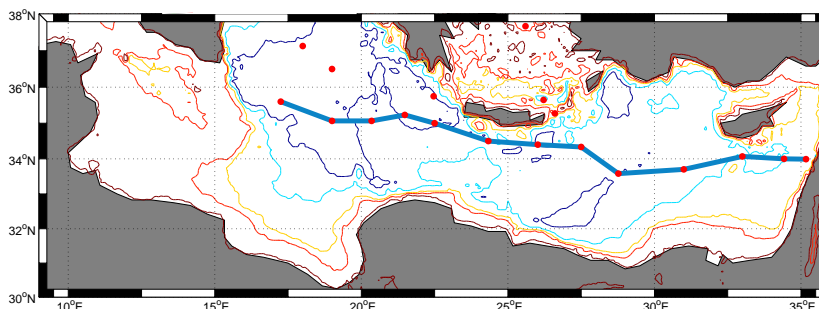
Figure 3.3. – Ionian and Levantine Sea. The SF$_6$ and CFC-12 section is indicated by the blue line. The depth contours are 500 m, 1000 m, 2000 m and 3000 m.

The concentration of a tracer is presented as partial pressure (*ppt*) in the following sections. This has the advantage that influences by temperature and salinity need not be considered. All results of gravimetric concentrations and tracer ages can be found in the appendix D.

The salinity range of the Levantine Sea below $500\,m$ ($> 40\,yrs$) lies between $38.75 - 38.83$ (Figure 3.4 and 3.5). The potential temperature reaches from $13.5\,°C$ to $14.1\,°C$. The upper layer between $250 - 500\,m$ ($\approx 10 - 40\,yrs$) is characterized by salinities between $\approx 38.85 - 39.25$ and a temperature range (Θ) of $13.9 - 16.8\,°C$. The densest water ($\sigma_2 \approx 37.9\,\frac{kg}{m^3}$) is indicated by a salinity of 38.78, $\Theta = 13.5\,°C$ and a mean age between $50 - 60\,yrs$. The Ionian Sea is characterized by a salinity range of $38.72 - 39.10$ and a potential temperature of $13.4 - 14.9\,°C$ below $500\,m$ and mean age $> 30\,yrs$ (Figure 3.6 and 3.7). Salinities between $38.95 - 39.12$ with $\Theta = 14.4 - 16.0\,°C$ are present in the intermediate layer ($250 - 500\,m$, $< 30\,yrs$). The densest water ($\approx 37.9\,\frac{kg}{m^3}$) is indicated by a salinity of 38.75, $\Theta = 13.4\,°C$ and a mean age between $50 - 60\,yrs$. Figure 3.12 shows the salinity of the whole EMed section. Below $600\,m$ the salinity lies between $38.74 - 38.90$. The salinity maximum is restricted to intermediate depth between $150 - 500\,m$ in the Ionian Sea and reaches the

surface at the Cretan Passage and the eastern part of the Levantine Sea. A salinity minimum is shown at the surface in the western Ionian Sea with values < 38.5.

A tracer minimum zone (TMZ) of CFC-12 can be found in the Levantine Sea. The TMZ is located at core depths between $600 - 1500\,m$ with a concentration of $120 - 150\,ppt$. The smallest concentrations in the Ionian Sea are also found in this layer with values $< 200\,ppt$. The Levantine and Ionian deep water layers ($> 2000\,m$ and $> 1500\,m$ in the western Ionian Sea) are characterized by higher concentration values $> 210\,ppt$. The Ionian Basin shows also a clear maximum at bottom depths in the most western part of $\approx 250\ ppt$ below $3000\,m$ (Figure 3.8). The concentration distribution of SF_6 is more homogeneous than the one of CFC-12. Concentrations $< 2\,ppt$ are found below $600\,m$ throughout the whole EMed. There are also slightly higher values of more than $2\,ppt$ at bottom depth in the western Ionian Basin and a maximum core $> 1.5\,ppt$ at station 299 ($\approx 22°30'E$) at $2000\,m$ depth (Figure 3.9).

Figure 3.10 and 3.11 show the mean ages of CFC-12 and SF_6 for the best ratio approach of the TTD. The oldest water can be found in the Levantine Sea at depths between $600 - 1500\,m$ with mean ages between $80 - 110\,yrs$. Furthermore, mean ages between $70 - 80\,yrs$ can be found in the same intermediate layer in the Ionian Sea. The CFC-12 mean ages are decreasing from $80\,yrs$ to $< 50\,yrs$ down to the bottom starting at $1600\,m$ depth. The SF_6 section has two deviant mean age characteristics of the intermediate layer ($\geq 70\,yrs$). Between $18°40'E - 22°00'E$ and $26°00'E - 28°20'E$ the mean ages of $60 - 70\,yrs$ reach down to $3100\,m$ and $2700\,m$ depths respectively.
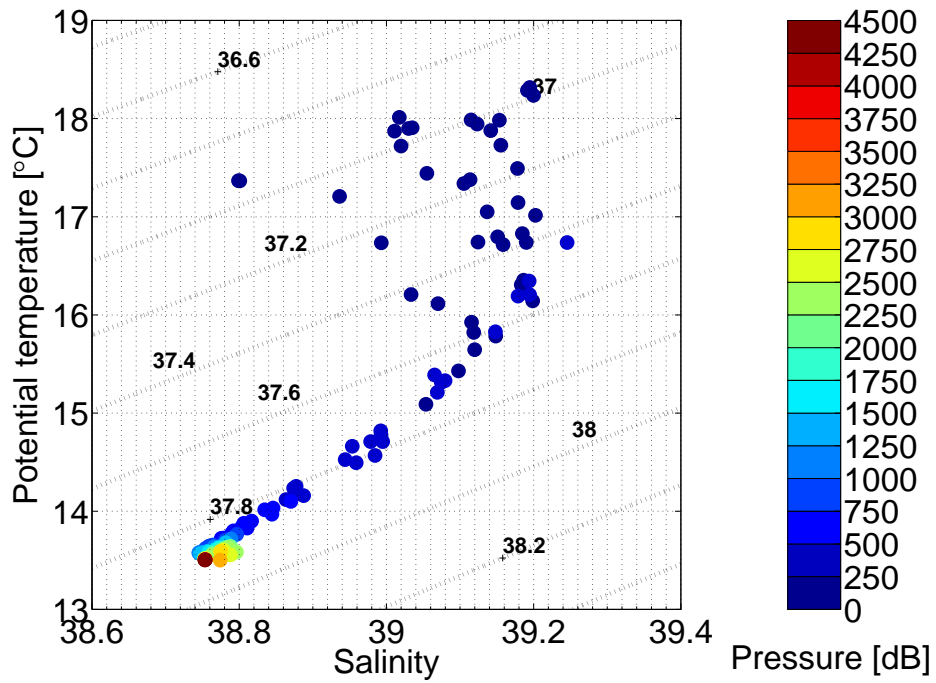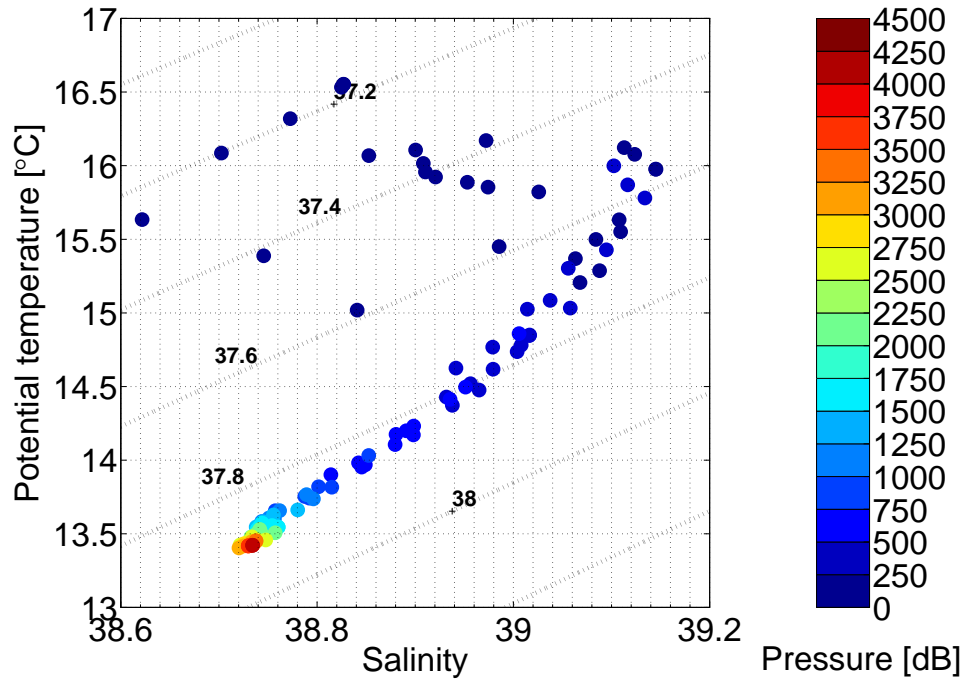
Figure 3.4. – Salinity vs. potential temperature plot of the Leveantine Sea coloured by depth. The isopycnals are based on σ_2.
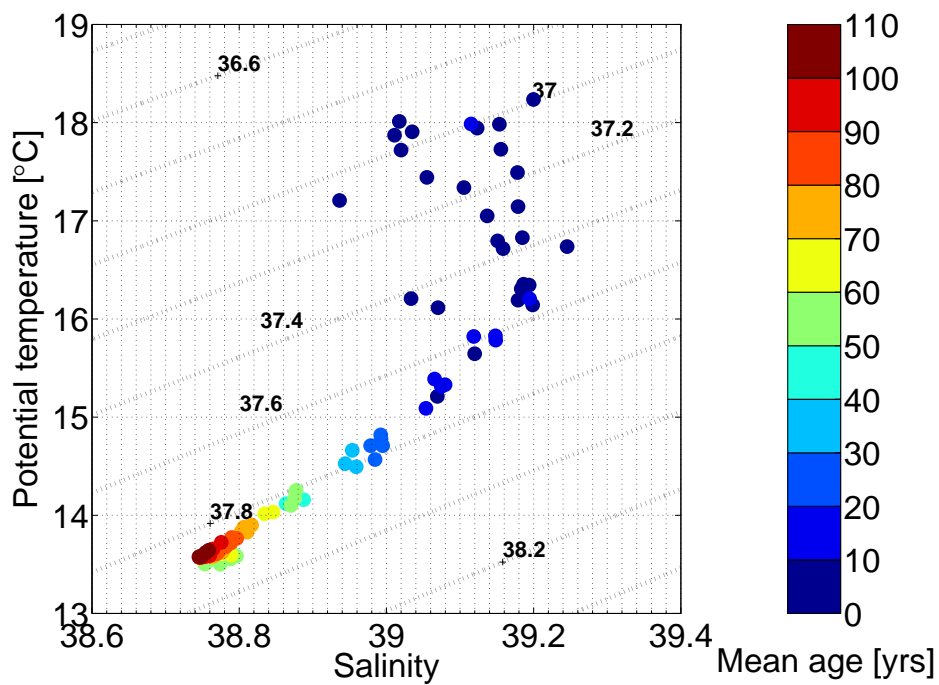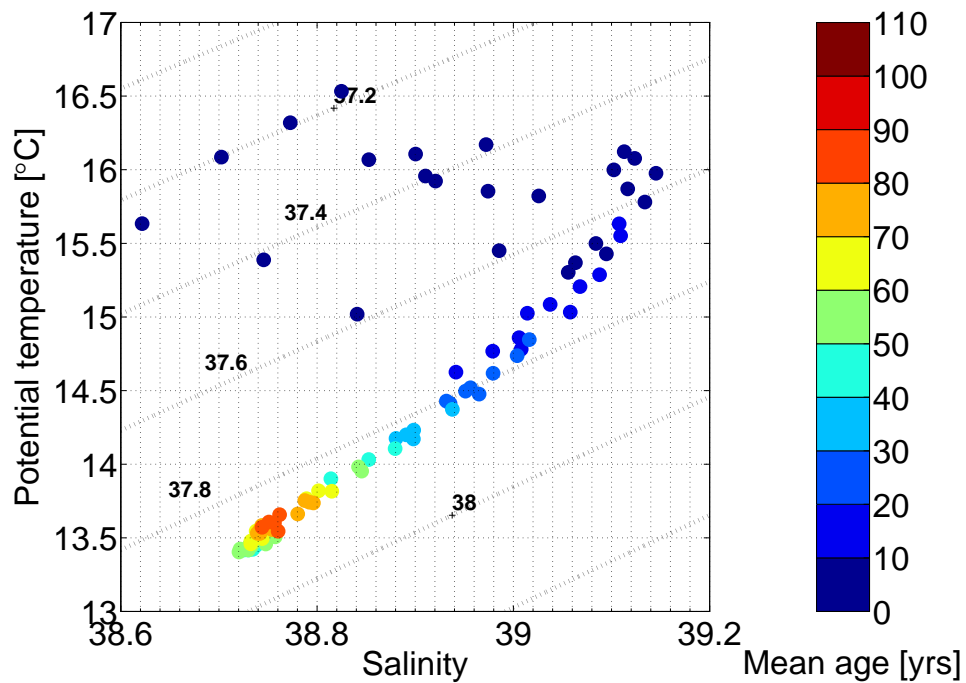

Figure 3.5. – Salinity vs. potential temperature plot of the Leveantine Sea coloured by CFC-12 mean age. The isopycnals are based on σ_2.
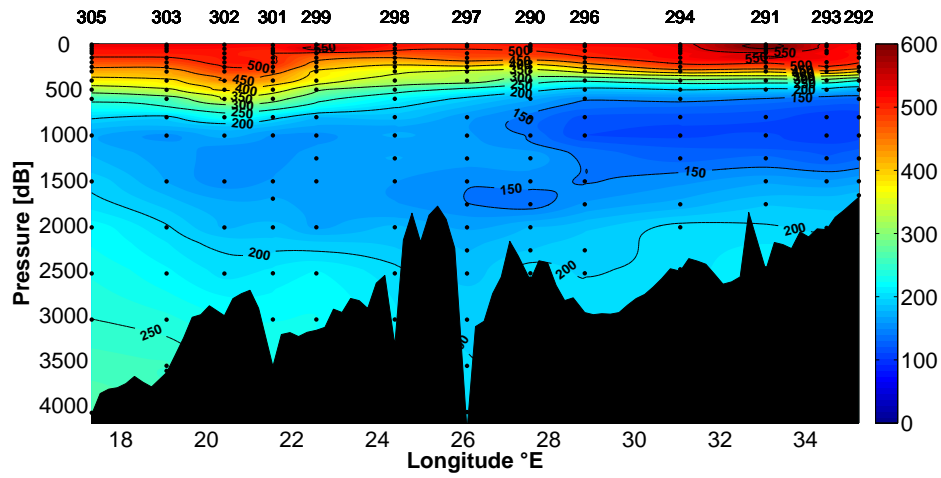
Figure 3.6. – Salinity vs. potential temperature plot of the Ionian Sea coloured by depth. The isopycnals are based on σ_2.

Figure 3.7. – Salinity vs. potential temperature plot of the Ionian Sea coloured by CFC-12 mean age. The isopycnals are based on σ_2.

Figure 3.8. – EMed: Partial pressure of CFC-12 in *ppt* with a contour line fragmentation of $50\,ppt$ and a colour contouring of $10\,ppt$.
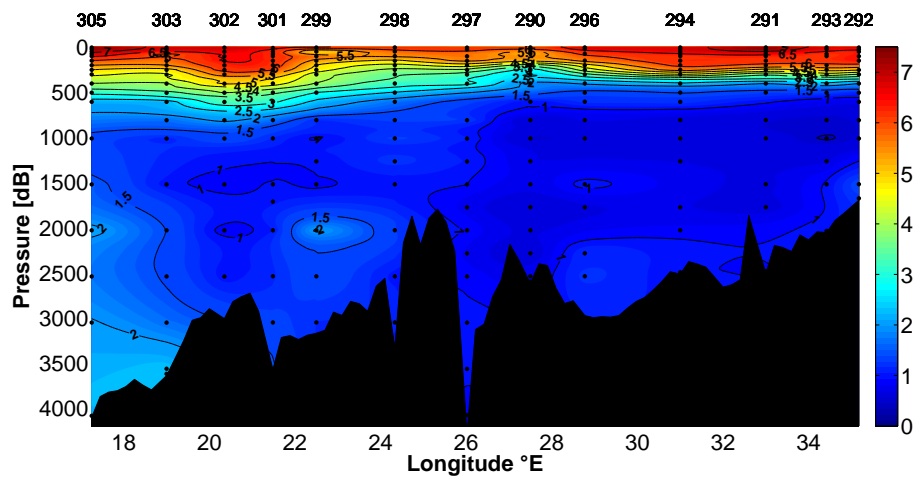
Figure 3.9. – EMed: Partial pressure of SF$_6$ in *ppt* with a contour line fragmentation of $0.5\,ppt$ and a colour contouring of $0.1\,ppt$.
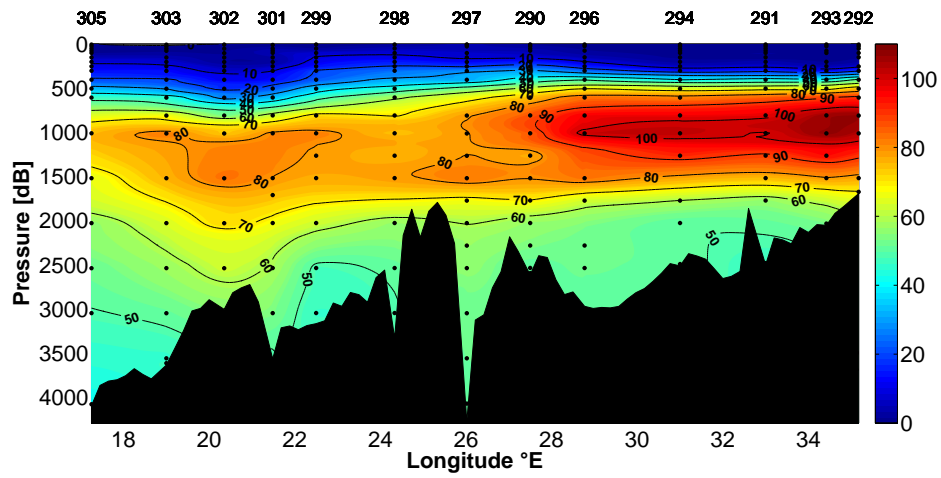
Figure 3.10. – EMed: Mean ages of CFC-12 in yrs with a contour line fragmentation of $10\,yrs$ and a colour contouring of $1\,yr$.
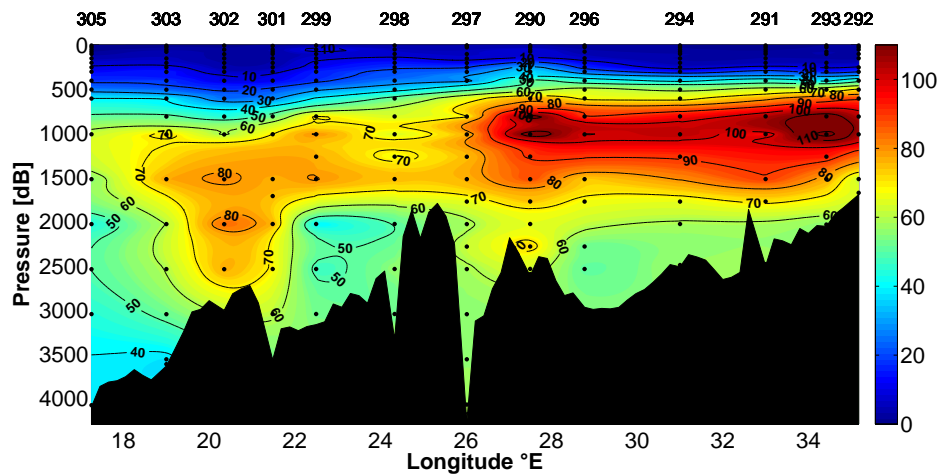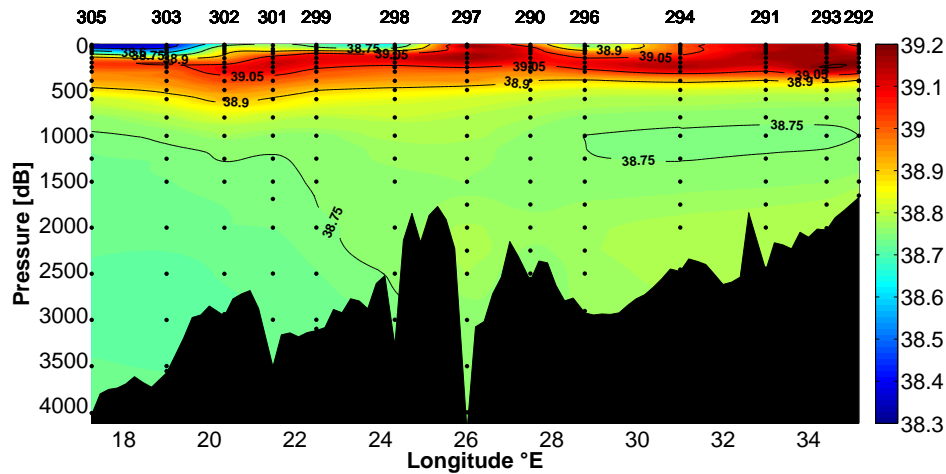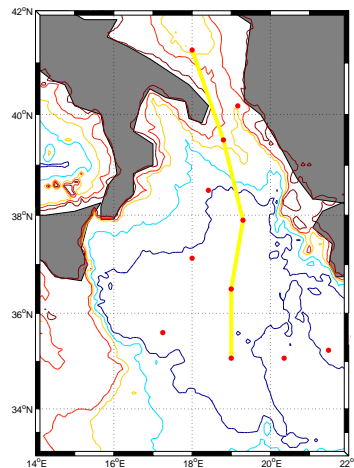

Figure 3.11. – EMed: Mean ages of SF_6 in yrs with a contour line fragmentation of $10\,yrs$ and a colour contouring of $1\,yr$.

Figure 3.12. – EMed: Salinity with a contour line fragmentation of 0.15 and a colour contouring of 0.01.

3.3. Northern Ionian Sea

Figure 3.13. – Northern Ionian Sea. The SF_6 and CFC-12 section is indicated by the yellow line. The depth contours are 500 m, 1000 m, 2000 m and 3000 m.

The Northern Ionian Sea has a salinity range of $38.71 - 38.93$ below $500\,m$ $(> 30\,yrs)$ (Figure 3.14 and 3.15). The potential temperature reaches from $13.4\,°C$ to $14.4\,°C$. The intermediate layer between $250 - 500\,m$ $(\approx 10 - 30\,yrs)$ is characterized by salinities between $38.71 - 39.02$ and a Θ range of $13.4 - 15.4\,°C$. The densest water

($\sigma_2 \approx 37.9 \frac{kg}{m^3}$) is indicated by a salinity of 38.74, $\Theta = 13.4\,^\circ C$ and a mean age between $50-60\,yrs$. There is a salinity minimum < 38.60 at the surface $(0-100\,m)$ followed by a maximum > 38.9 between $150-600\,m$ in the Northern Ionian Sea (Figure 3.20). A relative homogeneous salinity layer of ≈ 38.75 characterizes the whole water column below $1000\,m$.

Both Northern Ionian section plots of the partial pressure of CFC-12 and SF_6 show more or less the same concentration gradients (Figure 3.16 and 3.17). In the following descriptions the CFC-12 sections will be used and the SF_6 concentration will be stated in brackets.

The surface layer with concentrations between $540-450\,ppt$ $(7.5-5.5\,ppt)$ reaches down to $200\,m$. The intermediate layer of the Northern Ionian Sea lies between $200-500\,m$ with a concentration of $450-300\,ppt$ $(5.5-3\,ppt)$. In deeper water layers below $600\,m$, the concentration is smaller than $250\,ppt$ $(2.5\,ppt)$ with two TMZ's between $800-2300\,m$ ($35\,^\circ N$, station 303 and $38\,^\circ N$, station 307) and concentrations $< 150\,ppt$ $(< 1\,ppt)$. In the southern part of the Northern Ionians Sea are slightly higher concentrations in the bottom waters $(> 3000\,m)$ of more than $250\,ppt$ $(2.2\,ppt)$. The upper layer down to $600\,m$ has quite the same mean ages for both tracers between $0-35\,yrs$ (Figure 3.18 and 3.19). The mean ages of the TMZ's have a difference of $10\,yrs$ with a CFC-12 mean age maximum of $> 85\,yrs$. For the deep water layer $> 2000\,m$ the mean ages differ only slightly in space but not in time.
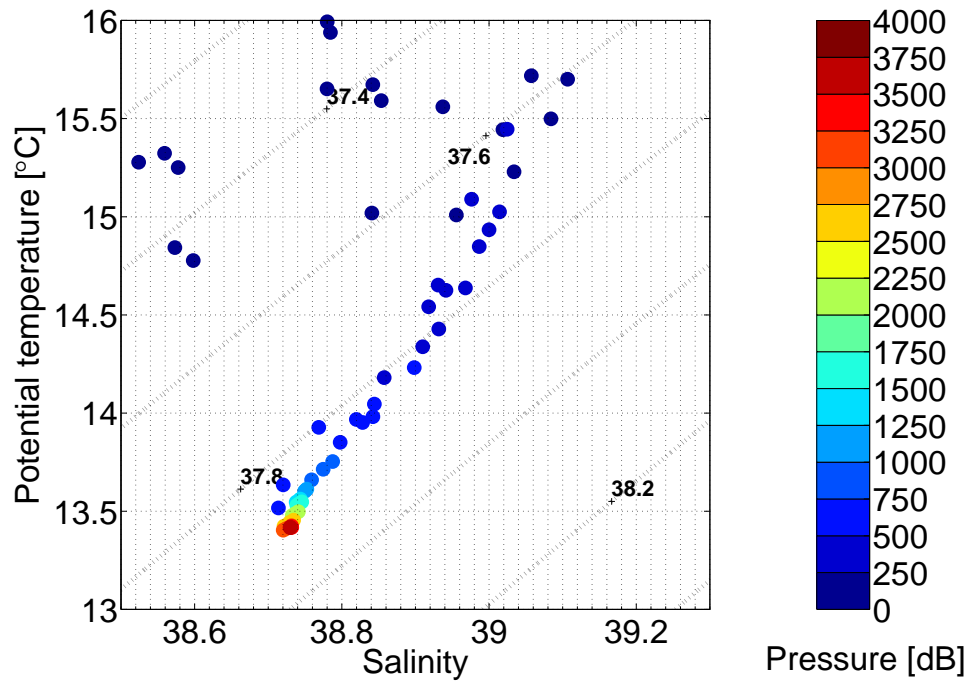
Figure 3.14. – Salinity vs. potential temperature plot of the Nothern Ionian Sea coloured by depth. The isopycnals are based on σ_2.
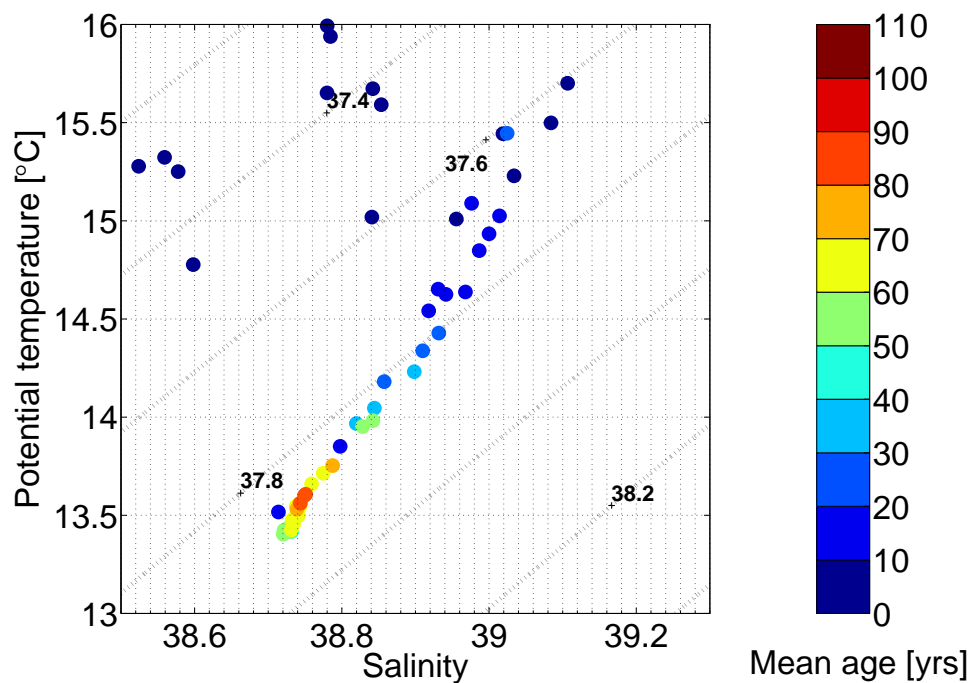

Figure 3.15. – Salinity vs. potential temperature plot of the Northern Ionian Sea coloured by CFC-12 mean age. The isopycnals are based on σ_2.
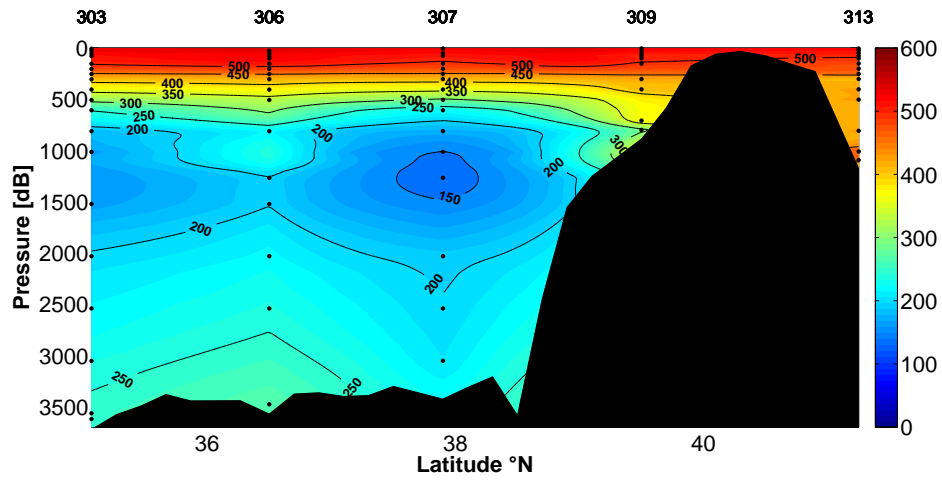
Figure 3.16. – Northern Ionian Sea: Partial pressure of CFC-12 in *ppt* with a contour line fragmentation of 50 *ppt* and a colour contouring of 10 *ppt*.
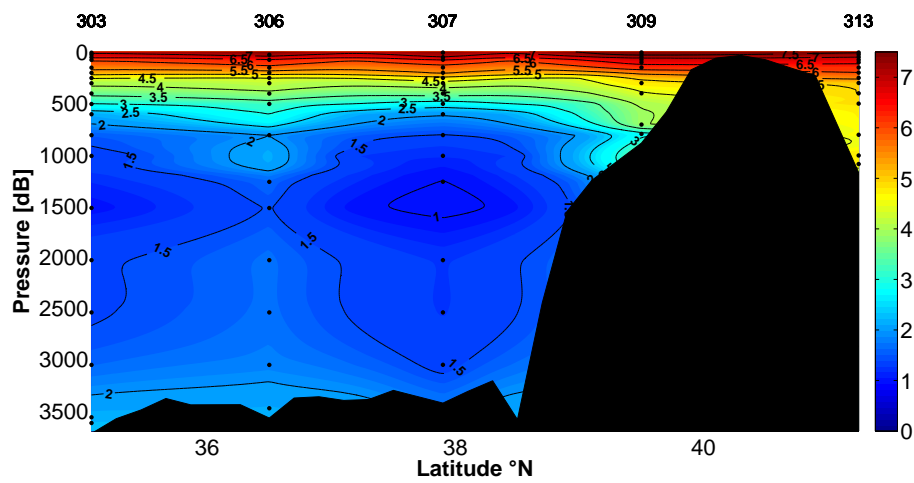
Figure 3.17. – Northern Ionian Sea: Partial pressure of SF_6 in *ppt* with a contour line fragmentation of 0.5 *ppt* and a colour contouring of 0.1 *ppt*.
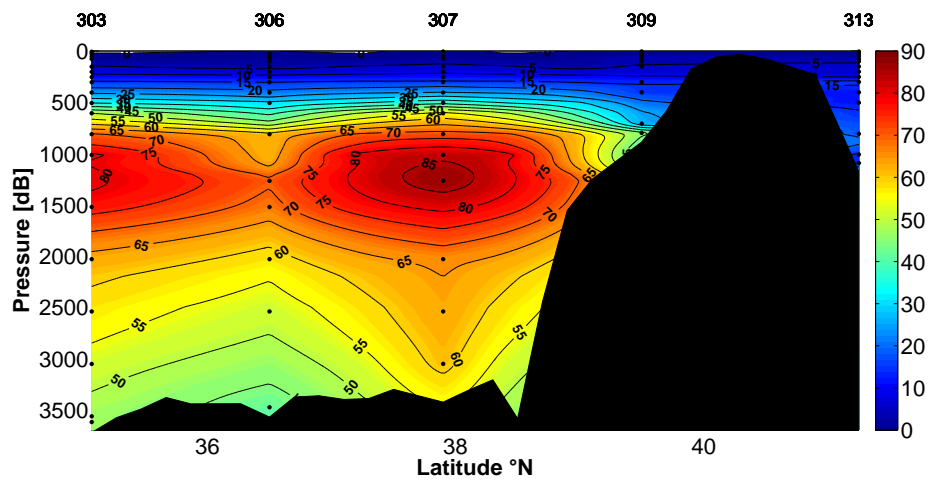
Figure 3.18. – Northern Ionian Sea: Mean ages of CFC-12 in yrs with a contour line fragmentation of $5\,yrs$ and a colour contouring of $1\,yr$.
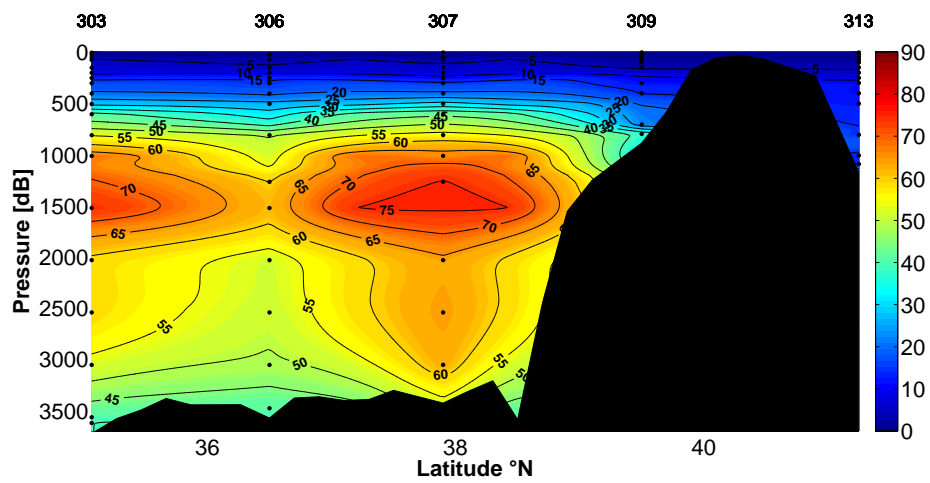
Figure 3.19. – Northern Ionian Sea: Mean ages of CFC-12 in yrs with a contour line fragmentation of $5\,yrs$ and a colour contouring of $1\,yr$.

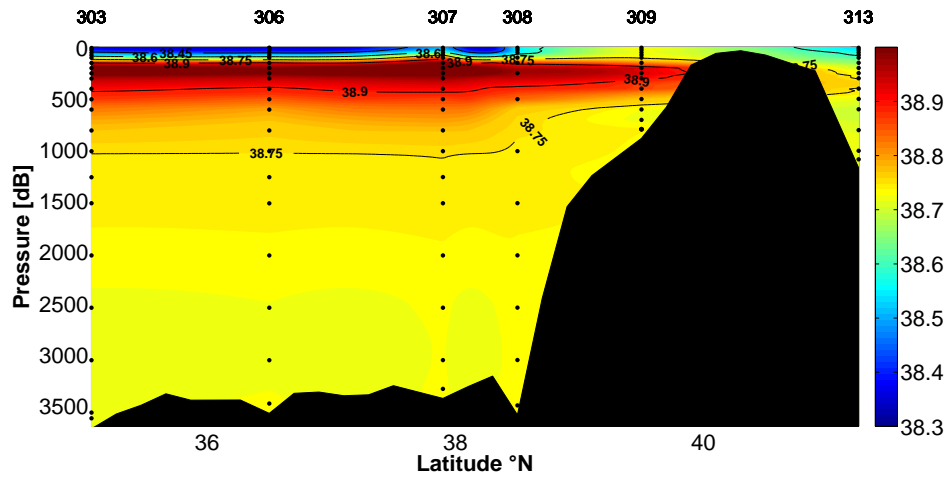**Figure 3.20.** – Northern Ionian Sea: Salinity with a contour line fragmentation of 0.15 and a colour contouring of 0.01.

3.4. Southern Adriatic Sea
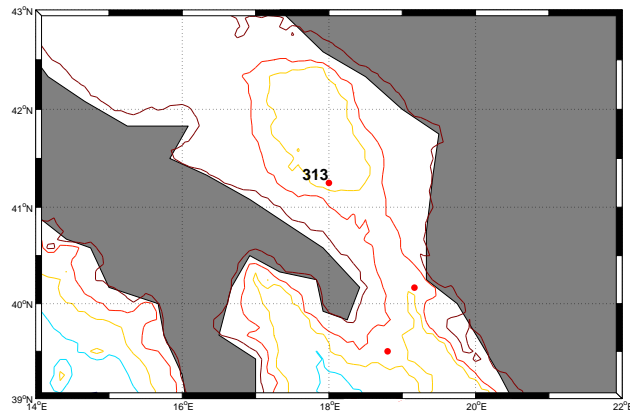
Figure 3.21. – Southern Adriatic Sea. Station 313 is the only sample point. The depth contours are 500 m, 1000 m, 2000 m and 3000 m.

The salinity lies between $38.71 - 38.76$ for depths below $400\,m$. The potential temperature reaches from $13.1°C$ to $13.7°C$. The upper layer between $50 - 400\,m$ has salinity values between $38.56 - 38.69$ with a potential temperature of $13.6 - 14.1\,°C$. The densest water ($\sigma_2 \approx 38\,\frac{kg}{m^3}$) is characterized by a salinity of 38.73, $\Theta = 13.1\,°C$

and a SF$_6$ mean age of $7\,yrs$ (Figure 3.22, 3.23 and 3.29). The partial pressure of both tracers is very high in the Southern Adriatic Sea throughout the whole water column with a minimum at $\approx 300\,m$ of $378\,ppt$ CFC-12 and $4.54\,ppt$ SF$_6$ (Figure 3.24, 3.25). All other values are $> 430\,ppt$ for CFC-12 and $> 5\,ppt$ for SF$_6$, respectively. Due to the direct relation between partial pressure and tracer age follows that the tracer ages of CFC-12 are $< 22\,yrs$ and those of SF$_6$ $< 10\,yrs$ for the main body of the water column (Figure 3.26, 3.27). Most of the mean ages are $< 10\,yrs$ and both tracer mean ages are equal (Figure 3.28). Furthermore the mean ages differ only slightly from the SF$_6$ age.
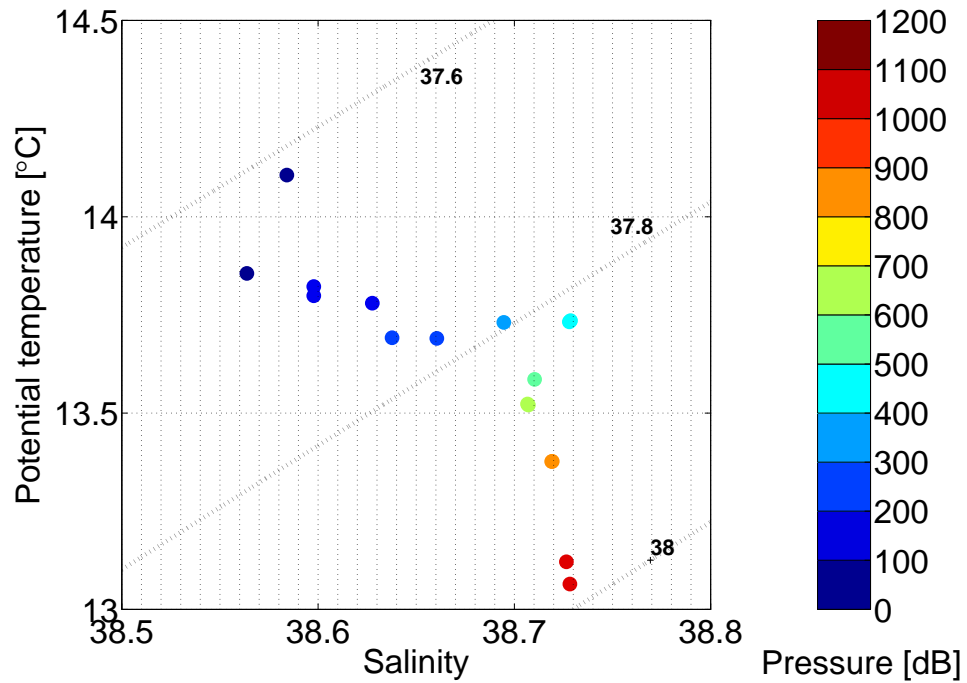
Figure 3.22. – Salinity vs. potential temperature plot of the Southern Adriatic Sea coloured by depth. The isopycnals are based on σ_2.
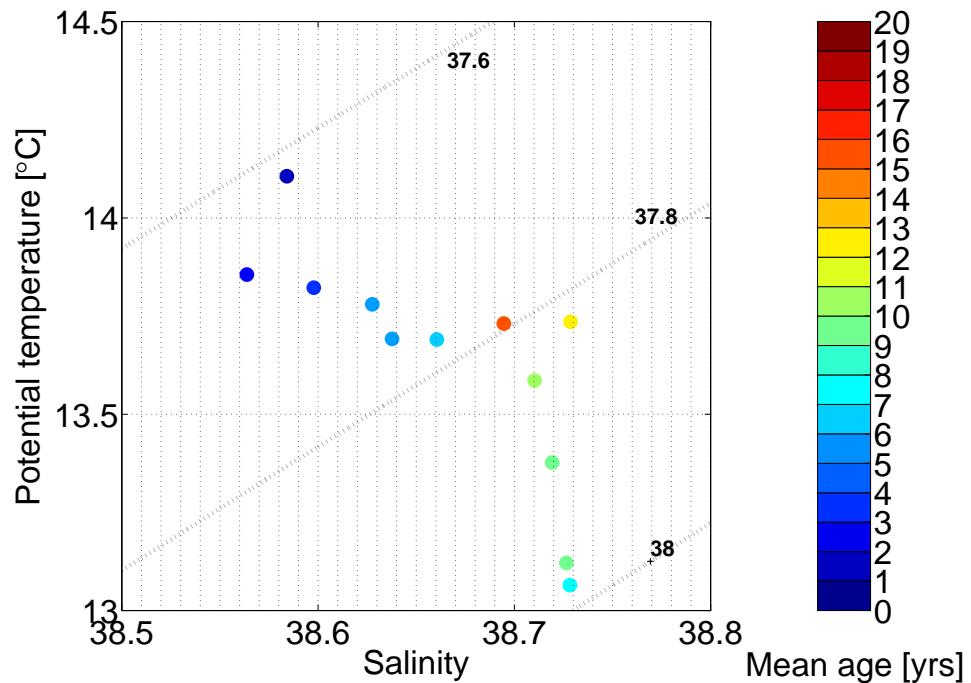
Figure 3.23. – Salinity vs. potential temperature plot of the Southern Adriatic Sea coloured by SF_6 mean age. The isopycnals are based on σ_2.
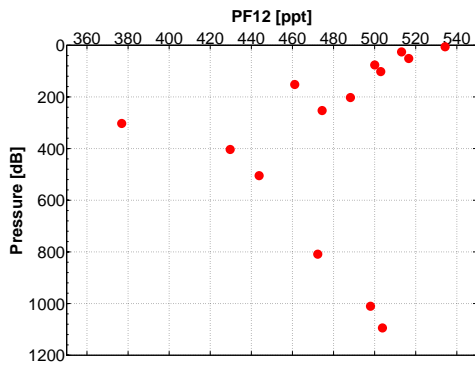
Figure 3.24. – Southern Adriatic Sea: Partial pressure of CFC-12 in *ppt*.
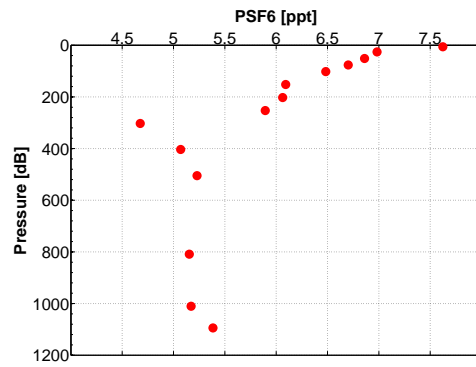
Figure 3.25. – Southern Adriatic Sea: Partial pressure of SF$_6$ in *ppt*.
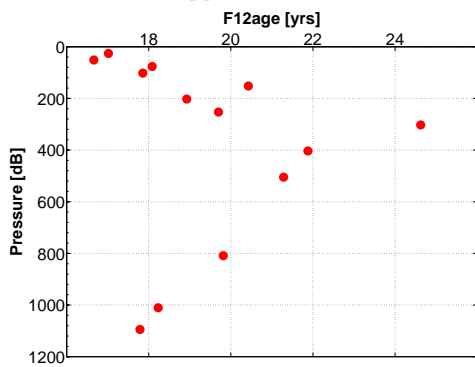
Figure 3.26. – Southern Adriatic Sea: Tracer age of CFC-12 in *yrs*.
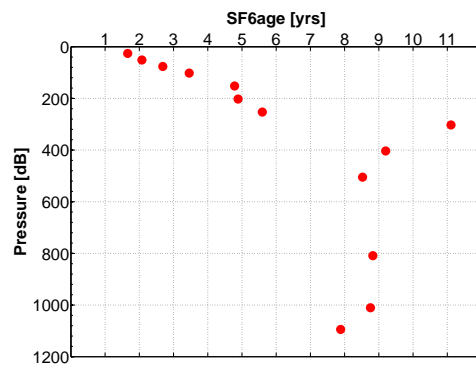
Figure 3.27. – Southern Adriatic Sea: Tracer age of SF$_6$ in *yrs*.

Figure 3.28. – Southern Adriatic Sea: Mean age of SF$_6$ in *yrs*.

Figure 3.29. – Southern Adriatic Sea: Salinity.
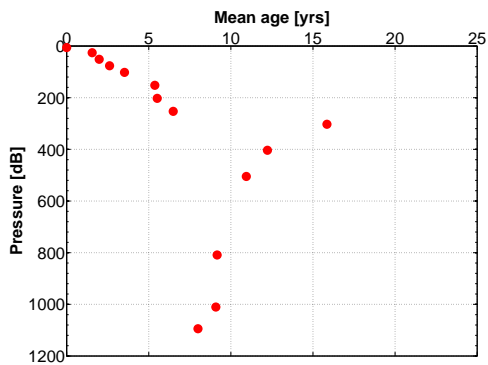
3.5. Aegean and Cretan Sea
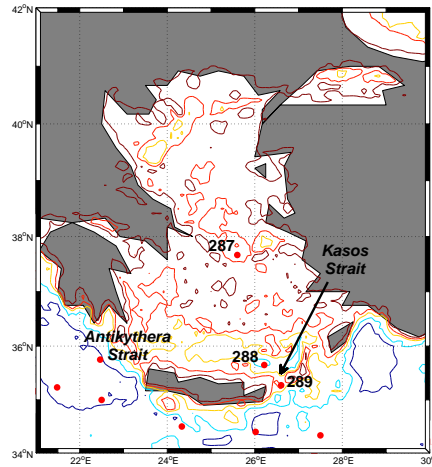
Figure 3.30. – Aegean and Cretan Sea. The Antikythera and Kasos Strait are the connections to the Ionian and Levantine Sea. The depth contours are 500 m, 1000 m, 2000 m and 3000 m.

The Aegan and Cretan Sea are characterized by salinity values between $38.98 - 39.23$, a potential temperature range of $14.0 - 17.6\,°C$ and SF_6 mean ages from $0 - 16\,yrs$. The densest water is indicated by a salinity of 39.05 and $\Theta = 14\,°C$ (Figure 3.31 and 3.32). The concentration of CFC-12 lies between $1.1 - 1.7\,^{pmol}/_{kg}$ and the SF_6 concentration reaches from $0.6 - 1.55\,^{fmol}/kg$. Station 288 only has a clear concentration gradient of SF_6. However, station 287 and 289 show no clear concentration profile of neither CFC-12 nor SF_6 (Figure 3.33, 3.34, 3.35 and 3.36). The mean age of SF_6 increases from surface to bottom from $0 - 40\,yrs$ at station 288. The mean ages of CFC-12 and SF_6 at the other two stations scatter from $0 - 16\,yrs$ over the whole water column (Figure 3.37).

Figure 3.31. – Salinity vs. potential temperature plot of the Aegean and Cretan Sea coloured by depth. The isopycnals are based on σ_2.

Figure 3.32. – Salinity vs. potential temperature plot of the Aegean and Cretan Sea coloured by SF_6 mean age. The isopycnals are based on σ_2.
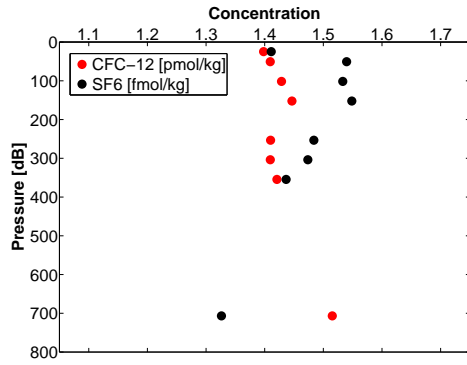
Figure 3.33. – Aegean Sea: Concentration of CFC-12 (pmol/kg) and SF$_6$ (fmol/kg) at station 287.
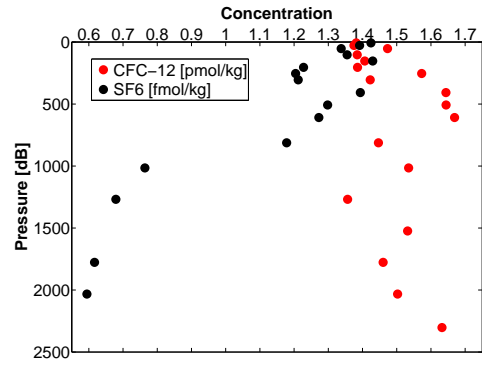
Figure 3.34. – Cretan Sea: Concentration of CFC-12 (pmol/kg) and SF$_6$ (fmol/kg) at station 288.
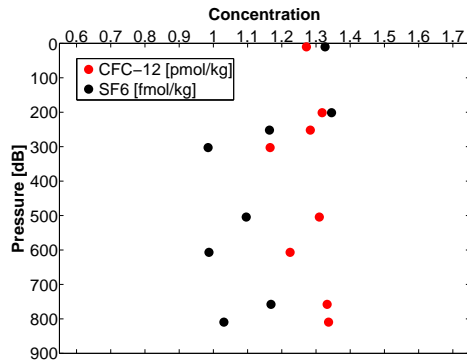
Figure 3.35. – Kasos Strait: Concentration of CFC-12 (pmol/kg) and SF$_6$ (fmol/kg) at station 289.
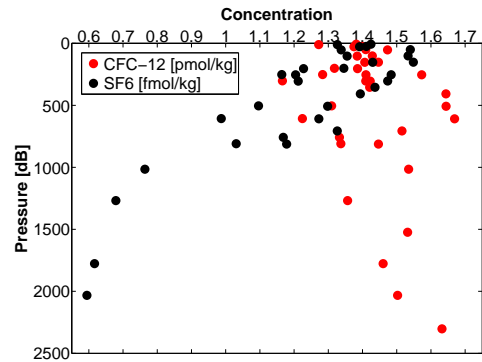
Figure 3.36. – Aegean and Cretan Sea: Concentration of CFC-12 (pmol/kg) and SF$_6$ (fmol/kg) for all three station.
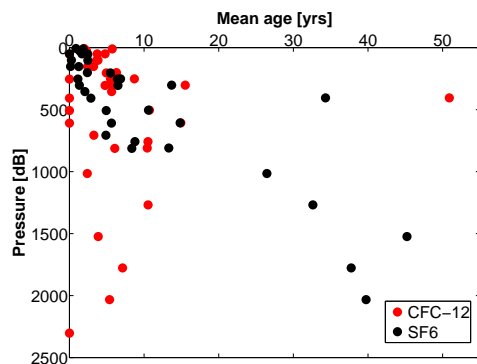
Figure 3.37. – Aegean and Cretan Sea: Mean age of CFC-12 and SF$_6$ in *yrs* for all three stations.

3.6. Western Mediterranean Sea
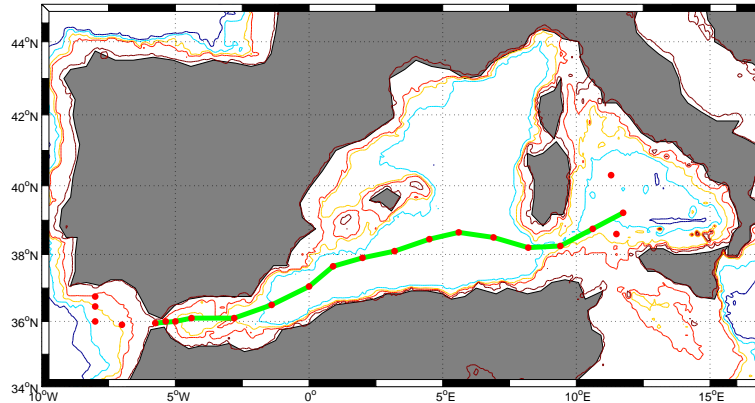
Figure 3.38. – Western Mediterranean Sea. The CFC-12 section is indicated by the green line. The depth contours are 500 m, 1000 m, 2000 m and 3000 m.

The salinity below $500\,m$ (mean age $\approx 50 - 90\,yrs$) lies between $38.42 - 38.58$ with a potential temperature range of $12.9 - 13.4\,°C$. The intermediate layer between $250 - 500\,m$ is characterized by salinites of $38.26 - 38.72$ and $\Theta = 13.2 - 14\,°C$. The densest water ($\sigma_2 \approx 37.8\,\frac{kg}{m^3}$) is indicated by a salinity of 38.48 and $\Theta = 12.9$ (Figure 3.39 and 3.40). The salinity section plot shows that the salinity is very homogeneous below $800\,m$ with a salinity value of ≈ 38.5 (Figure 3.43). A salnity maximum > 38.6 can be found at intermediate depths between $400 - 800\,m$ spreading out into the Tyrrhenian Sea. Furthermore, a salinity minimum < 36.5 can be shown at the surface layer near the Strait of Gibraltar.

From surface to $\approx 600\,m$ the concentration of CFC-12 decreases from $> 500\,ppt$ to $< 250\,ppt$ (Figure 3.41). The major part of the water column has a CFC - 12 concentration between $210 - 250\,ppt$ but with a TMZ reaching from $700 - 1300\,m$ with $\approx 200\,ppt$. This minimum core spreads out into the Tyrrhenian Sea with concentrations down to $160\,ppt$. Following the TMZ, it is the oldest layer in the water column with CFC - 12 mean ages $> 75\,yrs$. The intermediate layer gets older for the eastern part of the core, up to $115\,yrs$ in the Tyrrhenian Sea (Figure 3.42). The deep water layer below $1300\,m$ has a mean age between $60 - 75\,yrs$.
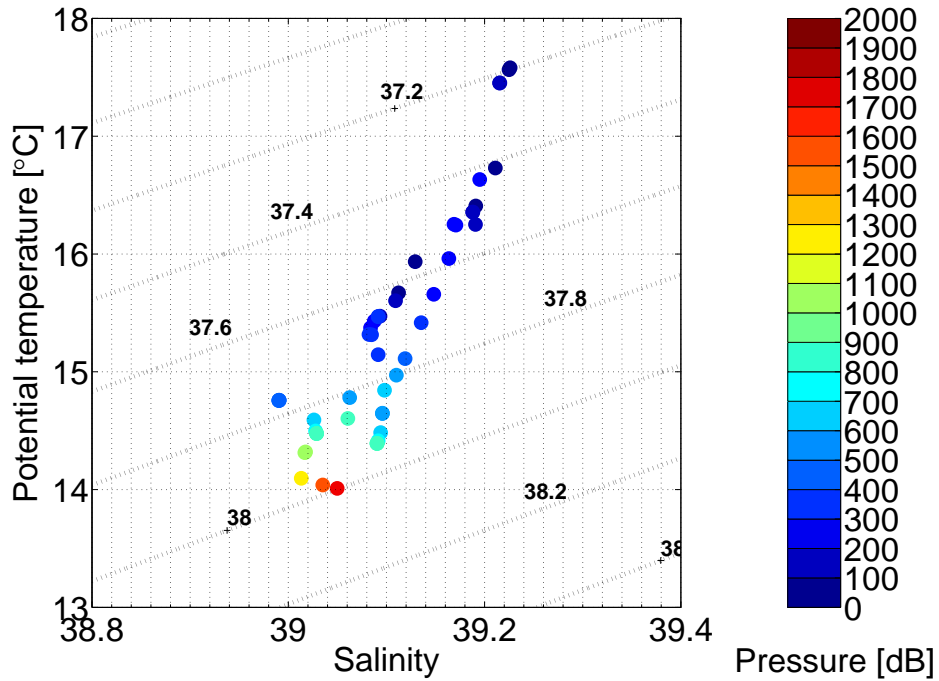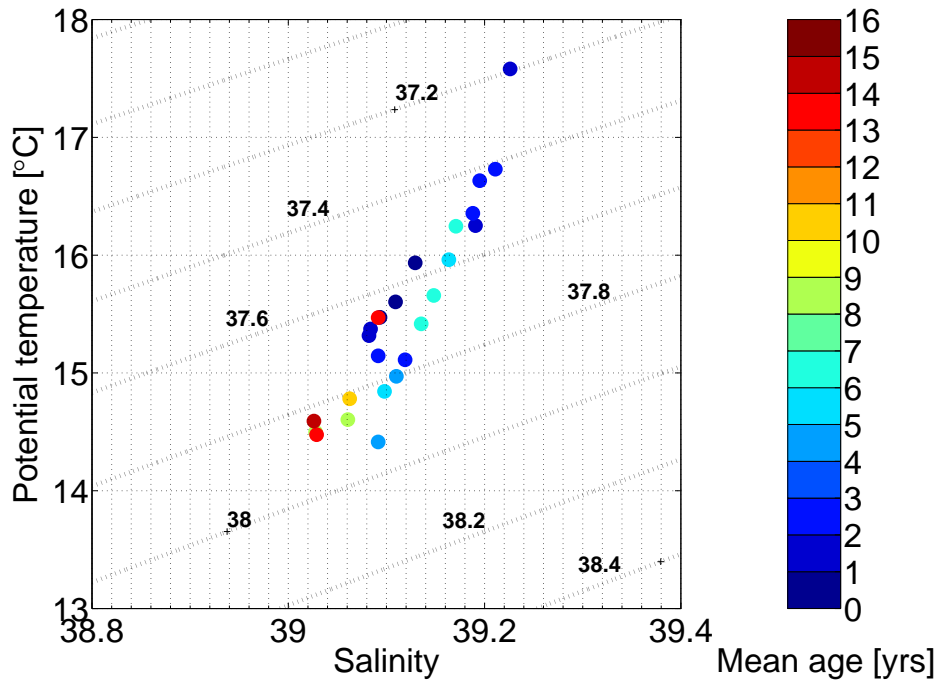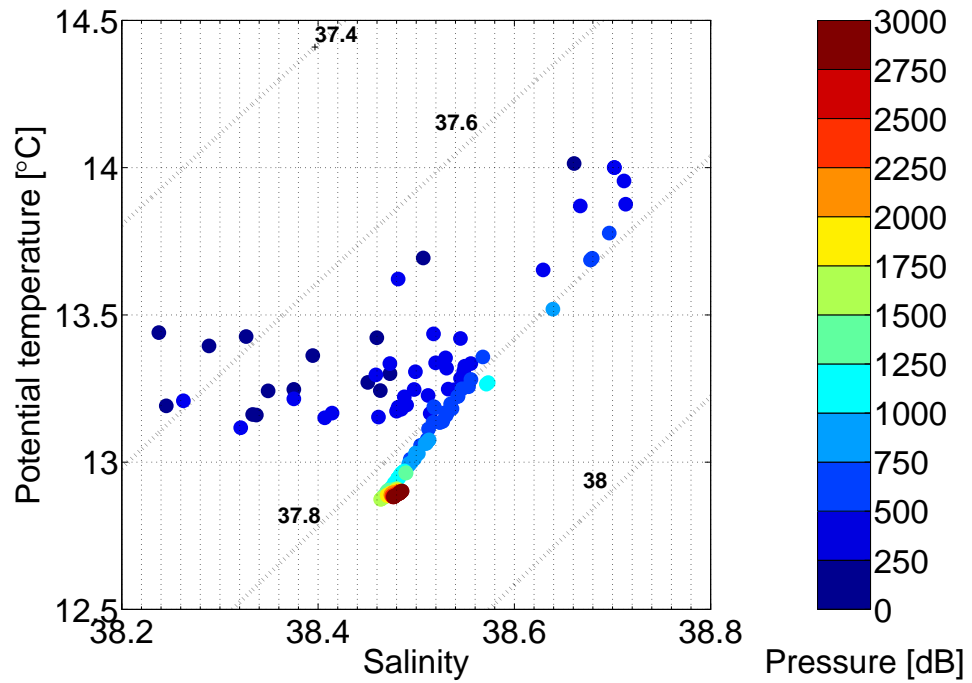
Figure 3.39. – Salinity vs. potential temperature plot of the Western Mediterranean Sea coloured by depth. The isopycnals are based on σ_2.
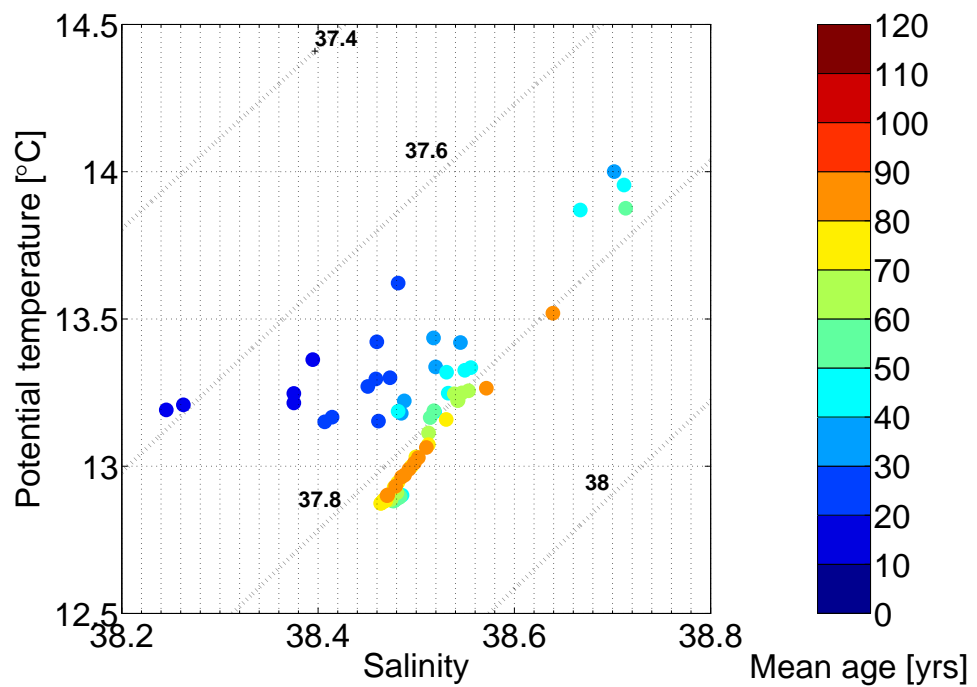

Figure 3.40. – Salinity vs. potential temperature plot of the Western Mediterranean Sea coloured by CFC-12 mean age. The isopycnals are based on σ_2.
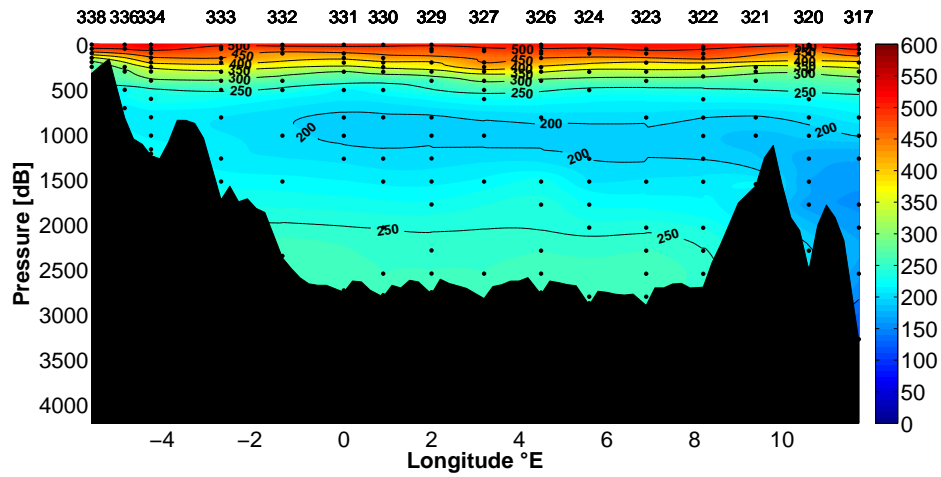
Figure 3.41. – WMed: Partial pressure of CFC-12 in *ppt*. Contour lines of 50 *ppt* and a colour contouring of 10 *ppt*.
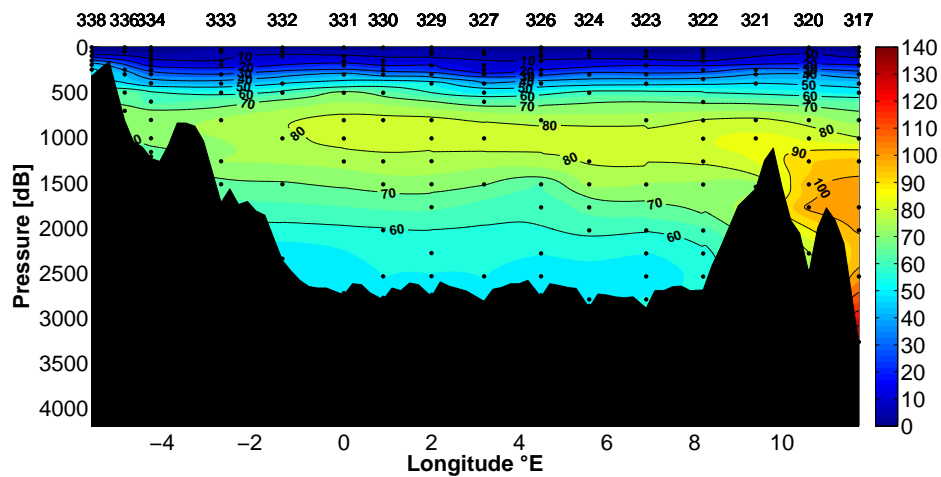
Figure 3.42. – WMed: Mean age of CFC-12 in *yrs*. Contour lines of 10 *yrs* and a colour contouring of 2 *yrs*.
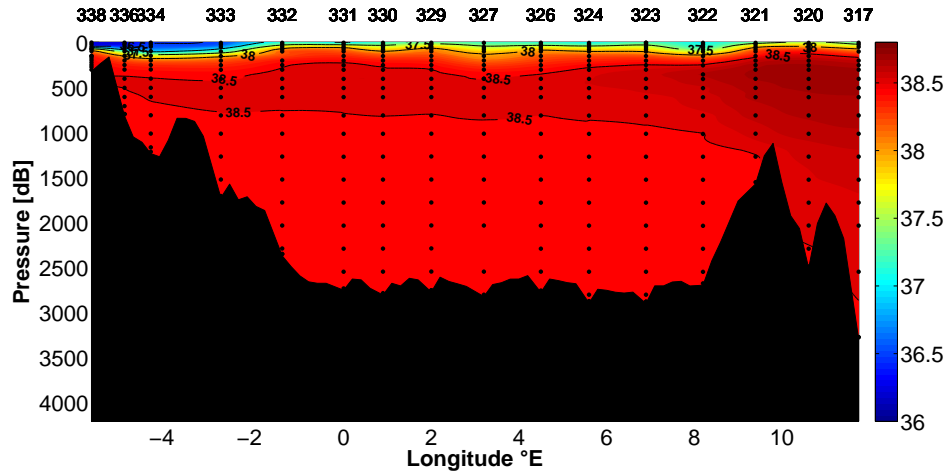
Figure 3.43. – WMed: Salinity with a contour line fragmentation of 0.5 and a colour contouring of 0.1.

3.7. Tyrrhenian Sea
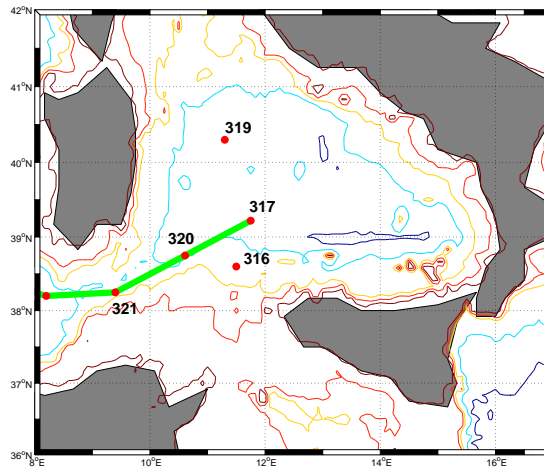
Figure 3.44. – Tyrrhenian Sea. Related stations are 316, 317, 319 and 320. The depth contours are 500 m, 1000 m, 2000 m and 3000 m.

The Salinity reaches from $38.47 - 38.70$ with a potential temperature between $12.9 - 13.8\,°C$ for depths below $500\,m$ (mean age $> 50\,yrs$). The intermediate layer between $250 - 500\,m$ is characterized by salinity values between $38.63 - 38.72$ and potential

temperatures of $13.7 - 14.1$. The densest water ($\sigma_2 \approx 37.8$) is indicated by a salinity of 38.47 and $\Theta = 12.9\,^\circ C$ (Figure 3.46 and 3.47). The stations $320 - 322$ show a clear CFC-12 concentration maximum with values $\geq 200\,ppt$, whereas station 317 shows a clear minimum $< 100\,ppt$ (Figure 3.45). Furthermore, there is a salinity minimum of 38.47 for station $320 - 322$ but for station 317 the bottom salinity only reaches 38.49. Figure 3.48 shows the characteristics of salinity vs. potential temperature for different sea areas. The Western Basin is indicated by black dots, the Strait of Sardinia is indicated by green dots and the Tyrrhenian Sea is indicated by red dots. The stations 320 and 321 have salinity and Θ properties of both sea areas.
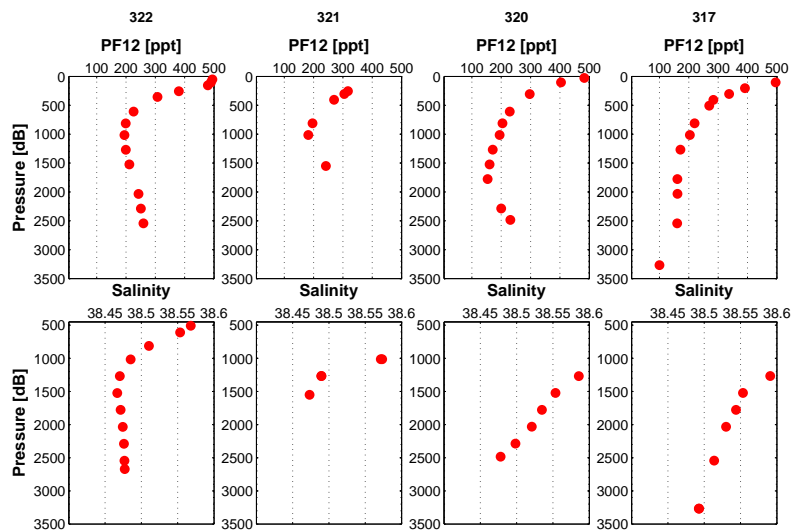
Figure 3.45. – Tyrrhenian Sea: Salinity and CFC-12 concentrations in *ppt*.
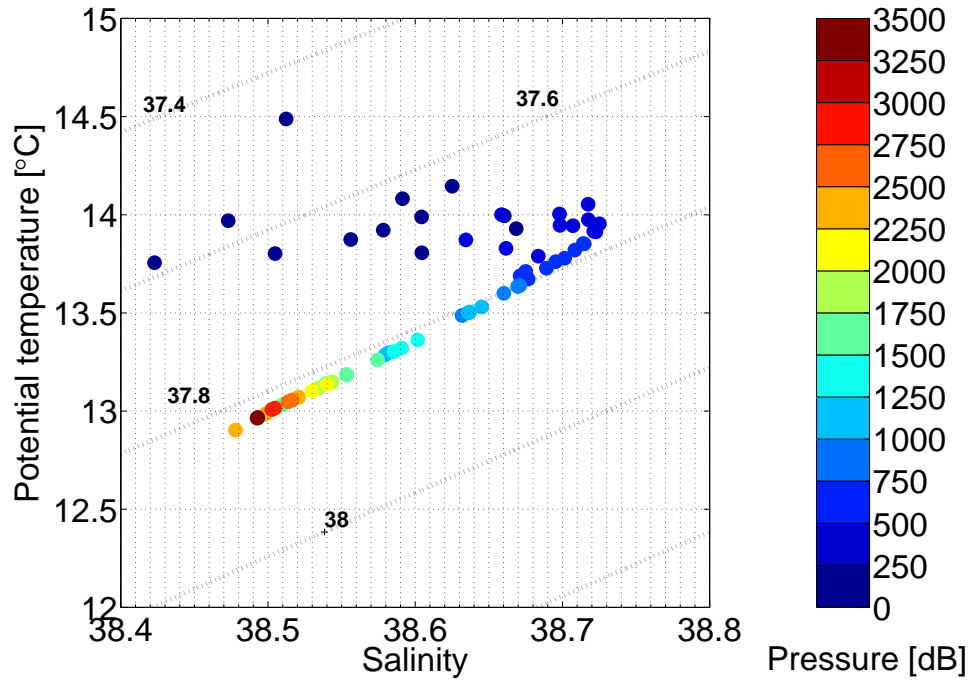
Figure 3.46. – Salinity vs. potential temperature plot of the Tyrrhenian Sea coloured by depth. The isopycnals are based on σ_2.
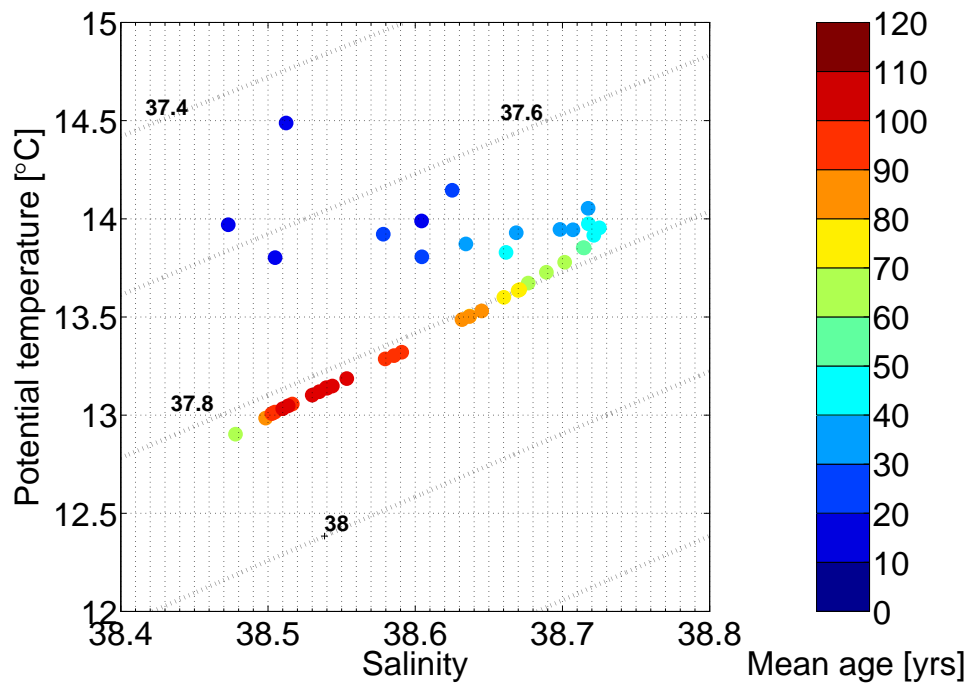
Figure 3.47. – Salinity vs. potential temperature plot of the Tyrrhenian Sea coloured by CFC-12 mean age. The isopycnals are based on σ_2.
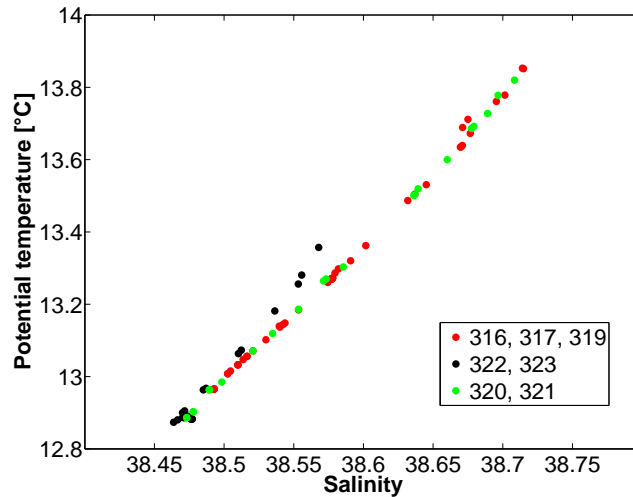
Figure 3.48. – Potential temperature vs. salinity of characteristic stations in the WMed.

3.8. Anthropogenic Carbon

3.8.1. Anthropogenic Carbon of M84
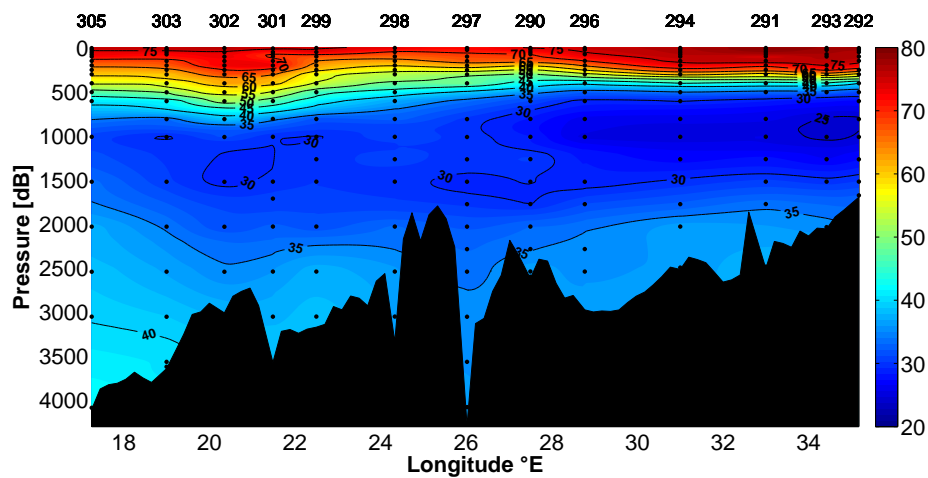
Figure 3.49. – EMed: Anthropogenic carbon in $\mu mol/kg$ based on CFC-12. Contour lines of 5 $\mu mol/kg$ and a colour contouring of 1 $\mu mol/kg$.

The anthopogenic carbon content reaches from 25 $\frac{\mu mol}{kg}$ in the TMZ of the Levantine Sea to 41 $\frac{\mu mol}{kg}$ in the bottom layer of the Western Ionian Sea (Depths below 500 −

$600\,m$). Above these deeper layers, the concentration increases with decreasing depth. Values of $40\,\frac{\mu mol}{kg}$ are found at intermediate depth and high values up to $80\,\frac{\mu mol}{kg}$ at the surface (Figure 3.49).

3.8.2. Anthropogenic Carbon in relation to 2001

The data set of the M51 cruise is taken from CARINA [2001].

Figure 3.50 and 3.51 shows that the anthropogenic carbon increased mainly in the surface and intermediate layers down to $1600\,m$ and in some parts of the deep water. A rough statistical survey is listed in table 3.2, 3.3 and 3.4. The water column is partitioned into two layer segments. The upper layer $(0-500\,m)$ has a small volumetric share of the whole water column, but is characterized by very high C_{ant} concentrations. The deeper layers $(500\,m-bottom)$ form the major volumetric share of the water column, but are characterized by low C_{ant} concentrations (Figure 3.49). Furthermore, this layer partitioning allows for seperated view of changes and trends of the C_{ant} content due to different sources. The upper layer is mainly effected by direct atmospheric input and intermediate layer formation (e.g. LIW). The C_{ant} content in deep water layers is mainly controlled by deep water formation. Table 3.4 shows that the concentration of C_{ant} has increased by $11\,\frac{\mu mol}{kg}$ in the upper layer between 2001-2011. The concentrations of the deep water layers have increased by $2\,\frac{\mu mol}{kg}$ in the Levantine Basin and by $5\,\frac{\mu mol}{kg}$ in the Ionian Basin. The mean column inventories of the M51 and M84 EMed section are listed in table 3.5. The mean column inventory of the Levantine Sea has increased $\approx 3.6\,\frac{mol}{m^2}$. The one of the Ionian Sea has increased by $29.7\,\frac{mol}{m^2}$. Figure 3.52 shows the interpolated C_{ant} concentrations for two specific stations. Station 298 belongs to the M84 cruise and station 526 to the M51 cruise. These two stations are chosen to be approximately at the same coordinates to have a direct relation of the concentration changes over the last decade. The column inventory of station 298 is $\approx 129\,\frac{mol}{m^2}$ and the one of station 526 $\approx 118\,\frac{mol}{m^2}$. Following that the C_{ant} concentration increased by about $11\,\frac{mol}{m^2}$.
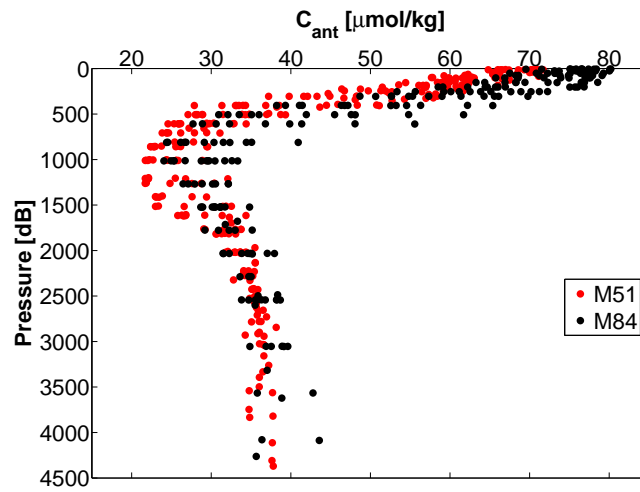
Figure 3.50. – C_{ant} concentrations in $\mu mol/kg$. The M51 data from 2001 is indicated by red dots. The M84 data from 2011 is indicated by black dots.
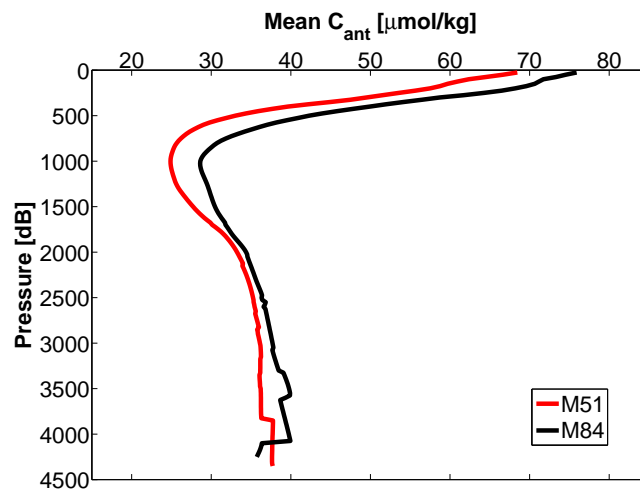
Figure 3.51. – Mean concentration of C_{ant} in $\mu mol/kg$. The M51 data from 2001 is indicated by the red curve. The M84 data from 2011 is indicated by the black curve.

Table 3.2. – EMed: Anthropogenic carbon in 2011.

Statistics	C_{ant} $[\mu mol/kg]$ $(0 - 500\,m)$	C_{ant} $[\mu mol/kg]$ $(500\,m - bottom)$
Levantine Sea		
mean value	67.65	31.23
median	71.80	31.06
std. dev.	11.92	3.86
Ionian Sea		
mean value	67.43	37.34
median	68.27	36.09
std. dev.	7.63	7.10

Table 3.3. – EMed: Anthropogenic carbon in 2001.

Statistics	C_{ant} $[\mu mol/kg]$ $(0 - 500\,m)$	C_{ant} $[\mu mol/kg]$ $(500\,m - bottom)$
Levantine Sea		
mean value	56.45	29.35
median	59.86	28.88
std. dev.	11.46	5.50
Ionian Sea		
mean value	56.71	32.30
median	58.88	33.04
std. dev.	9.72	3.53

Table 3.4. – Changes in anthropogenic carbon between $2001 - 2011$.

Statistics	ΔC_{ant} $[\mu mol/kg]$ (%) $(0 - 500\,m)$	ΔC_{ant} $[\mu mol/kg]$ (%) $(500\,m - bottom)$
Levantine Sea		
mean value	+11.2 (+19.8)	+1.88 (+6.4)
median	+11.94 (+19.9)	+2.18 (+7.5)
std. dev.	+0.46 (+4.0)	-1.64 (-29.8)
Ionian Sea		
mean value	+10.72 (+18.9)	+5.04 (+15.6)
median	+9.39 (+15.9)	+3.05 (+9.2)
std. dev.	-2.09 (-21.5)	+3.57 (+101)

Table 3.5. – Column inventories of anthropogenic carbon in 2001 and 2011.

Sea area	M84 - best ratio $[mol/m^2]$	M51 - best ratio $[mol/m^2]$	Difference $[mol/m^2]$ (%)
Levantine Sea	160.77	157.16	+3.61 (+2.3)
Ionian Sea	170.27	140.54	+29.73 (+21.2)
EMed	168.51	158	+10.51 (+6.7)
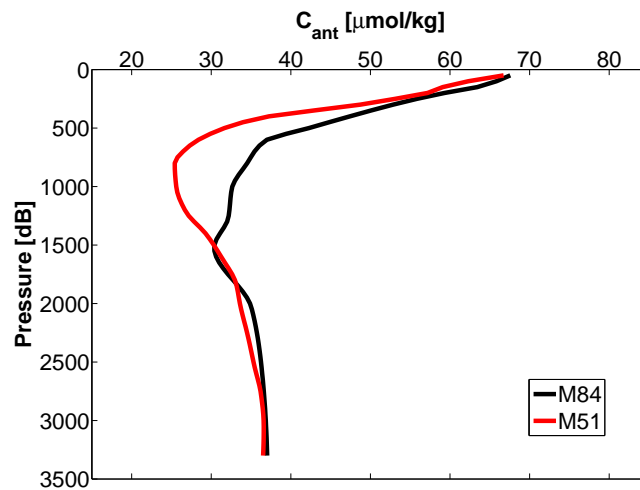
Figure 3.52. – Interpolated concentration of anthropogenic carbon in $\mu mol/kg$. Station 296 of the M84 cruise is indicated by the black curve. Station 526 of the M51 cruise is indicated by the red cruve. Both stations are chosen to have same coordinations of sampling.

3.8.3. Anthropogenic Carbon of M51 - New approach

The C_{ant} calculations of M51 have been carried out on the basis of CFC-12 data with a $^{\Delta}/_{\Gamma}$ ratio of 1.0 [Schneider et al., 2010]. Under the assumption that the determined ratios for the EMed of M84 are quite similar to the ones of M51, the C_{ant} calculations can be done more precisely.

Figure 3.53 and 3.54 describe the difference between the two ratios. The differences are quite small at the surface, but increase with depth. A statistical survey was carried out identically to the one described above (Table 3.6). The upper layer $(0-500\,m)$ is not much effected by a change in the ratio. The C_{ant} concentrations are slightly higher for the lower $^{\Delta}/_{\Gamma}$ ratios in the deep water layers. The difference of the whole EMed section below $500\,m$ is $\approx +1.6\,\frac{\mu mol}{kg}$ as well as $\approx +1.2\,\frac{\mu mol}{kg}$ for the Ionian Sea and $\approx +1.9\,\frac{\mu mol}{kg}$ for the Levantine Sea. Table 3.7 shows similar calculations for the mean column inventories. The differences between the two ratios are $\approx +6.6\,\frac{mol}{m^2}$ for the whole EMed, $\approx +4\,\frac{mol}{m^2}$ for the Ionian Sea and $\approx +7.7\,\frac{mol}{m^2}$ for the Levantine Sea. For one specific station (e.g. station 526) ratio 1.0 yields $\approx 115.00\,\frac{mol}{m^2}$ and the best fitting ratio $\approx 118.52\,\frac{mol}{m^2}$. Hence the difference is $+3.52\,\frac{mol}{m^2}$ (Figure 3.55).

Figure 3.56 and 3.57 visualize the difference of both ratio approaches and where the main changes occur. The water layers above $500\,m$ are not shown due to their relatively small changes in the concentration.
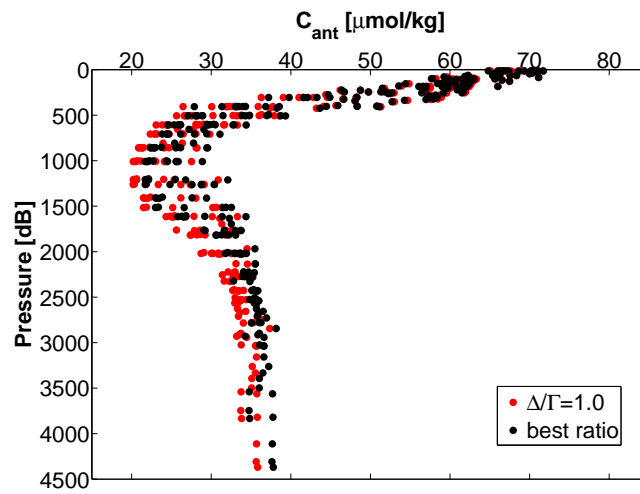
Figure 3.53. – C_{ant} concentrations for different $^\Delta/_\Gamma$ ratios in $\mu mol/kg$. The red dots indicate a $^\Delta/_\Gamma$ ratio of 1.0. The black dots indicate the best fitting ratios determined by the M84 data set.
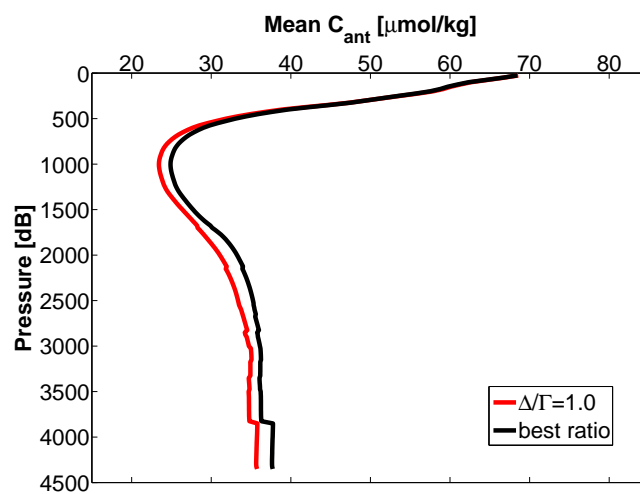
Figure 3.54. – Mean concentrations of C_{ant} for different $^\Delta/_\Gamma$ ratios in $\mu mol/kg$. The red curve indicates a $^\Delta/_\Gamma$ ratio of 1.0. The black curve indicates the best fitting ratios determined by the M84 data set.

Table 3.6. – Differences between $^{\Delta}/_{\Gamma}$=1.0 and best fitting ratio.

Statistics	ΔC_{ant} $[\mu mol/kg]$ $(0-500\,m)$	ΔC_{ant} $[\mu mol/kg]$ $(0-500\,m)$
EMed		
mean value	-0.05	+1.61
median	-0.23	+1.46
std. dev.	+0.47	+0.60
Ionian Sea		
mean value	-0.10	+1.18
median	-0.28	+1.16
std. dev.	+0.42	+0.18
Levantine Sea		
mean value	-0.01	+1.92
median	-0.16	+1.51
std. dev.	+0.50	+0.60

Table 3.7. – Column inventories of anthropogenic carbon for different ratios.

Sea area	Best ratio $[mol/m^2]$	$^{\Delta}/_{\Gamma} = 1.0$ $[mol/m^2]$	Difference $[mol/m^2]$ (%)
Levantine Sea	157.16	149.46	+7.70 (+5.2)
Ionian Sea	140.54	136.57	+3.97 (+2.9)
EMed	158.00	151.37	+6.63 (+4.4)
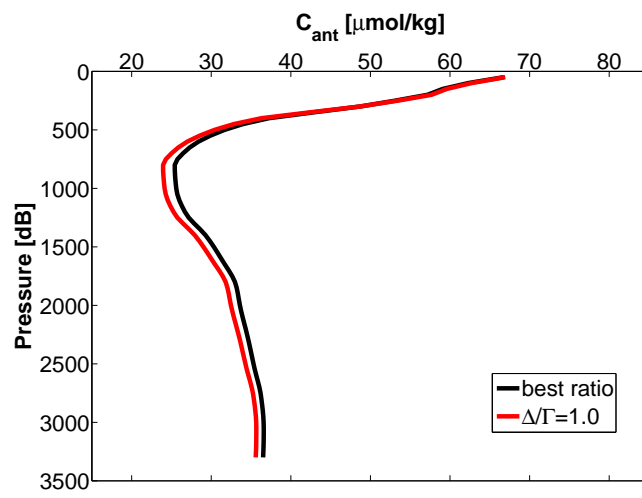
Figure 3.55. – Column inventories of station 526 for different $\Delta/_\Gamma$ ratios. The red curve indicates a ratio of 1.0. The black curve indicates the best fitting ratio.
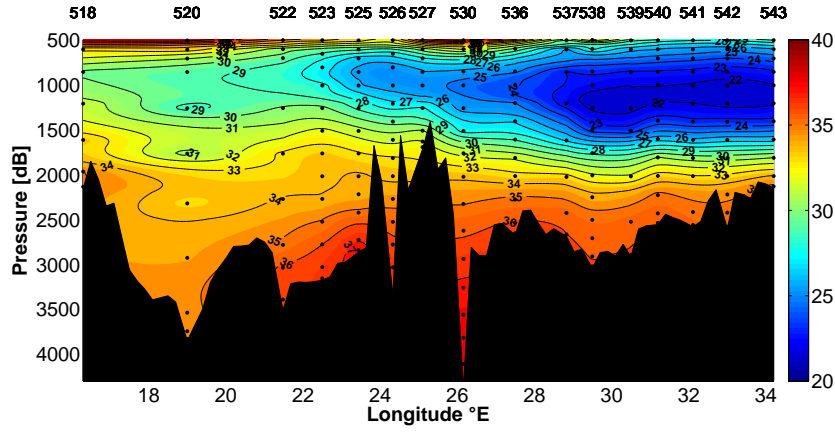
Figure 3.56. – EMed: Anthropogenic carbon in $\mu mol/kg$ for best ratio below $500\,m$. Contour line fragmentation of $1\,\mu mol/kg$ and a colour contouring of $0.5 \mu mol/kg$.
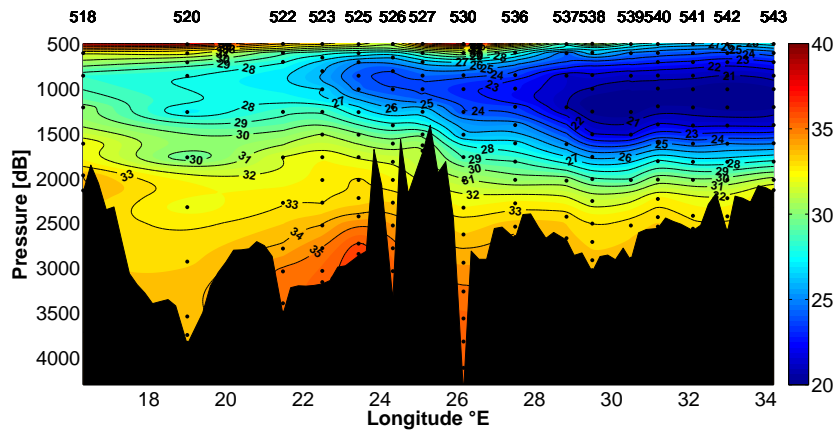
Figure 3.57. – EMed: Anthropogenic carbon in $\mu mol/kg$ for $^{\Delta}/_{\Gamma} = 1.0$ below $500\,m$. Contour line fragmentation of $1\,\mu mol/kg$ and a colour contouring of $0.5 \mu mol/kg$.

4. Discussion

4.1. Transit Time Distribution

The mean age vs mean age plots (Appendix C) show that the Western Mediterranean cannot be described by the used tracer couple or the 1D-TTD model. The reasons might be that for each part of the WMed (Alboran Sea, Western Basin, Tyrrenhian Sea) only one station with both tracer exists. Such a small data set does not allow a well founded statement about whether the tracer couple is useless or even more the 1D-TTD-model. It remains to be seen, which results can be determined by the other obtained tracers (e.g. ^{3}He, ^{3}H, ^{14}C, etc). Furthermore, the 2IG-TTD model should be applied to the data set.

The CFC-12 concentrations were scattering at high values throughout the whole water column at some stations. These stations mainly have been sea areas at overflows or well mixed basins (e.g. Aegean Sea, Kasos Strait). The combination of a clear SF_6 profile and such a scattering CFC-12 profile at these stations does not give any significant TTD results. Very young water masses (tracer age $< 18\,yrs$) are hardly to describe with the CFC-12 tracer due to its decreasing concentration in the atmosphere. The SF_6 loses the significance for tracer ages $> 55\,yrs$ due to the low concentration for these ages.

Statistical calculations without any specific restrictions to the model are leading to wrong results. Figure 3.1 shows the results only obtained by defining the ratios for which the mean ages difference has a minimum. This suggests that most of the determined data was very close or perfectly matching to a specific ratio. Based on

these results one would define quite higher ratios at the surface and a very low ratio at intermediate depth. It follows, that the calculated mean age sections of both tracer are notably different and thus useless. By using the exact model restrictions, less specific data points (Figure 3.2) with a defined ratio can be obtained (only exact matching). However, the mean age plots of both tracer are quite similar based on these results (Figure 3.10 and 3.11). The mean ages are thereby sufficiently determined.

4.2. Eastern Mediterranean Sea

To describe the recent changes of the EMed, the complete data set of a quite similar section of Meteor cruise M51-2 is presented in the appendix D. The M51 cruise was carried out in the year 2001. In relation to the data set of M84 in 2011, the recent changes of the last decade can be described. All interpolation parameters for the gridding of the section plots were kept identically. This provides a better relation between the data set of M51 and the one of M84. The obtained best fitting TTD ratios were also applied to the data set of M51. It is noteworthy, that this is only an approach to the real ratios of M51 with the assumption that the TTD characteristics have not changed over the last ten years. Even if the ratios do not match perfectly, serveral large and short scale trends as well as changes can be described.

The TMZ in the eastern part of the Levantine Sea spreaded out vertically and westwards in the last ten years. The TMZ of 2001 can be roughly described by the contour line of $60\,yrs$ and thus for 2011 (present state) by CFC-12 tracer mean ages $> 70\,yrs$. In 2001 the TMZ was vertically located between $\approx 600 - 1600\,m$ depth (Figure D.8) and the thickness of this layer decreased from east to west. Finally the TMZ ends in the western Ionian Sea. In 2011 the TMZ reaches from $\approx 500\,m$ to $1700\,m$ in the Levantine Sea (Figure 3.10). Furthermore, mean ages describing the TMZ can be found throughout the whole west-east section of the EMed at depth between $500 - 1700\,m$ with a dip down to $2100\,m$ in the Ionian Sea (Figure 3.10,

station 302). There is a slight maximum in mean ages ($> 80\,yrs$) above this dip at $\approx 1250\,m$ depth. This dip is better shown at the north south section from the Southern Adriatic Sea into the Ionian Basin (Figure 3.18, station 302). The newly formed EMDW from ASOW [Hainbucher et al., 2006, Robino and Hainbucher, 2007] is shown by higher CFC-12 concentrations ($> 230\,ppt$) at the bottom layer in the western part of the Ionian Basin. Additionally, the salinity and potential temperature characteristics of the ASOW ($S = 38.74$, $\Theta = 13.4\,^{\circ}C$) can be found in the Southern Adriatic Sea and in the bottom layer (EMDW) of the northern and southern Ionian Sea (Figure 3.22, 3.14 and 3.6). The T/S[1] plots coloured by mean age show clearly that the densest bottom water with ASOW characteristics is relatively young with mean ages $\leq 50\,yrs$ (Figure 3.15 and 3.7). Neither overflow water characteristics of the Adriatic nor the Aegean Sea can be observed in the Levantine Sea. It follows that the EMDW of the Levantine Sea is not affected by any new deep water formation. The CFC - 12 concentrations are still between $\approx 190 - 210\,ppt$. Figure 3.12 and 3.20 describe a very homogeneous salinity of the water column below $500\,m$. The Aegean Sea has relativeley high salinity values of > 39 and thus one would expect a significant increase in salinity for a dense water outflow from the Aegean Sea. The concentration distribution of CFC-12, the determined mean ages and the T/S characteristics of the EMed currently exclud the Aegean Sea as a deep water source for the EMDW. Small scale dense water interdependencies at intermediate depth between the Aegean (Cretan) Sea, the Levantine Sea and the Ionian Sea (e.g. LIW, CIW) are not analized yet.

4.3. Southern Adriatic Sea

Even if there is only one station in the Southern Adriatic Sea where tracer data was obtained, it is a very interesting station. The ratio determination is based on five data points which are barely in the scope of the TTD-Model (Figure 3.2, station

---

[1]T/S stands for Temperature and Salinity. The temperature is always referred as the potential temperature.

313). The upper water column is dominated by a high $^{\Delta}/_{\Gamma}$ ratio of 1.2 with a high CFC-12 content of $430 - 540\,ppt$ (Figure C.4). It follows that these watermasses are young and formed by a high mixing ratio and diffusivity, respectively. The Adriatic Sea is mainly supported by water layers between $0 - 500\,m$. These are normally represented by the LIW and MAW coming from the Ionian Sea [Roether et al., 2007]. The bottom layer is characterized by a very low $^{\Delta}/_{\Gamma}$ ratio of 0.4 indicating a high advective share. This dense water is very young (mean age $< 10\,yrs$) and has different T/S characteristics than the ASOW. The salinity is 38.73 and the potential temperature $13.1\,°C$. This water mass might be formed by a smaller deep water formation in the Southern Adriatic Sea. It does not reach the shallow sill of Otranto and is thus retained in the Adriatic Basin. The T/S characteristics of the recent ASOW are still verifiable at intermediate depth between $700 - 900\,m$.

4.4. Aegean and Cretan Sea

The CFC-12 concentrations are all $> 1.15\,\frac{pmol}{kg}$ ($> 400\,ppt$), whereas the SF$_6$ reaches from 0.6 to $1.42\,\frac{fmol}{kg}$ ($2.4 - 7.2\,ppt$). However, the CFC-12 has no concentration gradient such as the SF$_6$ (Figure 3.36). The CFC-12 values are scattering from surface to bottom and thus there is no useable TTD relation between the two tracers. The scattering of the high CFC-12 concentrations shows clearly that this tracer loses its significance for young water masses. Nevertheless, this scattering and the young tracer ages indicate that the Aegean and Cretan Sea are well mixed throughout the whole water column.

4.5. Western Mediterranean Sea

The newly formed deep water between $2004 - 2006$ [Schroeder et al., 2008a, 2010] is shown by the high CFC-12 concentrations below $\approx 1300\,m$ with its maximum values ($> 250\,ppt$) at the bottom layer (Figure 3.41). The WMDW is characterized

by a salinity of 38.48, $\Theta < 12.9\,°C$ and mean ages $< 75\,yrs$ (Figure 3.39, 3.40 and 3.42). The exact spreading of this deep water layer cannot be obtained by CFC-12 and salinity due to the relatively homogeneous characteristics of both parameters throughout the whole Western Basin and Alboran Sea (Figure 3.41 and 3.43). A detailed analysis of the T/S properties of each single station would lead to more exact results of the deep water spreading. Nevertheless, a significant statement about the intrusion of the deep water into the Tyrrhenian Sea can be obtained. Figure 3.47, 3.45 and 3.48 show clearly that water masses with characteristics of WMDW enter the Tyrrhenian Sea over the shallow sill between Sicily and Sardinia. The WMDW is less saltier but colder ($S = 38.48\,/\,\Theta \approx 12.88$) than the bottom water of the Tyrrhenian Sea ($S = 38.52\,/\,\Theta = 13.0$). The WMDW dense water mass reaches half way down into the abyss of the Tyrrhenian Sea. The bottom layer of the Tyrrhenian Sea is not affected yet (Figure 3.45 and 3.48, station 317). However, it is expected that the entering deep water flows along the slope of Sicily (eastwards) such as the LIW and TDW. In this case the entering WMDW might reach the bottom layer in the north east of the Tyrrhenian Basin. Further transient tracer observations in this area would give a more detailed view on this topic.

The CFC-12 mean ages of the WMed are just a rough estimate, based on a $^{\Delta}/_{\Gamma} = 1.0$ for the whole western area. Nevertheless, one can say that the water masses in the Western Basin underly more mixing processes by trend than in the Tyrrhenian Sea. The water gets older from surface to bottom in the Tyrrhenian Basin what implies that there is less intrusion of younger waters into intermediate or deep water layers.

4.6. Anthropogenic carbon based on the TTD

The carbon cycle and respectively the carbon system of the Mediterranean Sea are not part of this diploma thesis. The calculations of C_{ant} on the basis of the constrained TTD should give some more aspects about the TTD characteristics and the

use of the observed results. As mentioned in the results part, all statistical surveys are based on very rough assumptions to have a first superficial view into the results. A detailed analysis of this data, containing calculations and estimations about the complete C_{ant} inventories of the Mediterranean Sea, will be the focus of further work.

In the last ten years the C_{ant} concentration has increased by about $11 \frac{\mu mol}{kg}$ at depths between $0-500\,m$. The deep water layer of the Levantine Basin was more or less unaffected by bigger changes (Table 3.4). The higher values of the Ionian Basin ($\approx +5 \frac{\mu mol}{kg}$) can be related to the dense water input from the Adriatic Sea, which transports younger waters with a higher C_{ant} content into the bottom layer. Similar tendencies can be obtained for the mean column inventories (Table 3.5). The column inventory of the Ionian Sea ($+30 \frac{mol}{m^2}$) has increased about eight times more than the one of the Levantine Sea ($+3.6 \frac{mol}{m^2}$). For a massive dense water input such as the past EMT, one would expect a bigger change in the mean concentration and column inventories. The section plot of the EMed (Figure 3.49) in contrast shows clearly that there is no bigger change in the last decade.

The defined $^\Delta/_\Gamma$ ratios of the EMed, based on the constrained TTD, are lower than the one used by Schneider et al. [2010]. The determined $^\Delta/_\Gamma$ ratios of M84 are between $0.6-0.8$, whereas Schneider et al. [2010] defined an overall ratio of $^\Delta/_\Gamma = 1.0$ for the M51 data. It follows, that the C_{ant} column inventories are underestimated because of a too high $^\Delta/_\Gamma$ ratio, provided that there was no bigger change in the ratios between $2001-2011$. Figure 3.53 and 3.54 as well as table 3.6 and 3.7 show clearly the difference between both ratios. For example the column inventory of station 526 is $115.00 \frac{mol}{m^2}$ for a ratio of 1.0. The best fitting ratio yields a column inventory of $118.52 \frac{mol}{m^2}$ and thus a difference of $+3.52 \frac{mol}{m^2}$ (Figure 3.55). The column inventory differences of both ratios yield a mean underestimation of $4.4\,\%$ for the whole EMed. Figure 3.56 and 3.57 visualize the difference of both ratios for depths below $500\,m$.

Table 3.6 includes some fundamental characteristics of the TTD-model. First of all one would not expect that there are negative values for the difference of C_{ant} ($^\Delta/_\Gamma =$

$0.8 \, or \, 0.6) - C_{ant} \, (^{\Delta}/_{\Gamma} = 1.0)$. These negative values occur only at the surface layer, where high tracer concentrations are present. High tracer concentrations represent young tracer ages. Figure 2.12 can explain this negative behaviour. The differences in mean age as well as C_{ant} concentrations are very low for young water masses and in the range of low ages each curve has intersections with the other curves. This means that in an age range of $0 - intersection$, a higher ratio leads to lower mean ages and higher C_{ant} concentrations, than a lower one. The classical behaviour is true for all ages $> intersection$.

5. Conclusion

It is very important to have a close look at the tracer couple properties and the resulting restrictions to define the exact matching $^\Delta/_\Gamma$ ratios. The relation between all mean ages of both tracers for different ratios can only be used as a preestimation. Nevertheless, with this preestimation one can check if the data aligns with the TTD-model or not (e.g. EMed and WMed). Most of the EMed can be described by the 1D-TTD model with CFC-12 and SF_6 as tracer couple. This constrained TTD data forms the basis for further estimations and calculations of column inventories of anthropogenic carbon. Additional data of other transient tracers should be considered to verify the results.

The EMed is returning to a pre EMT state. The Southern Adriatic Sea plays the major role as a deep water source for the EMDW at present state. The intermediate layer, including the TMZ, spreads out horizontally and vertically again since it has been uplifted by the massive dense water input of the EMT. But it might be just a question of time when the Aegean Sea will take over again as the major deep water source. The data cannot described the WMed in sufficient detail, making an exact determination of the TTD-model impossible. The newly formed WMDW and an overflow of this deep water into the Tyrrhenian Sea can be observed. Additional tracer data might lead to more precise information about the WMed. The whole Mediterranen Sea consists of serveral very complex processes whos mechanisms are still unknown to some extend. The transient tracers CFC-12 and SF_6 are very useful to find and characterize mixing processes and water mass properties. However, they cannot explain the precise mechanisms of the underlying processes.

6. Bibliography

P. Brasseur, J.M. Beckers, J.M. Brankart, and R. Schoenauen. Seasonal temperature and salinity fields in the mediterranean sea: Climatological analyses of a historical data set. *Deep Sea Research Part I: Oceanographic Research Papers*, 43(2):159 – 192, 1996.

J. L. Bullister and D.P. Wisegarver. The shipboard analysis of trace levels of sulfur hexafluoride, chlorofluorocarbon-11 and chlorofluorocarbon-12 in seawater. *Deep Sea Research Part I: Oceanographic Research Papers*, 55(8):1063 – 1074, 2008.

J.L. Bullister and B. Lee. Chlorofluorocarbon-11 removal in anoxic marine waters. *Geophysical Research Letters*, 22(14):1893–1896, 1995.

J.L. Bullister and R.F. Weiss. Determination of ccl3f and ccl2f2 in seawater and air. *Deep Sea Research Part A. Oceanographic Research Papers*, 35(5):839 – 853, 1988.

J.L. Bullister, D.P. Wisegarver, and F.A. Menzia. The solubility of sulfur hexafluoride in water and seawater. *Deep Sea Research Part I: Oceanographic Research Papers*, 49(1):175 – 187, 2002.

CARINA. Data set of m51-2. In *Carbon in Atlantic Ocean database*. W. Roether and A. Schneider, 2001. 06MT20011018.

G. Civitarese, M. Gacic, M. Lipizer, and G.L. Eusebi Borzelli. On the impact of the bimodal oscillating system (bios) on the biogeochemistry and biology of the adriatic and ionian seas (eastern mediterranean). *Biogeosciences*, 7(12):3987 – 3997, 2010.

Claude and Millot. Circulation in the western mediterranean sea. *Journal of Marine Systems*, 20(1-4):423 – 442, 1999.

S.C. Doney and J.L. Bullister. A chlorofluorocarbon section in the eastern north atlantic. *Deep Sea Research Part A. Oceanographic Research Papers*, 39(11-12): 1857 – 1883, 1992.

P. Forster. Changes in atmospheric constituents and radiative forcing. In *Climate Change 2007: The Physical Science Basis. Contribution of Working Group I to the Fourth Assessment Report of the Intergovernmental Panel on Climate Change*. S. Solomon and D. Qin and M. Manning and Z. Chen and M. Marquis and K.B. Averyt and H. Miller, Cambridge University Press, Cambridge, United Kingdom and New York, NY, USA, 2007.

D. Hainbucher, A. Robino, and B. Klein. Water mass characteristics in the deep layers of the western ionian basin observed during may 2003. *Geophysical Research Letters*, 33(L05608), 2006.

T.M. Hall and R.A. Plumb. Age as a diagnostic of stratospheric transport. *Journal of Geophysical Research*, 99(D1):1059–1070, 1994.

B. Klein, W. Roether, B.B. Manca, D. Bregant, V. Beitzel, V. Kovacevic, and A. Luchetta. The large deep water transient in the eastern mediterranean. *Deep Sea Research Part I: Oceanographic Research Papers*, 46(3):371 – 414, 1999.

B. Klein, W. Roether, G. Civitarese, M. Gacic, B.B. Manca, and M.R. d'Alcala. Is the adriatic returning to dominate the production of eastern mediterranean deep water? *Geophysical Research Letters*, 27(20):3377 – 3380, 2000.

A. Lascaratos, W. Roether, K. Nittis, and B. Klein. Recent changes in deep water formation and spreading in the eastern mediterranean sea: a review. *Progress In Oceanography*, 44(1-3):5 – 36, 1999.

C.S. Law, A.J. Watson, and M.I. Liddicoat. Automated vacuum analysis of sulphur hexafluoride in seawater: derivation of the atmospheric trend (1970-1993) and potential as a transient tracer. *Marine Chemistry*, 48(1):57 – 69, 1994.

P. Malanotte-Rizzoli and A. Hecht. Large scale properties of the eastern mediterranean: a review. *Oceanologica Acta*, 11(4):323 – 335, 1988.

P. Malanotte-Rizzoli and A. Robinson. Poem: Physical oceanography of the eastern miditerranean. *EOS Transactions*, 69:194 – 203, 1988.

P. Malanotte-Rizzoli, A.R. Robinson, W. Roether, B. Manca, A. Bergamasco, S. Brenner, G. Civitarese, D. Georgopoulos, P.J. Haley, S. Kioroglou, H. Kontoyannis, N. Kress, M.A. Latif, W.G. Leslie, E. Ozsoy, M.R. d'Alcala, I. Salihoglu, E. Sansone, and A. Theocharis. Experiment in eastern mediterranean probes origin of deep water masses. *EOS Transactions*, 77:305 – 311, 1996.

S. Marullo, R. Santoleri, and F. Bignami. The surface characteristics of the tyrrhenian sea: Historical satellite data analysis. In *Seasonal and interannual variability of the western Mediterranean Sea*, pages 135 – 154. P.E. La Violette, 1995.

A. Robino and D. Hainbucher. A large abrupt change in the abyssal water masses of the eastern mediterranean. *Geophysical Research Letters*, 34(L23607), 2007.

A.R. Robinson, P. Malanotte-Rizzoli, A. Hecht, A. Michelato, W. Roether, A. Theocharis, U. Uenlueata, N. Pinardi, A. Artegiani, A. Bergamasco, J. Bishop, S. Brenner, S. Christianidis, M. Gacic, D. Georgopoulos, M. Golnaraghi, M. Hausmann, H.-G. Junghaus, A. Lascaratos, M.A. Latif, W.G. Leslie, C.J. Lozano, T. Oguz, E. Oezsoy, E. Papageorgiou, E. Paschini, Z. Rozentroub, E. Sansone, P. Scarazzato, R. Schlitzer, G.-C. Spezie, E. Tziperman, G. Zodiatis, L. Athanassiadou, M. Gerges, and M. Osman. General circulation of the eastern mediterranean. *Earth-Science Reviews*, 32(4):285 – 309, 1992.

W. Roether and R. Schlitzer. Eastern mediterranean deep water renewal on the basis

of chlorofluoromethane and tritium data. *Dynamics of Atmospheres and Oceans*, 15(3-5):333 – 354, 1991.

W. Roether, B.B. Manca, B. Klein, D. Bregant, D. Georgopoulos, V. Beitzel, V. Kovacevic, and A. Luchetta. Recent changes in eastern mediterranean deep waters. *Science*, 271(5247):333 – 335, 1996.

W. Roether, B. Klein, B.B. Manca, A. Theocharis, and S. Kioroglou. Transient eastern mediterranean deep waters in response to the massive dense-water output of the aegean sea in the 1990s. *Progress In Oceanography*, 74(4):540 – 571, 2007.

R. Schlitzer, W. Roether, H. Oster, H.G. Junghans, M. Hausmann, H.Johannsen, and A. Michelato. Chlorofluoromethane and oxygen in the eastern mediterranean. *Deep Sea Research Part A. Oceanographic Research Papers*, 38(12):1531 – 1551, 1991.

A. Schneider, T. Tanhua, A. Koertzinger, and D.W.R. Wallace. High anthropogenic carbon content in the eastern mediterranean. *Journal of Geophysical Research*, 115(C12050), 2010.

F. Schott, M. Visbeck, and U. Send. Open ocean deep convection, mediterranean and greenland seas. In *Ocean Processes in Climate Dynamics: Global and Mediterranean Examples*, pages 203 – 225. P. Malanotte-Rizzoli and A. Robinson, 1994.

K. Schroeder, A. Ribotti, M. Borghini, R. Sorgente, A. Perilli, and G.P. Gasparini. An extensive western mediterranean deep water renewal between 2004 and 2006. *Geophysical Research Letters*, 35(L18605), 2008a.

K. Schroeder, S.A. Josey, M. Herrmann, L. Grignon, G.P. Gasparini, and H.L. Bryden. Abrupt warming and salting of the western mediterranean deep water after 2005: Atmospheric forcings and lateral advection. *Journal of Geophysical Research*, 115(C08029), 2010.

T. Tanhua, D.W. Waugh, and D.W.R. Wallace. Use of sf6 to estimate anthropogenic co2 in the upper ocean. *Journal of Geophysical Research*, 113(C04037), 2008.

A. Theocharis, B. Klein, K. Nittis, and W. Roether. Evolution and status of the eastern mediterranean transient (1997 - 1999). *Journal of Marine Systems*, 33-34 (0):91 – 116, 2002.

M.J. Warner and R.F. Weiss. Solubilities of chlorofluorocarbons 11 and 12 in water and seawater. *Deep Sea Research Part A. Oceanographic Research Papers*, 32(12): 1485 – 1497, 1985.

D.W. Waugh, T.M. Hall, and T.W.N. Haine. Relationship among tracer ages. *Journal of Geophysical Research*, 108(C5):3138, 2003.

G. Wuest. On the vertical circulation of the mediterranean sea. *Journal of Geophysical Research*, 66(10):3261 – 3271, 1961.

A. Flow schemes
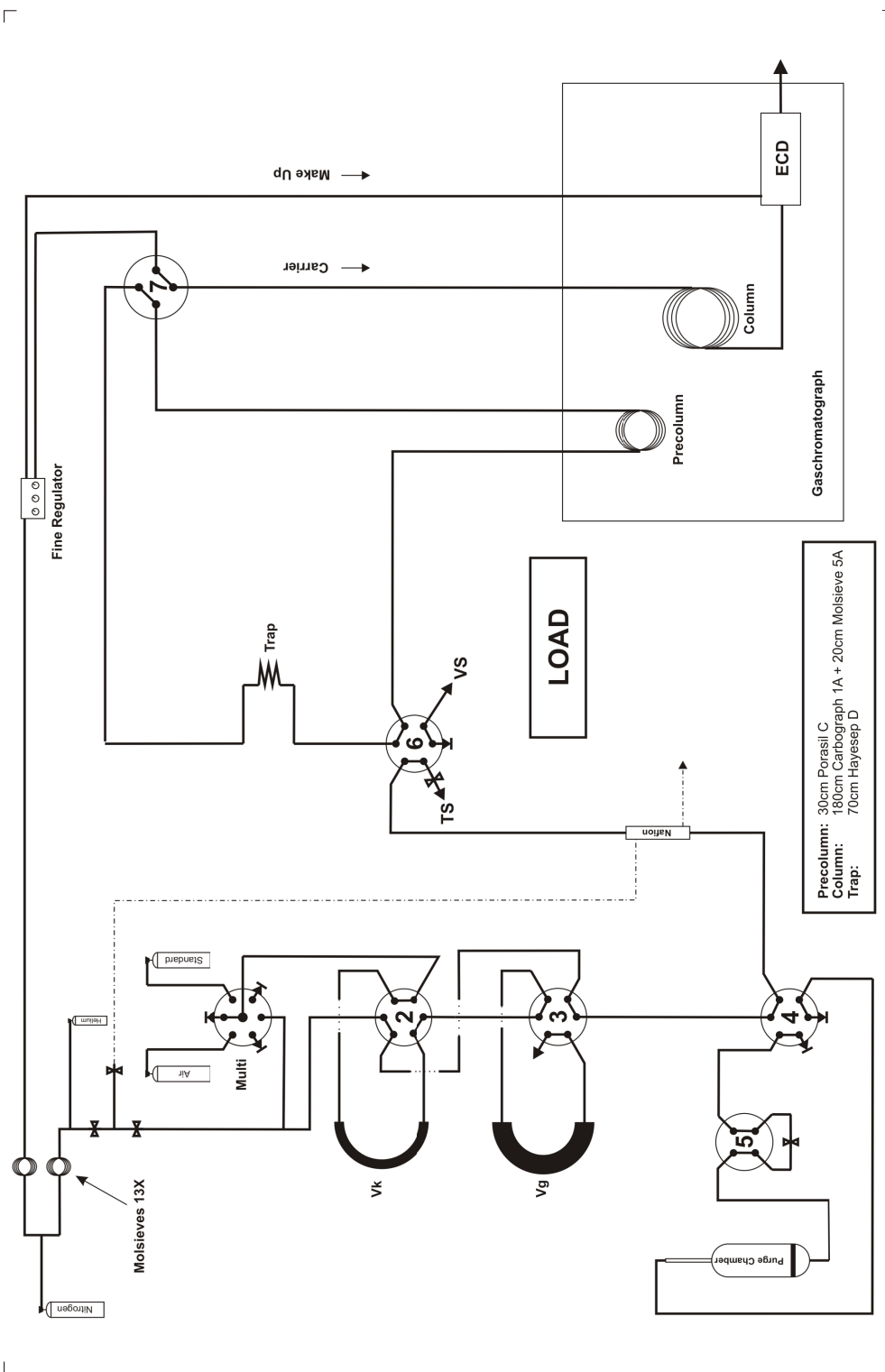
Figure A.1. – VS1-system during M84.
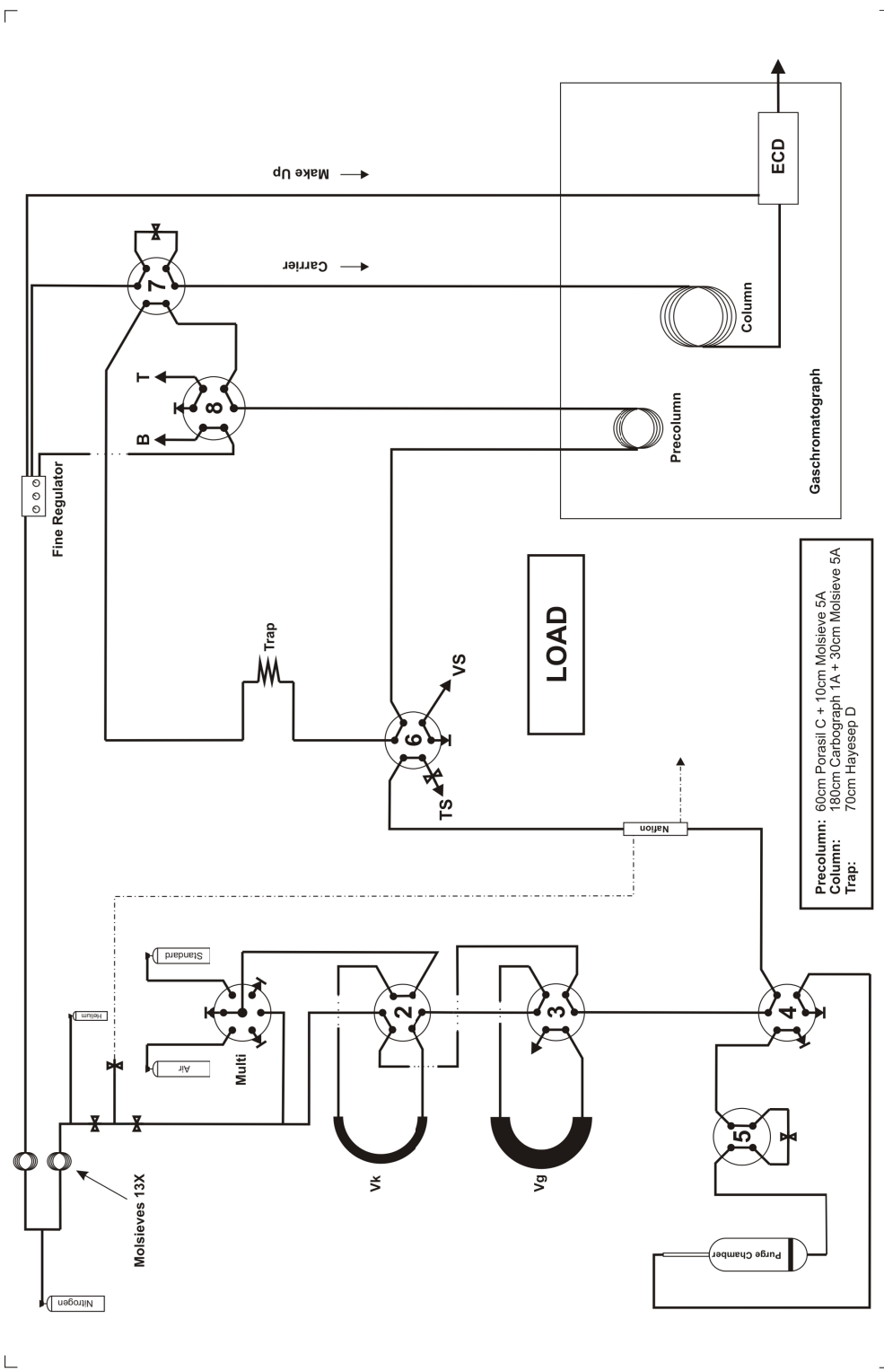
Figure A.2. – VS1-system post cruise.
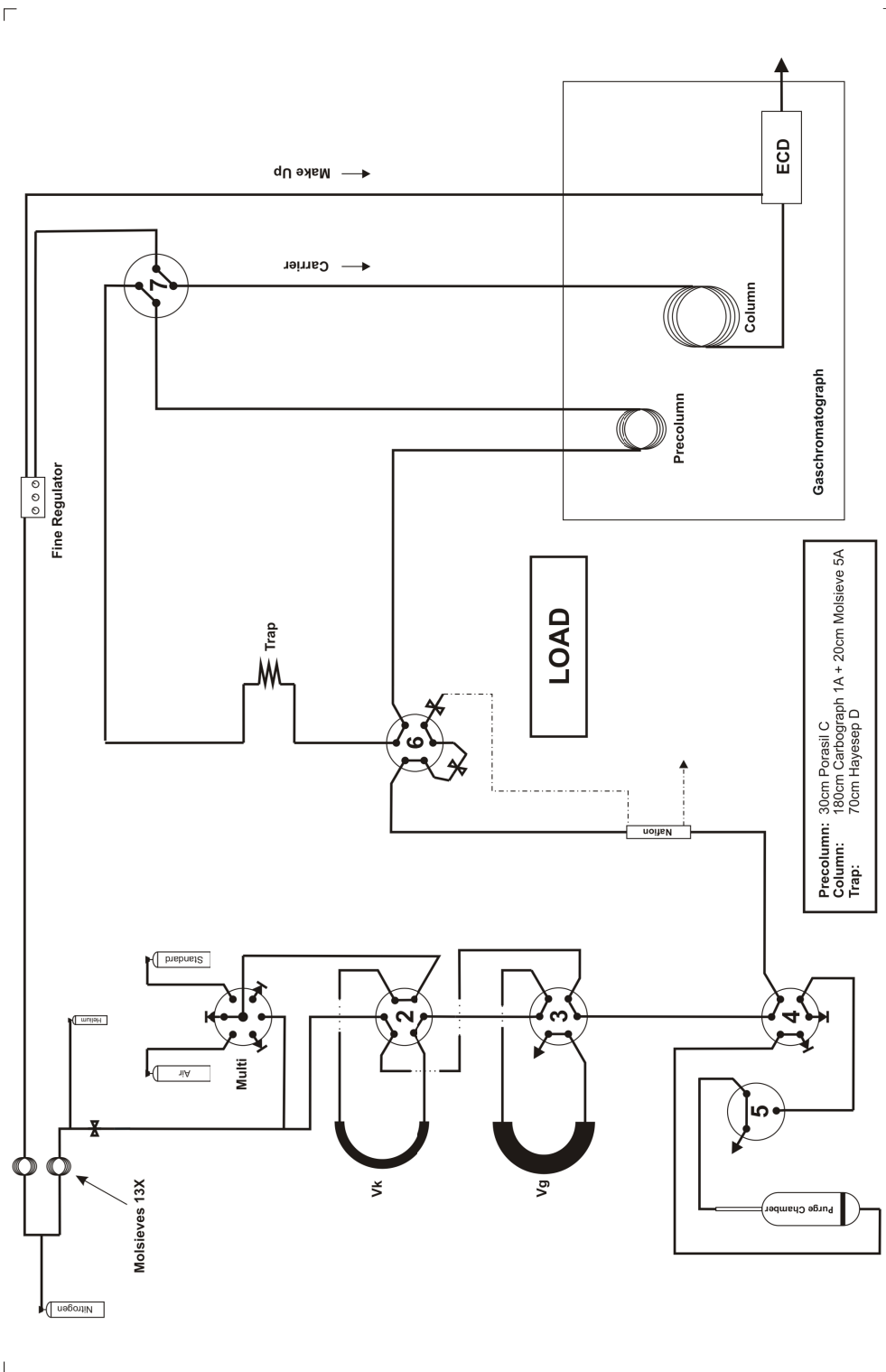
Figure A.3. – PT3-system during M84.
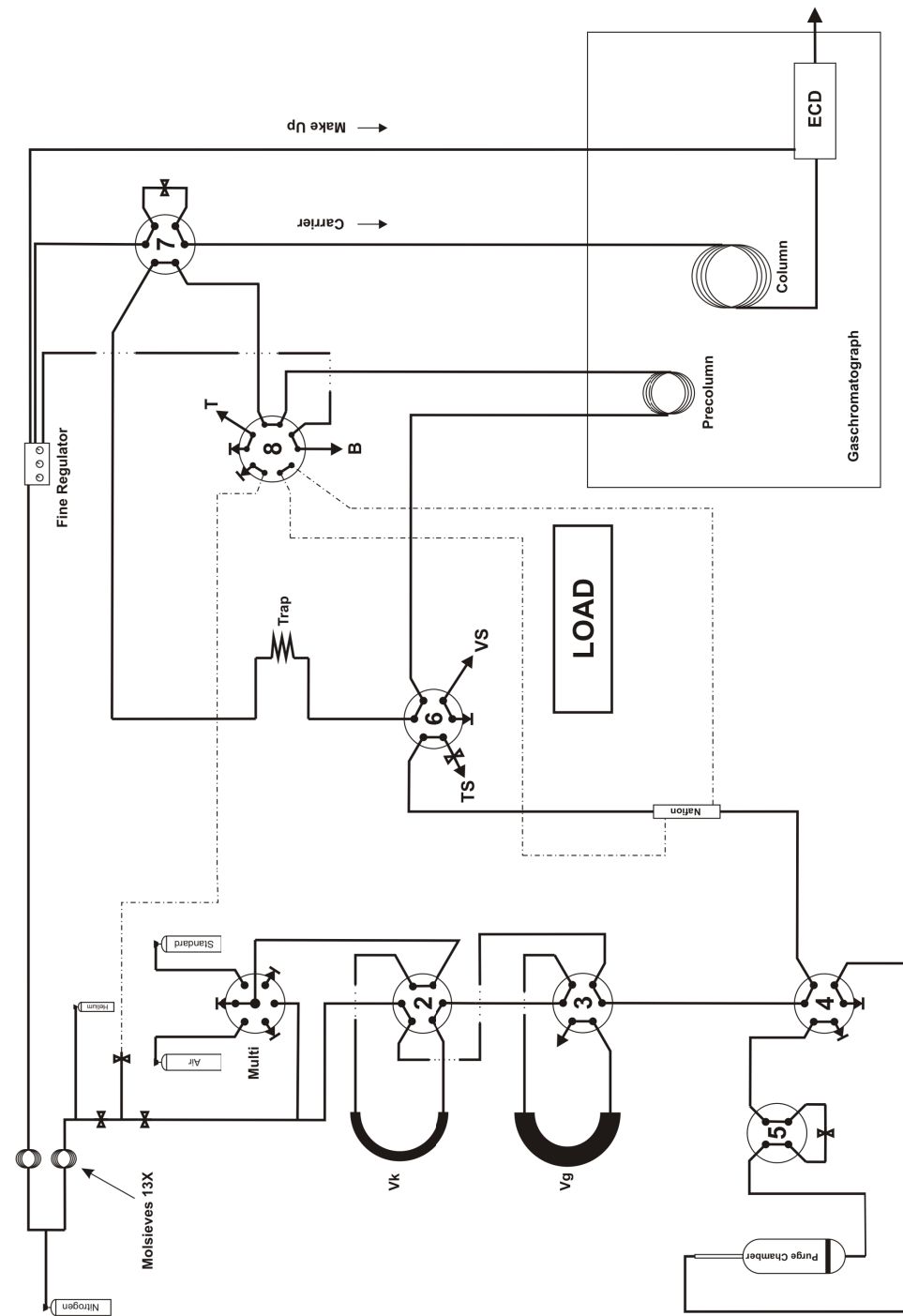
Figure A.4. – PT3-system post cruise.

B. Chromatograms
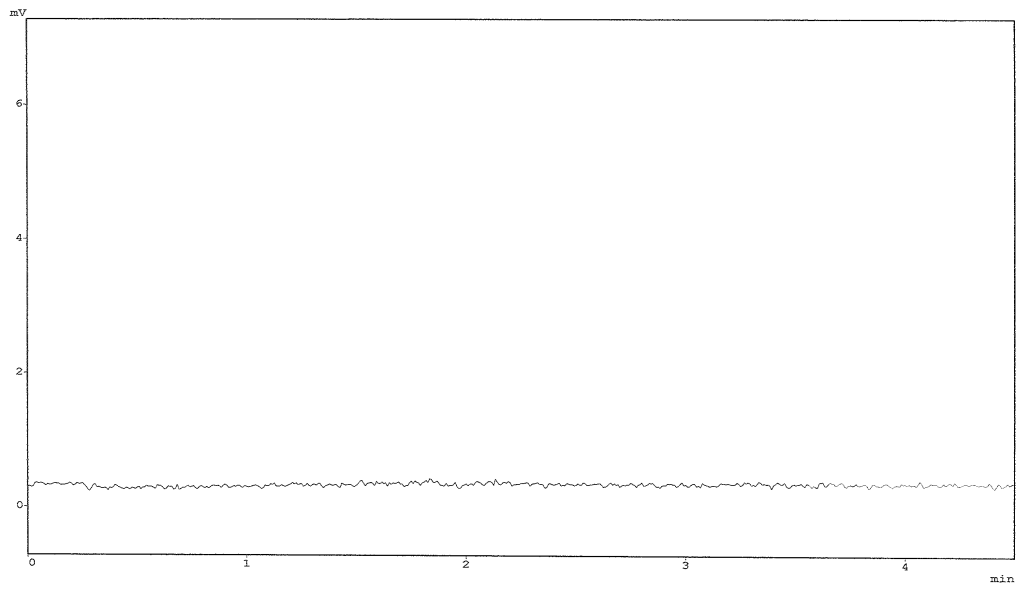
Figure B.1. – VS1 blank (M84).
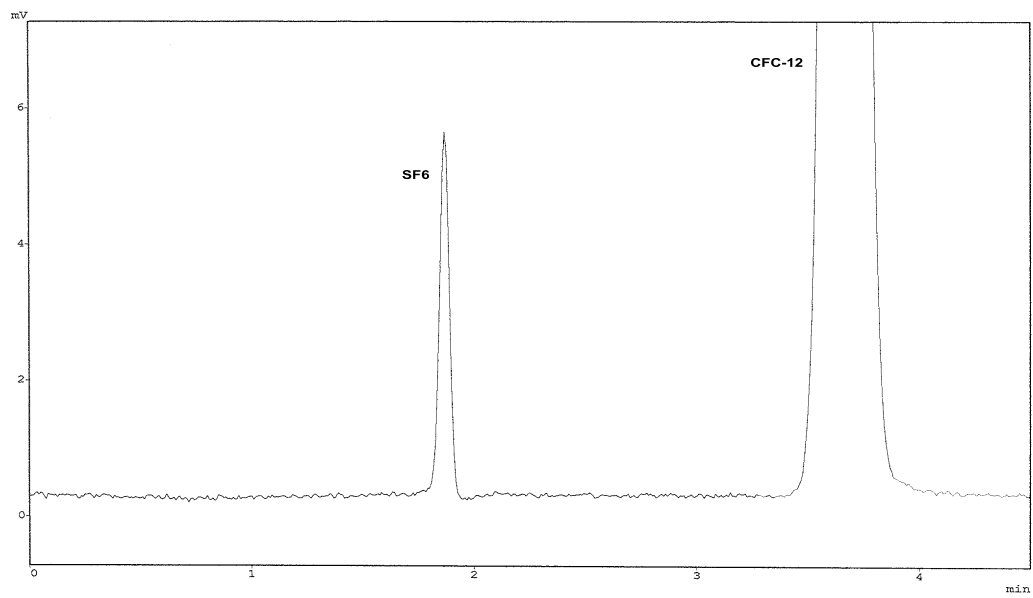
Figure B.2. – VS1 standard (M84).
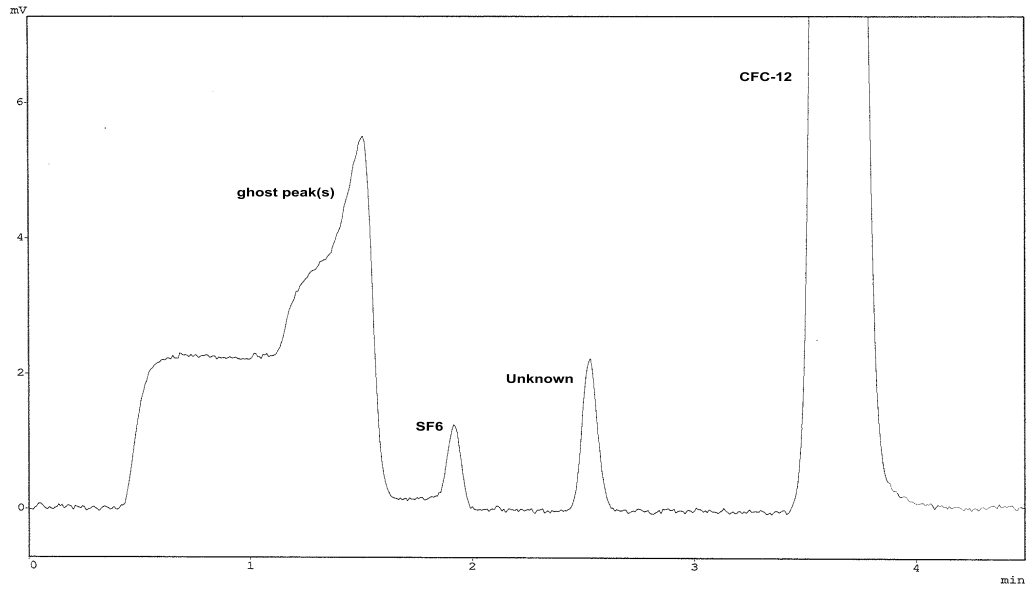
Figure B.3. – VS1 water sample (M84).
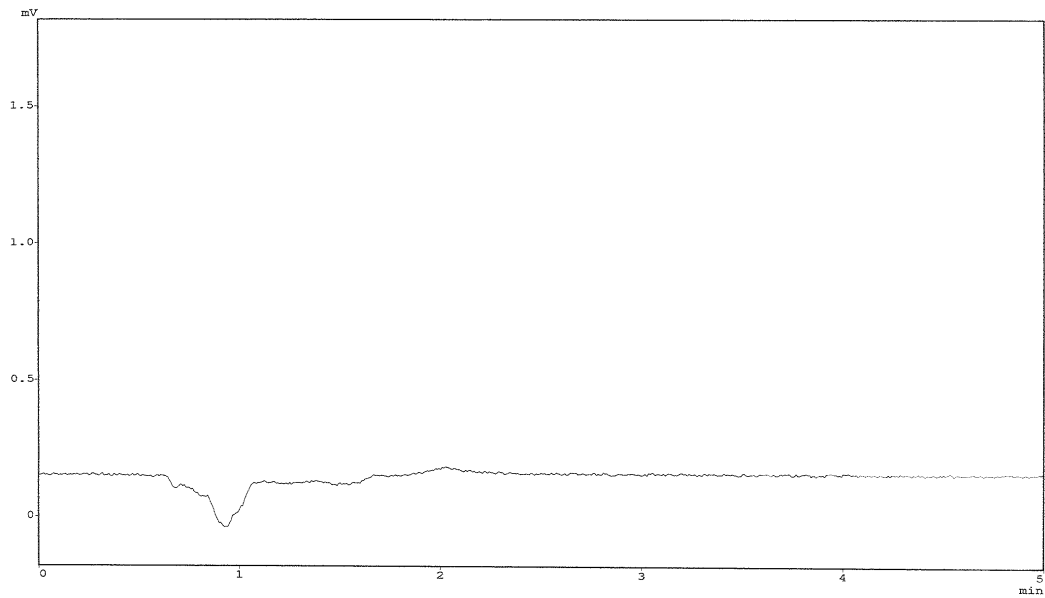
Figure B.4. – VS1 cracker blank.
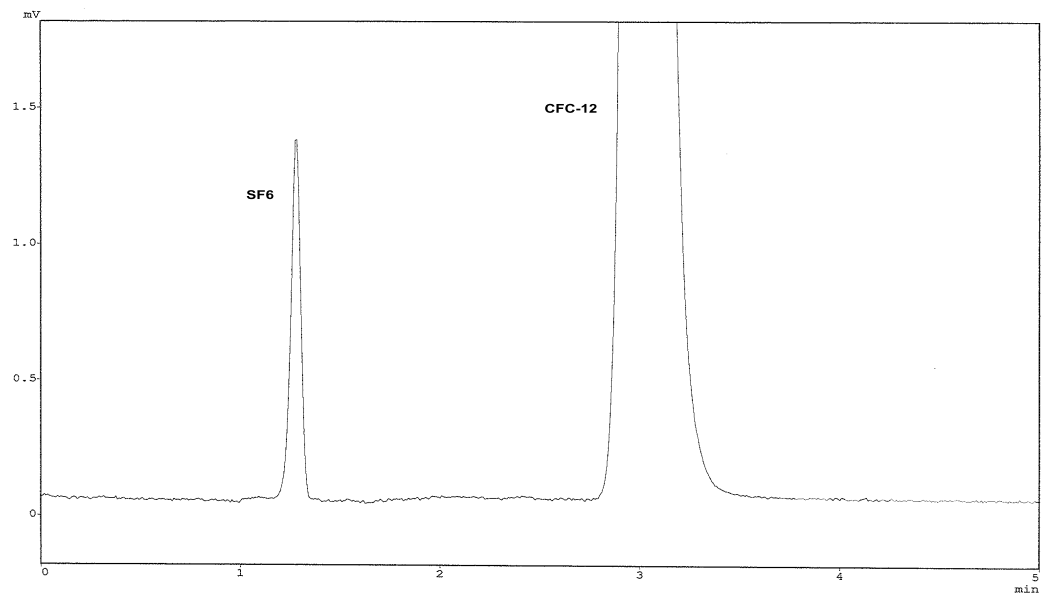
Figure B.5. – VS1 cracker standard.
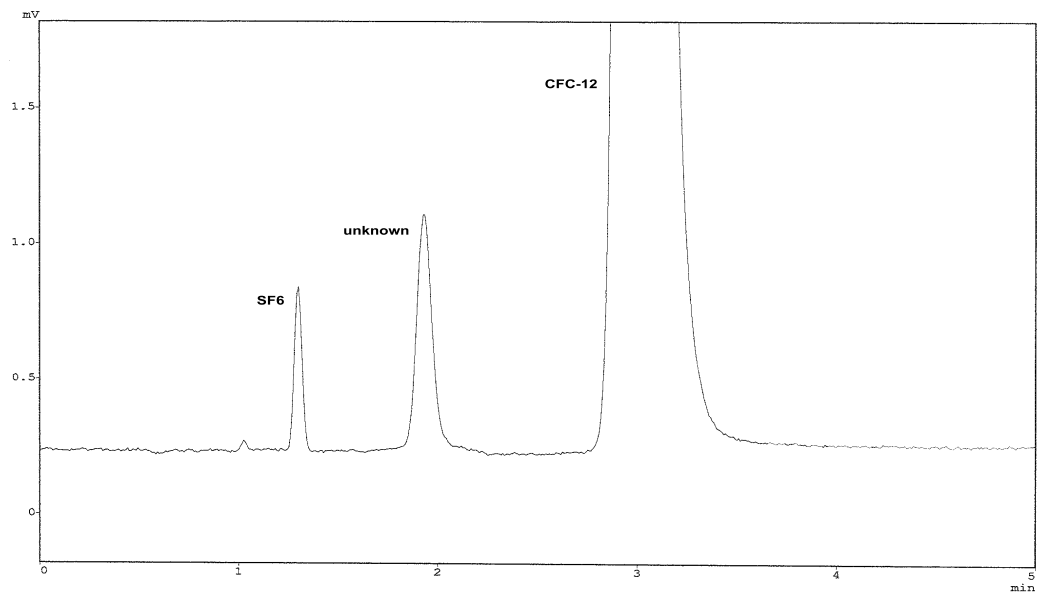
Figure B.6. – VS1 cracker water sample.
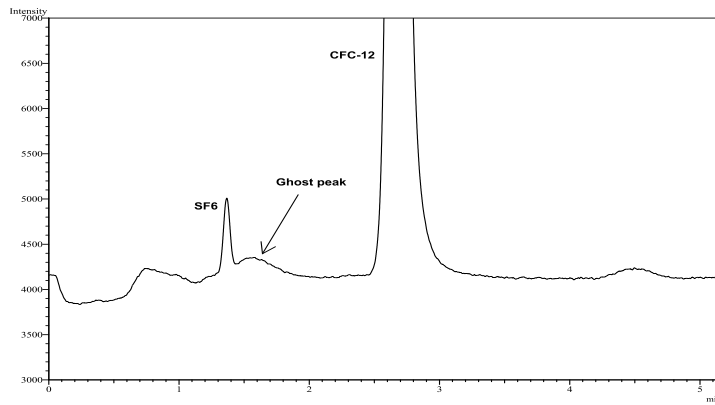
Figure B.7. – PT3 standard (first column setup, M84).
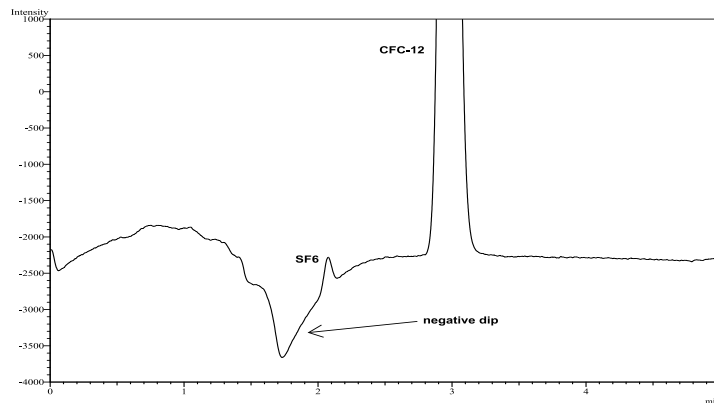
Figure B.8. – PT3 standard (used column setup, M84).
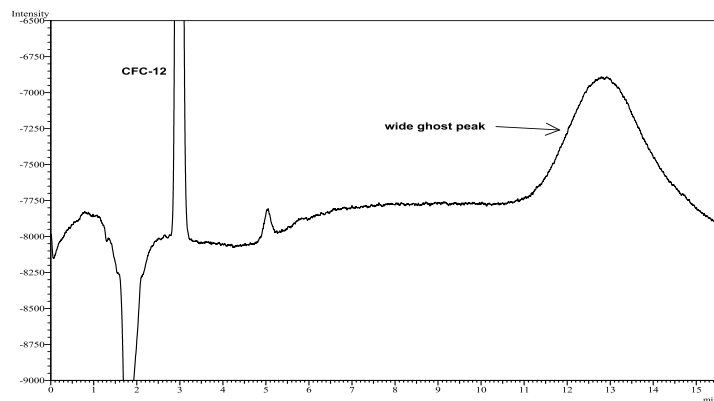
Figure B.9. – PT3 water sample (M84).

C. TTD – Ratio approach
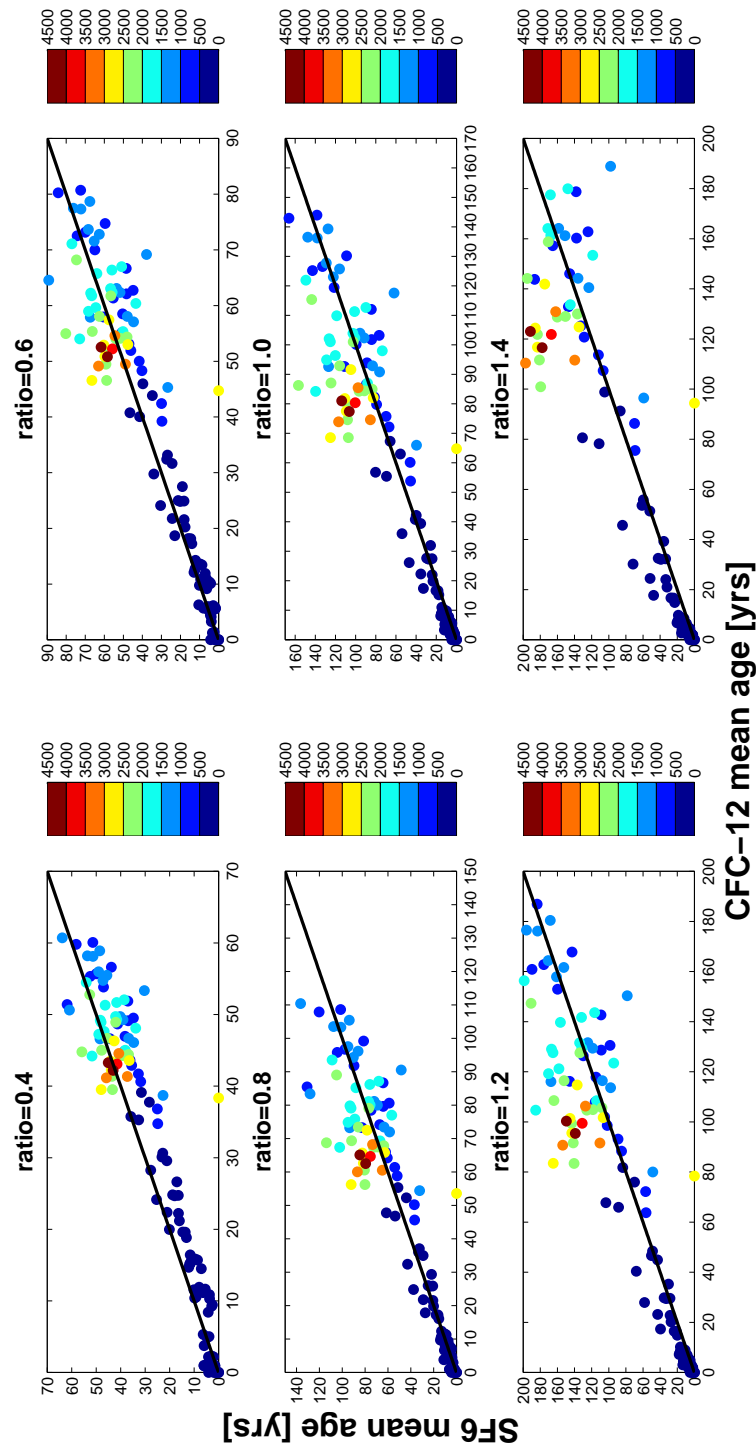
Figure C.1. – Levantine Sea.
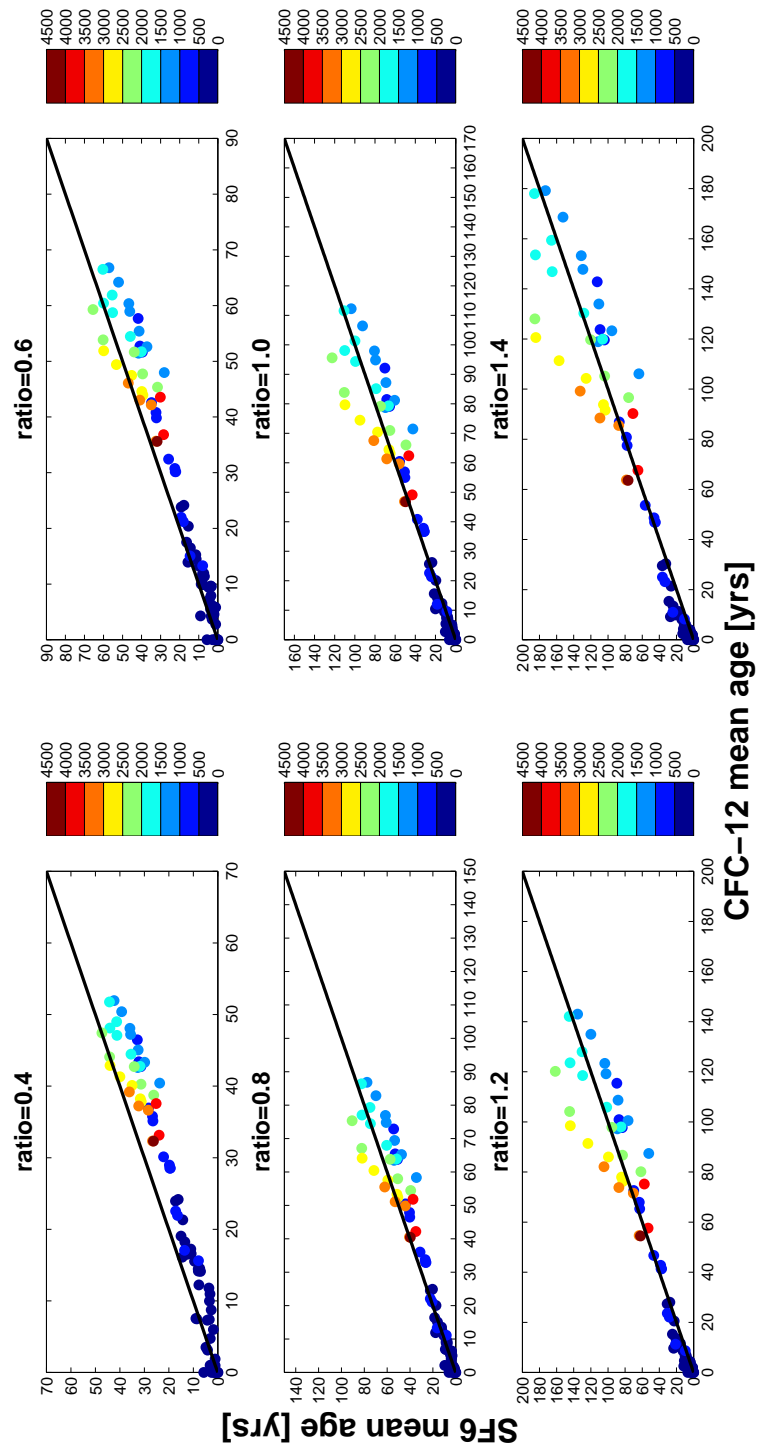
Figure C.2. – Southern Ionian Sea.
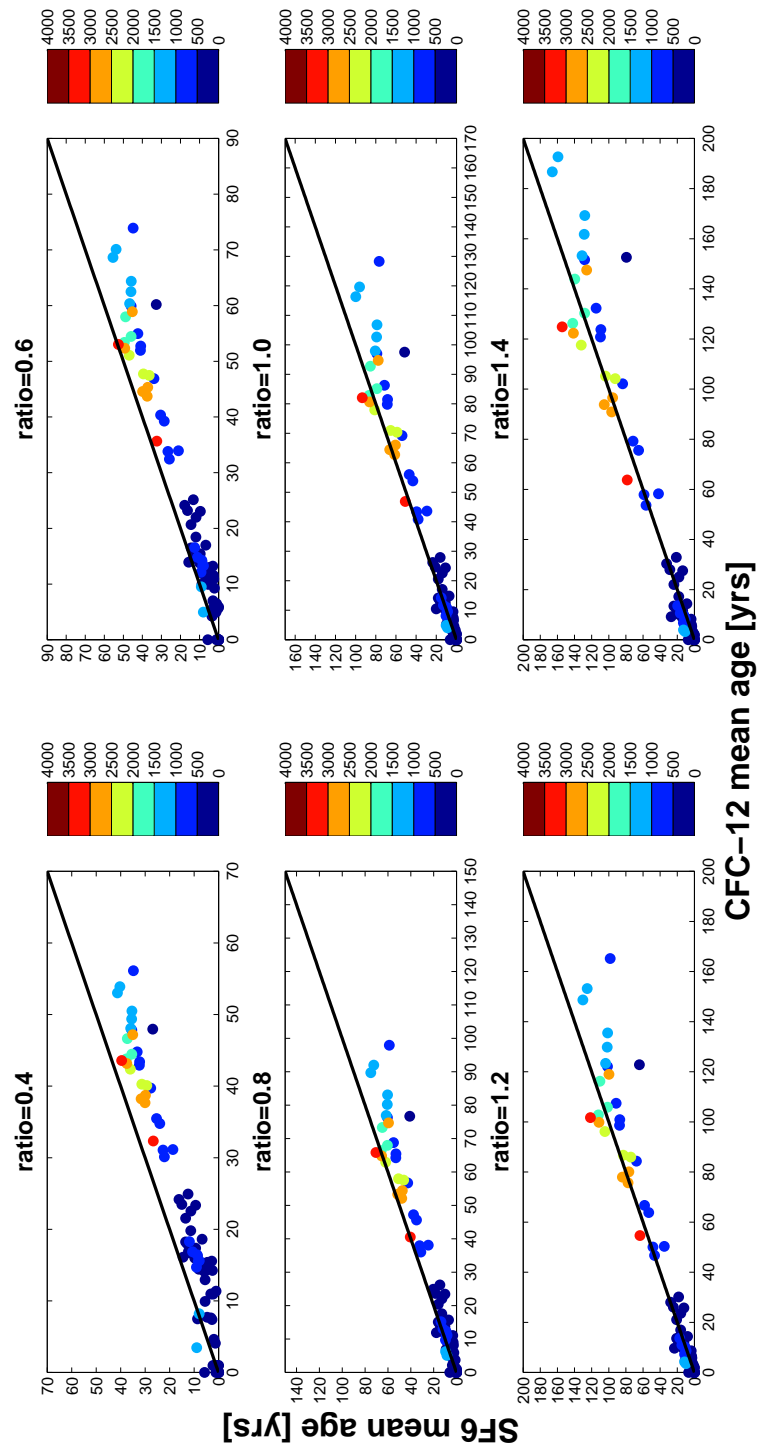
Figure C.3. – Northern Ionian Sea.
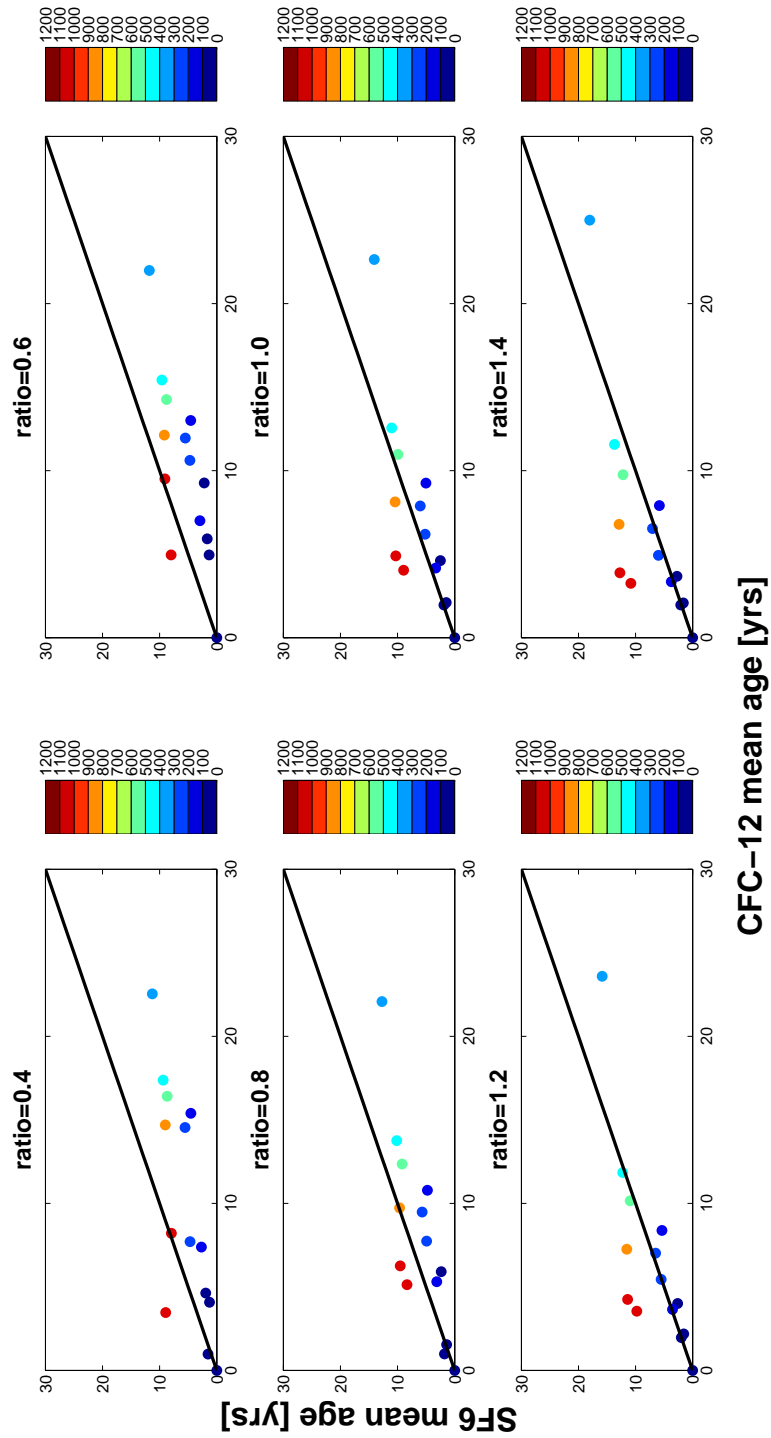
Figure C.4. – Adriatic Sea.
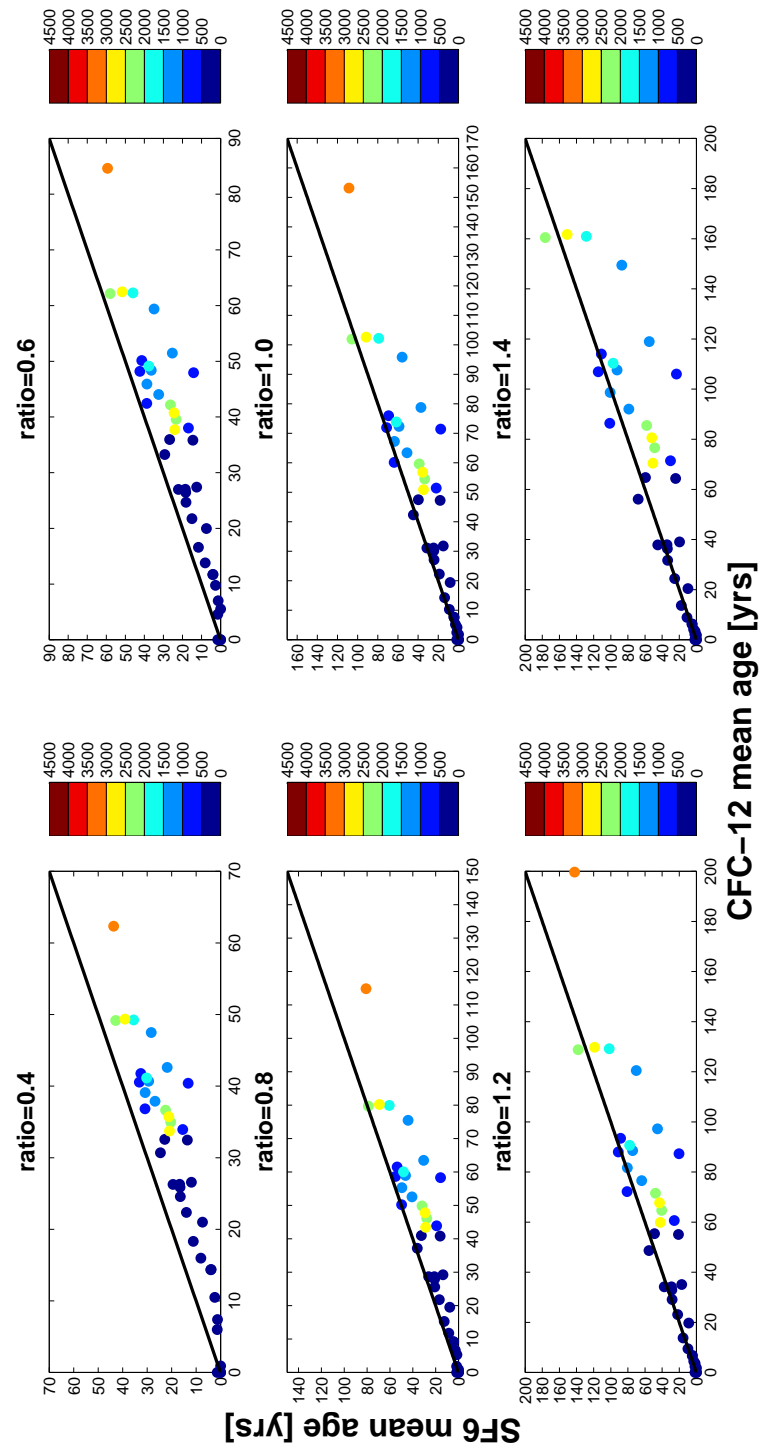
Figure C.5. – Western Mediterranean.

D. M84 and M51 additional data

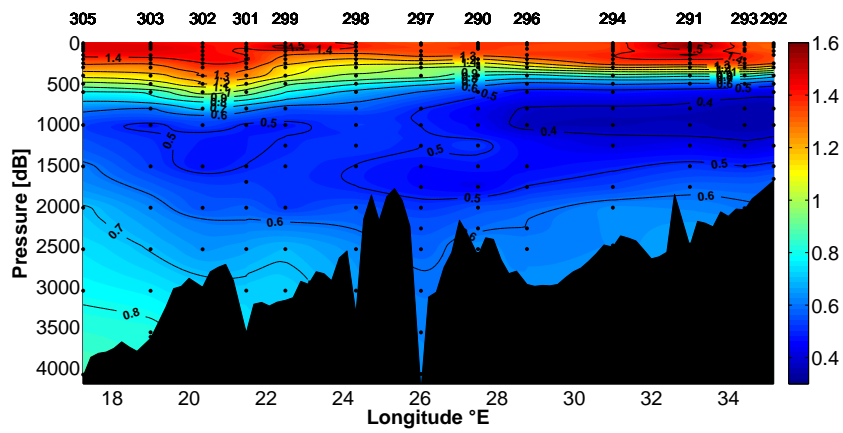## D.1. M84 - Eastern Mediterranean Sea

Figure D.1. – EMed: Concentrations of CFC-12 in $pmol/kg$. Contour line fragmentation of $0.1\,pmol/kg$ and a colour contouring of $0.01\,pmol/kg$.
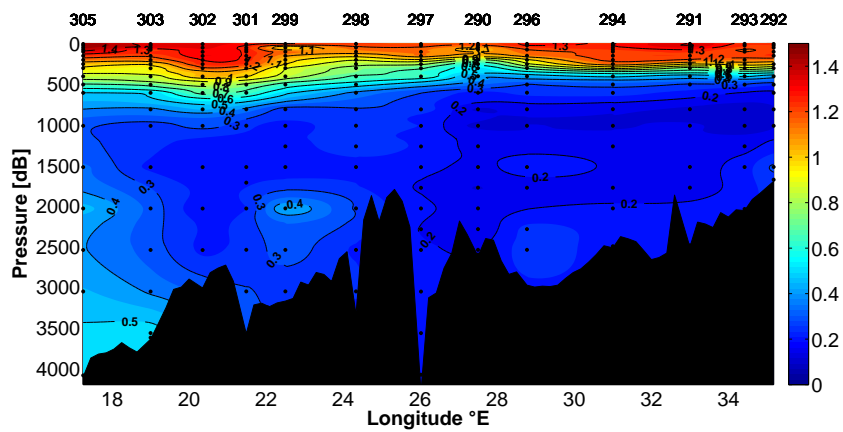

Figure D.2. – EMed: Concentrations of SF$_6$ in $fmol/kg$. Contour line fragmentation of $0.1\,fmol/kg$ and a colour contouring of $0.5\,fmol/kg$

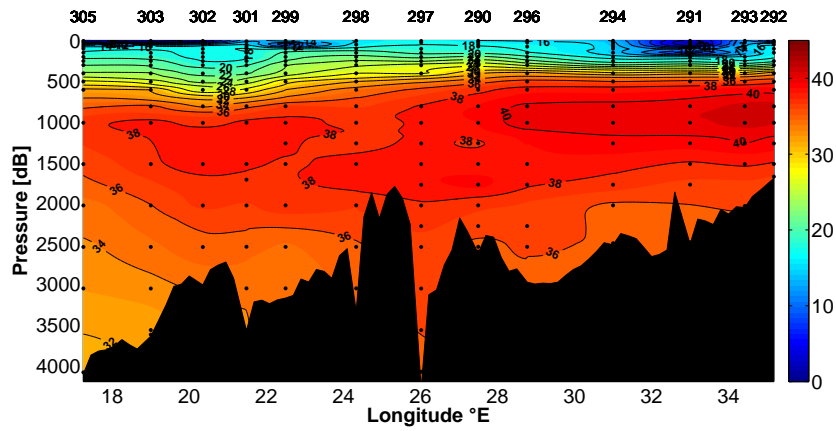**Figure D.3.** – EMed: Tracer age of CFC-12 in yrs. Contour line fragmentation of $2\,yrs$ and a colour contouring of $1\,yr$
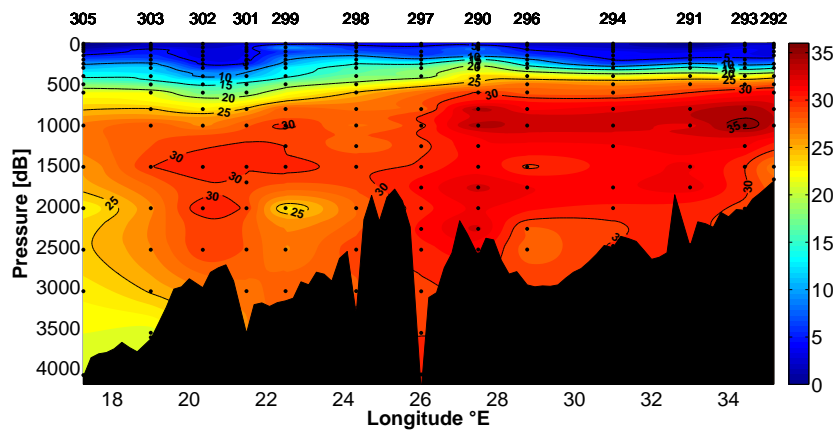

Figure D.4. – EMed: Tracer age of SF_6 in yrs. Contour line fragmentation of $5\,yrs$ and a colour contouring of $1\,yr$
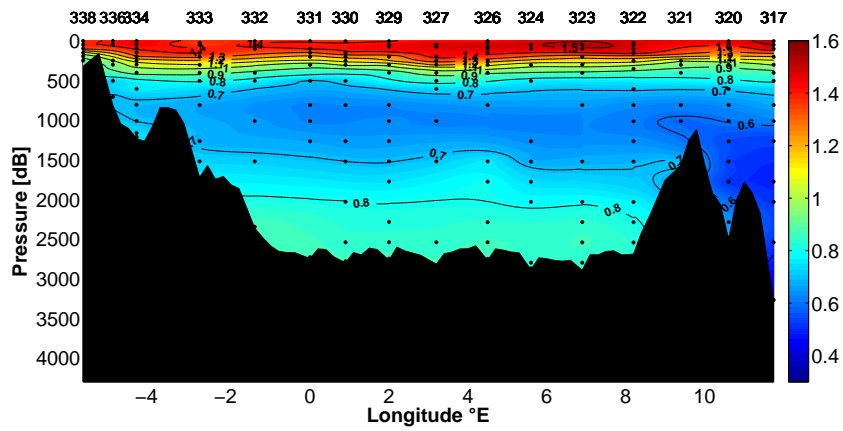
D.2. M84 - Western Mediterranean Sea

Figure D.5. – WMed: Concentrations of CFC-12 in $pmol/kg$. Contour line fragmentation of $0.1\,pmol/kg$ and a colour contouring of $0.01\,pmol/kg$
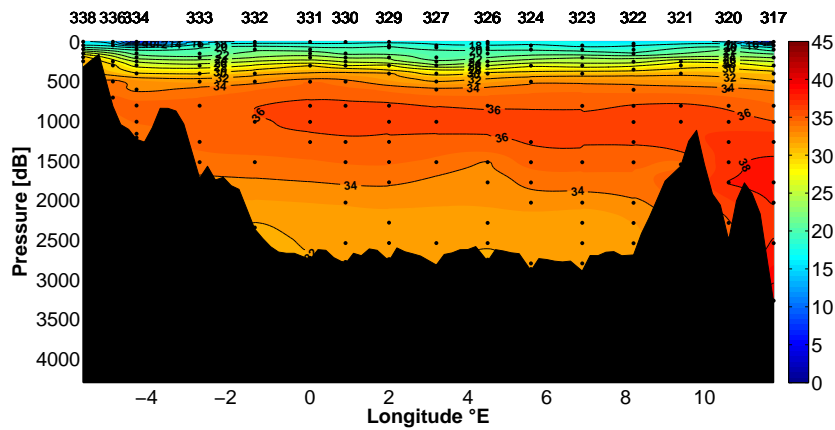

Figure D.6. – WMed: Tracer age of CFC-12 in yrs. Contour line fragmentation of $2\,yrs$ and a colour contouring of $1\,yr$
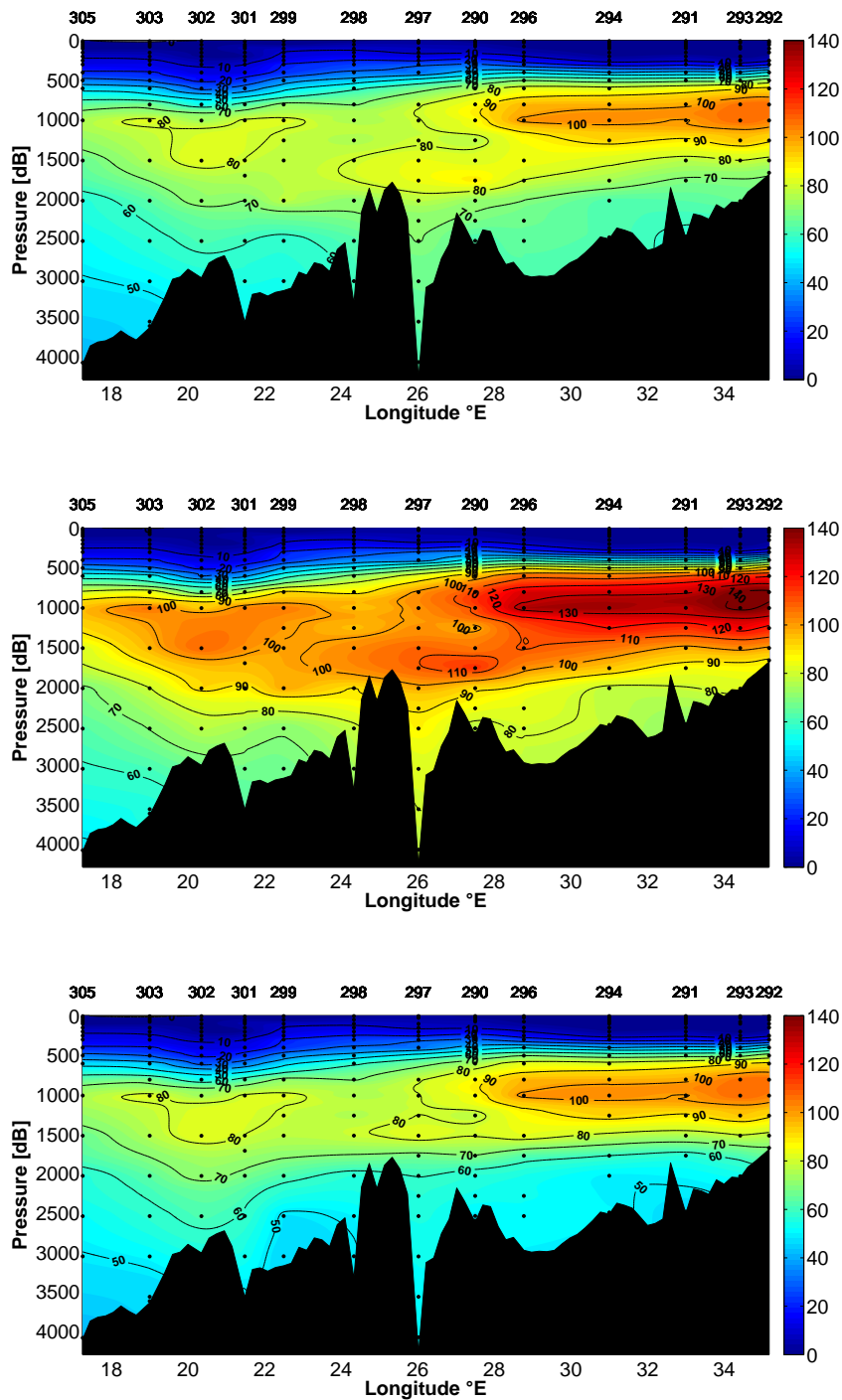
D.3. Mean age of M84 and M51

Figure D.7. – EMed: M84 mean ages of CFC-12 for $^{\Delta}/_{\Gamma} = 0.8$ (top), $^{\Delta}/_{\Gamma} = 1.0$ (center) and best ratio (bottom) in yrs. Contour line fragmentation of $10\,yrs$ and a colour contouring of $1\,yr$

Figure D.8. – EMed: M51 mean ages of CFC-12 for $^{\Delta}/_{\Gamma} = 0.8$ (top), $^{\Delta}/_{\Gamma} = 1.0$ (center) and best ratio (bottom) in yrs. Contour line fragmentation of $10\,yrs$ and a colour contouring of $1\,yr$
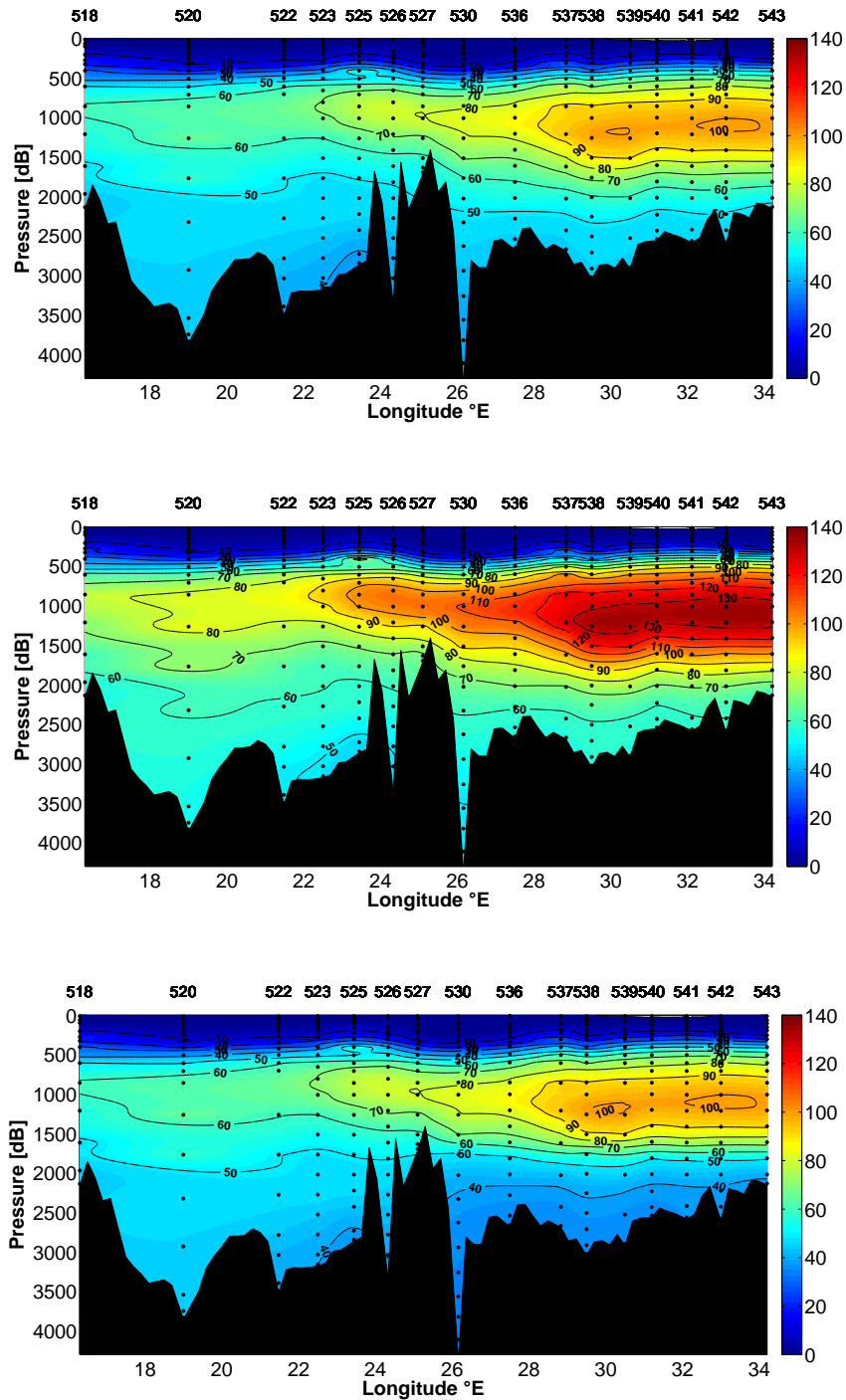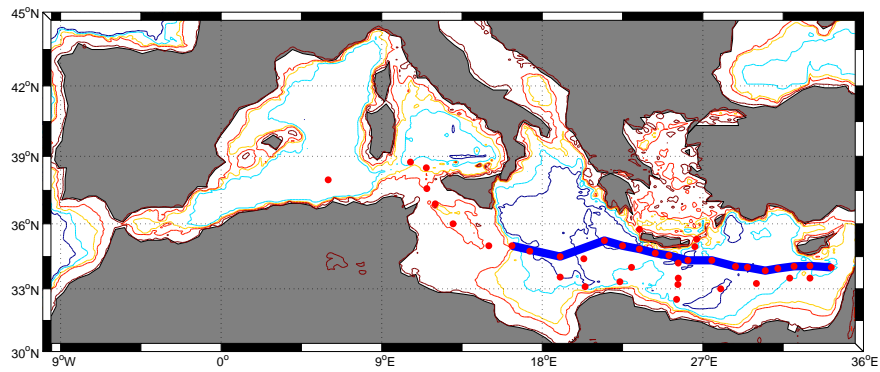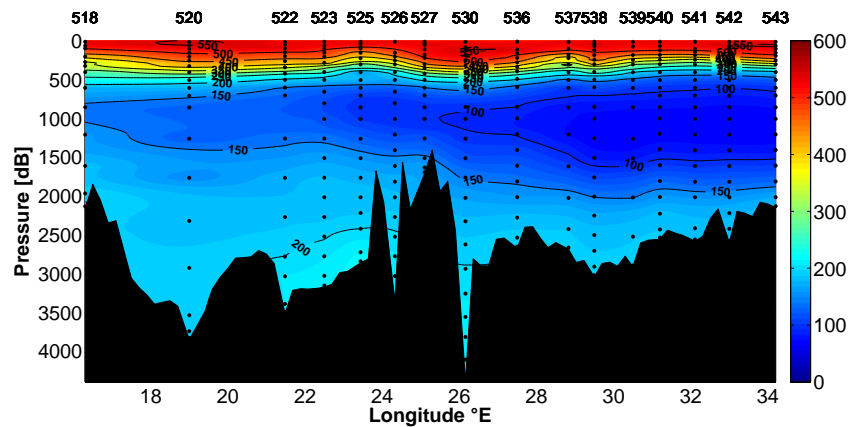
D.4. M51 - Eastern Mediterranean Sea

Figure D.9. – Meteor cruise $M51 - 2$ station map and used section. The depth contours are 500 m, 1000 m, 2000 m and 3000 m.

Figure D.10. – EMed: M51 partial pressure of CFC-12 in *ppt*. Contour line fragmentation of $50\,ppt$ and a colour contouring of $10\,ppt$

D.5. Anthropogenic carbon

Figure D.11. – EMed: M84 anthropogenic carbon in $\mu mol/kg$ for best fitting ratio (top), $^{\Delta}/_{\Gamma} = 0.8$ (center) and $^{\Delta}/_{\Gamma} = 1.0$ (bottom). Contour line fragmentation of $5\,\mu mol/kg$ and a colour contouring of $1\,\mu mol/kg$
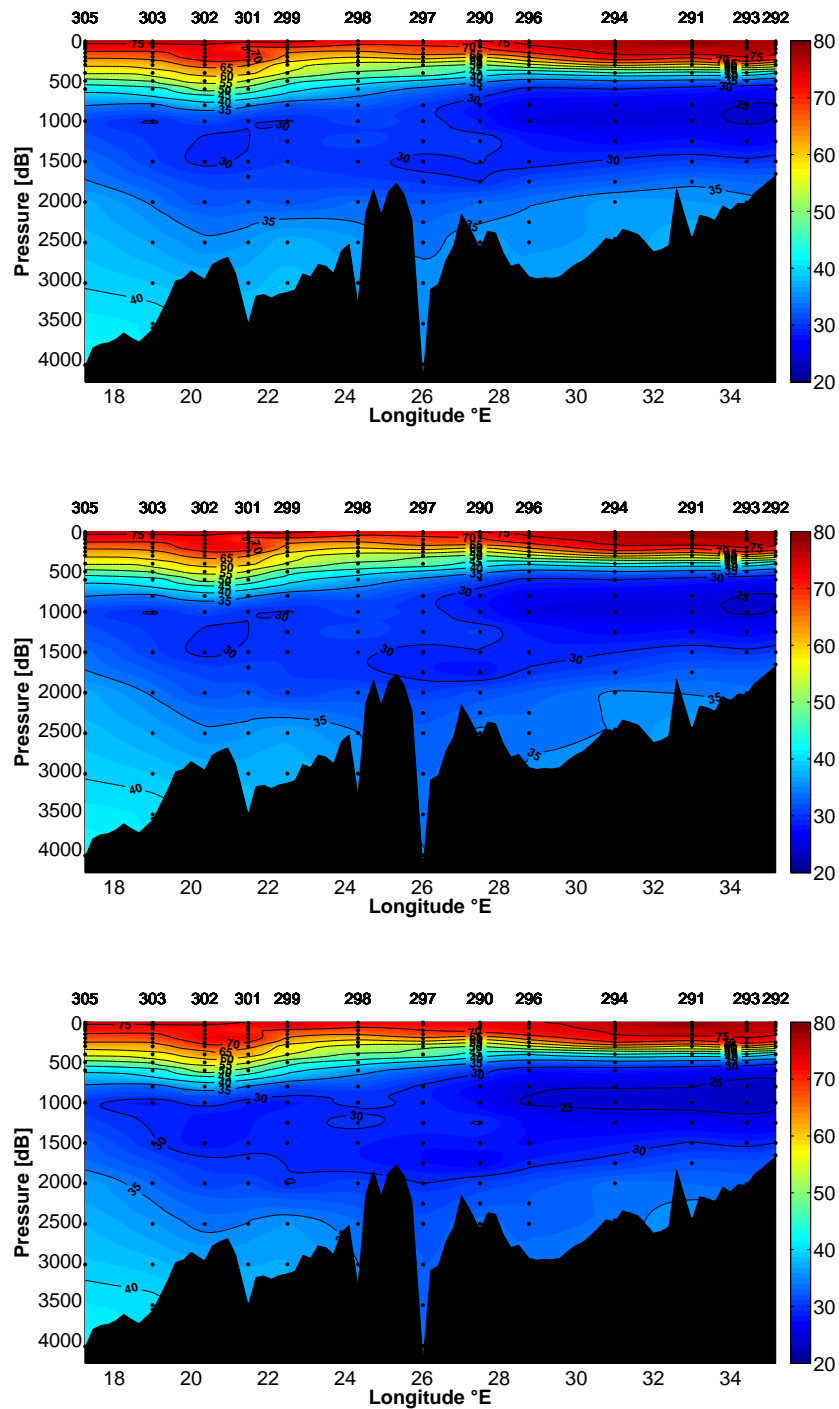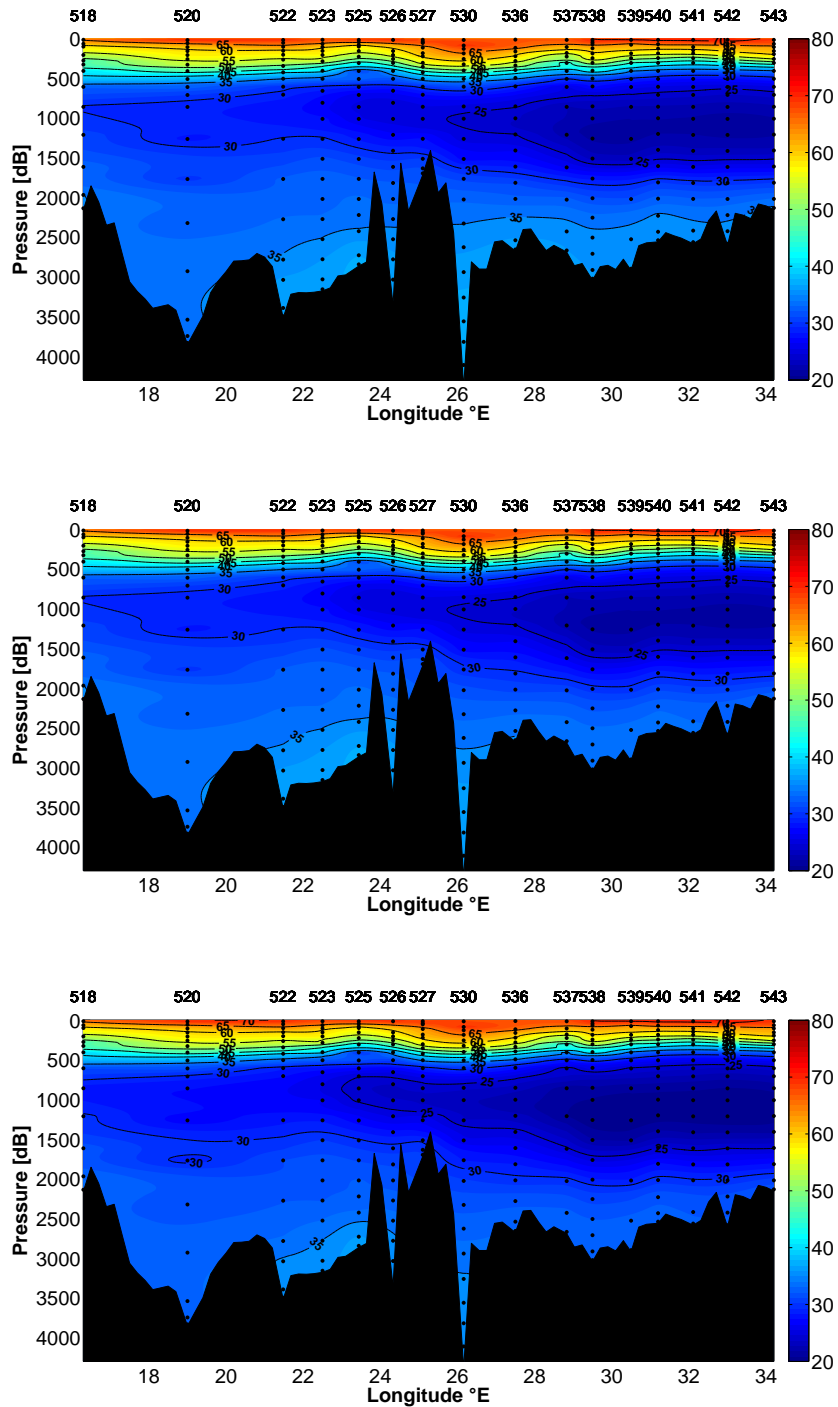
Figure D.12. – EMed: M51 anthropogenic carbon in $\mu mol/kg$ for best fitting ratio (top), $^\Delta/_\Gamma = 0.8$ (center) and $^\Delta/_\Gamma = 1.0$ (bottom). Contour line fragmentation of $5\,\mu mol/kg$ and a colour contouring of $1\,\mu mol/kg$

E. Equipment and Instruments

Table E.1. – Used equipment of *VS1*.

Equipment/Instruments	Producer
300 ml glas ampoules	*Erich Eydam KG*
Computer	*IFM-GEOMAR* cmp
Detector	*Shimadzu* Electron Capture Detector
Fittings	*Valco, Swagelok, Shimadzu*
Flowcontrol	*Shimadzu* 221-32819-91
Flowmeter	*Agilent Technologies* ADM3000
Gas chromatograph	*Shimadzu* GC-14A
Heater	*IFM-GEOMAR* cmp
Laptop	*Toshiba* Satellite 110OCS
Nafion	*PermaPure* MP-050-72S-2
Nitrogen	*Air Liquide* ECD Quality
	Alltech Molsieve 13X (63231-69-6)
Packing material	*Supelco* Molsieve 5Å (69912-79-4)
	Restek Porasil C (57460-15-8)
	GRACE Carbograph 1AC(815581-67-0)
Standard gas	*Deuste Steiniger* cmp
System controller	*Shimadzu* CBM101
Temperature control	*Micromega* PID 77000
Temperature sensor	*Micromega* 5TC-TT
Transformer	*IFM-GEOMAR* cmp
Trap	*GRACE* 70 cm Hayesep D (9003-69-4)
Tubings	*Dockweiler* 1/16, 1/8, 1/4
Vacuum pump	*Vacuubrand* MZ 2C NT
Valve controlbox	*IFM-GEOMAR* cmp
	VICI Valves Valco Instruments Co.Inc.
Valves	E6
	E36
	E60

Table E.2. – Used equipment of *PT3*.

Equipment/Instruments	Producer
250 ml syringes	*TOMOPAL Inc.*
Cooler	*Julabo* FT902
Cooling chamber	*Nalgene* 4150-4000
Detector	*Shimadzu* Electron Capture Detector
Fittings	*Valco*, *Swagelok*, *Shimadzu*
Flowmeter	*Agilent Technologies* ADM3000
Gas chromatograph	*Shimadzu* GC2014
Heater	*IFM-GEOMAR* cmp
Laptop	*IBM* Thinkpad R40
Nafion	*PermaPure* MP-050-72S-2
Nitrogen	*Air Liquide* ECD Quality
Packing material	*Alltech* Molsieve 13X (63231-69-6)
	Supelco Molsieve 5Å (69912-79-4)
	Restek Porasil C (57460-15-8)
	GRACE Carbograph 1AC(815581-67-0)
Standard gas	*Deuste Steiniger* cmp
Temperature control	*Micromega* PID 77000
Temperature sensor	*Micromega* 5TC-TT
Trap	*GRACE* 70 cm Hayesep D (9003-69-4)
Tubings	*Dockweiler* 1/16, 1/8, 1/4
Valve controlbox	*IFM-GEOMAR* cmp
Valves	*VICI Valves Valco Instruments Co.Inc.*
	E6
	E36
	E60

Erklärung

Hiermit versichere ich, dass ich die vorliegende Arbeit selbstständig verfasst und keine anderen als die angegebenen Quellen und Hilfsmittel benutzt habe, dass alle Stellen der Arbeit, die wörtlich oder sinngemäß aus anderen Quellen übernommen wurden, als solche kenntlich gemacht sind und dass die Arbeit in gleicher oder ähnlicher Form noch keiner Prüfungsbehörde vorgelegt wurde.

Kiel, den 30. November 2011